AN INVESTIGATION ON THE EFFECTIVENESS OF NAILED TIMBER WALLS AS RETROFITTING MEASURE FOR SUBSTANDARD CONCRETE STRUCTURES

by
Aslı Keser
B.S., Civil Engineering, Boğaziçi University, 2018

Submitted to the Institute for Graduate Studies in
Science and Engineering in partial fulfillment of
the requirements for the degree of
Master of Science

Graduate Program in Civil Engineering
Boğaziçi University
2022

To my brother

ACKNOWLEDGEMENTS

Before anyone else, I would like to express my infinite gratitude to my thesis advisors Prof. Ario Ceccotti and Prof. Hilmi Luş. I was lucky enough to have them by my side throughout this tough period in my life. Even though there are no words to describe how grateful I am, I wholeheartedly appreciate their kindness, thoughtfulness, and patience. Besides their endless moral support, their immense knowledge and plentiful experience have encouraged me in all the time of my academic research and daily life.

Besides, I would love to express my deepest appreciation to Fatih Bilen for his tremendous support and his persistent guidance. Thanks to his kind heart and willingness to share his knowledge with his peers, I was able to proceed with my master's research.

I would like to express my special thanks to Assoc. Prof. Serdar Selamet and Prof. Alper İlki for providing me with insightful suggestions to further improve my academic research and participating in my thesis jury.

I would also like to thank Ege Çulfaz and Boğaziçi University Structures Laboratory's technicians for their help with the experiments.

I am grateful to my family: my parents Gülsüm and Şenol, my brother Tufan, not only for their tremendous support and encouragement but also for believing in me no matter what I happen to be working on.

Above all, I owe a great depth of gratitude to my soul mate Canberk İnceler for persistently reminding me that there is a light at the end of the tunnel and a bright future waiting for us. Thank you for trying so hard to put a smile on my face even in the darkest of times. Thank you for helping me discover the strength within myself. You are indisputably by far the most important person behind this thesis. None of this would ever have been possible without you. Thank you for being my best friend, rock, muse, editor, and proofreader. Thank you for all the late nights and early mornings, and most importantly for keeping me sane over the last few months. You are everything I could ever ask for. I cannot imagine going through this without you.

ABSTRACT

AN INVESTIGATION ON THE EFFECTIVENESS OF NAILED TIMBER WALLS AS RETROFITTING MEASURE FOR SUBSTANDARD CONCRETE STRUCTURES

Turkey is in a seismically active region and has suffered through extensive losses due to several major earthquakes that struck its various parts. The destructive effects of earthquakes in Turkey are infuriated by the large volume of buildings constructed with low-quality materials and workmanship. Especially a great percentage of residential buildings are constructed by using substandard concrete and reinforcement. Furthermore, research shows a great possibility of a high magnitude earthquake to occur in the near future around the Marmara region, which includes the most populated cities in Turkey. Inevitably, there is a need for an effective and affordable retrofitting method. In this study, a new retrofitting method is introduced and its effect on the seismic performance of two representative case study buildings are investigated. The retrofitting method consists of the implementation of timber walls which are prepared with nails. Initially, cyclic shear tests are performed on two types of nailed timber walls in an effort to obtain stiffness and strength properties. The only difference between the nailed timber walls is the number of nails used. Computational simulations of the experimental tests are generated in CSI Perform3D with buckling restrained brace elements. Two simulations of each case study reinforced concrete buildings retrofitted with the two types of nailed timber walls are conducted along with the original reinforced concrete building. Finally, the seismic performances of structural models are compared with each other. For the first case study building, which is a well-designed building with substandard material quality, it is concluded that even though the seismic performance of the representative building is slightly increased, a comprehensive enhancement in seismic performance is not achieved with the retrofitting method investigated. For the second case study building, which is a poorly designed building with low material quality, seismic performance is significantly improved.

ÖZET

DÜŞÜK BETON DAYANIMLI BİNALARIN ÇİVİLİ AHŞAP DUVARLAR İLE GÜÇLENDİRİLMESİNE İLİŞKİN BİR İNCELEME

Türkiye depremsellik açısından çok aktif bir bölgede yer almaktadır ve çeşitli bölgelerini etkilemiş birçok büyük deprem çok büyük kayıplara yol açmıştır. Düşük malzeme dayanımı ve kalitesiz işçilik ile yapılmış çok sayıda bina, Türkiye'deki depremlerin yıkıcı etkilerini arttırmıştır. Özellikle 2000'lerden önce inşa edilmiş konut binalarının büyük çoğunluğunun standartların altında beton ve donatı kullanılarak yapıldığı düşünülmektedir. Ayrıca araştırmalar, Türkiye'nin en kalabalık şehirlerini içeren Marmara bölgesinde yakın gelecekte büyük bir deprem olma olasılığının yüksek olduğunu göstermektedir. Bu nedenle etkili ve uygun maliyetli bir güçlendirme yöntemine ihtiyaç kaçınılmazdır. Bu çalışmada, ahşaba dayalı bir güçlendirme yöntemi değerlendirilmiş ve bu yöntemin iki binanın sismik performansı üzerindeki etkisi irdelenmiştir. Önerilen güçlendirme yöntemi, çivilerle hazırlanmış ahşap duvarların bina çevresine montajından oluşmaktadır. İlk olarak, rijitlik ve mukavemet özelliklerini elde etmek için iki tip çivili ahşap duvar üzerinde döngüsel yanal yük deneyleri yapılmıştır. Çivilenmiş ahşap duvarlar arasındaki tek fark kullanılan çivi sayısıdır. Daha sonra, CSI Perform3D yazılımı kullanılarak burkulması önlenmiş çelik çaprazlar ile deneysel testlerin bir modeli oluşturulmuştur. Güçlendirilmemiş iki betonarme bina yapısal modelleri ile her binanın iki farklı tip çivilenmiş ahşap duvar ile güçlendirilmiş yapısal modelleri CSI Perform3D yazılımı ile oluşturulmuş ve yapısal modellerin deprem performansları birbirleriyle karşılaştırılmıştır. İrdelenen güçlendirme yöntemi ile, yapısal boyutlandırması son deprem yönetmeliğine uygun olarak yapılmış fakat malzeme dayanımı yetersiz olan ilk vaka çalışması binasının performansı biraz artırılsa da, kapsamlı bir iyileştirme sağlanmadığı sonucuna varılmıştır. İkinci vaka çalışması olarak ise yerleşim ve boyutlandırmada zaafları olduğu gibi aynı zamanda malzeme dayanımı da yetersiz olan binanın önerilen güçlendirme yöntemi ile güçlendirilmesi sonucunda binanın hasar seviyelerinde dikkate değer düşüş sağladığı gözlemlenmiştir.

TABLE OF CONTENTS

ACKNOWLEDGEMENTS iv
ABSTRACT v
ÖZET vi
LIST OF FIGURES ix
LIST OF TABLES xv
LIST OF SYMBOLS xvii
LIST OF ACRONYMS/ABBREVIATIONS xxi
1. INTRODUCTION 1
1.1. General 1
1.2. Research Significance 5
1.3. Objective and Scope of the Study 6
1.4. Thesis Outline 6
2. EXPERIMENT 7
2.1. Experimental Test Setup 7
2.2. Experimental Tests Results 9
2.2.1. NTWs Response 9
2.2.2. Connection Response 10
2.3. Modeling the Experimental Test Setup 10
2.4. Results of CSI Perform3D Models of the Experimental Tests 13
2.5. Parameters for Braces used in CSBs 18
3. NONLINEAR MODELING AND ANALYSIS 22
3.1. CSB Properties 22
3.2. Nonlinear Models 26
3.3. Nonlinear Modeling 29
3.3.1. Material Properties 29
3.3.2. Gravity Loads 33
3.3.3. Seismic Loads 34
3.3.4. Load Combinations 40
3.3.5. Seismic Masses 40
3.3.6. Modeling of Structural Members 41

3.3.7. Damping 44
4. SEISMIC PERFORMANCE OF THE CASE STUDY BUILDING I 45
4.1. General 45
4.2. Interstory Drift Ratios 45
4.3. Column and Beam Plastic Rotations 50
4.4. Structural Wall Shear Force 54
4.5. Strain Values of Structural Walls 58
5. SEISMIC PERFORMANCE OF THE CASE STUDY BUILDING II 64
5.1. General 64
5.2. Interstory Drift Ratios 64
5.3. Column and Beam Plastic Rotations 69
6. CONCLUSIONS AND RECOMMENDATIONS 72
6.1. Summary 72
6.2. Future Recommendations 74
REFERENCES 75

LIST OF FIGURES

Figure 2.1. Framing nailer with nails and the nailing pattern. 7

Figure 2.2. Front and side view of the test setup. 8

Figure 2.3. Hysteresis curve obtained from the experimental test of NTW I. 9

Figure 2.4. Hysteresis curve obtained from the experimental test of NTW II. 9

Figure 2.5. Experimental test model in CSI Perform3D. 10

Figure 2.6. Representative experimental test setup. 11

Figure 2.7. Hysteresis curves obtained from experimental tests and corresponding backbone curves. 12

Figure 2.8. Backbone curve generated based on experiment results of NTW I, and backbone curve of representative brace element used in CSI Perform3D model of the experiment. 12

Figure 2.9. Backbone curve generated based on experiment results of NTW II, and backbone curve of representative brace element used in CSI Perform3D model of the experiment. 13

Figure 2.10. Force record of the experiment of NTW I. 14

Figure 2.11. Displacement results of the experiment (NTW I) and the computational model (BRB I). 14

Figure 2.12. Hysteresis curves of the experiment (NTW I) and the computational model (BRB I). 15

Figure 2.13. Dissipated energies of the experiment (NTW I) and the computational model (BRB I). 15

Figure 2.14. Force record of the experiment of NTW II. 16

Figure 2.15. Displacement results of the experiment (NTW II) and the computational model (BRB II). 16

Figure 2.16. Hysteresis curves of the experiment (NTW II) and the computational model (BRB II). 17

Figure 2.17. Dissipated energies of the experiment (NTW II) and the computational model (BRB II). 17

Figure 2.18. Positions of NTWs in plan view of CSB I. 19

Figure 2.19. Positions of NTWs in plan view of CSB II. 19

Figure 2.20. Backbone curves of NTW I used in CSB I for 3.5 m height and different width values. 20

Figure 2.21. Backbone curves of NTW I used in CSB I for 4.5 m height and different width values. 20

Figure 2.22. Backbone curves of NTW II used in CSB I for 3.5 m height and different width values. 21

Figure 2.23. Backbone curves of NTW II used in CSB I for 4.5 m height and different width values. 21

Figure 3.1. The case study buildings' location and source-to-site distance [20]. 22

Figure 3.2. 3D view of CSB I. 23

Figure 3.3. Elevation view of CSB I. 23

Figure 3.4. Floor plan view of CSB I. 24

Figure 3.5. 3D view of CSB II. 25

Figure 3.6. Elevation view of CSB II. 25

Figure 3.7. Floor plan view of CSB II. 26

Figure 3.8. 3D views of nonlinear models of CSB I. (a)Plain RC, (b) RET I, (c) RET II. 27

Figure 3.9. (a) Plan view of RET I and RET II of CSB I (b) A-A section (c) B-B section. 28

Figure 3.10. 3D views of nonlinear models of CSB II. (a)Plain RC, (b) RET I, (c) RET II. 29

Figure 3.11. Linearized stress-strain relationship of concrete. 32

Figure 3.12. Stress-strain relationship of reinforcement. 33

Figure 3.13. Target spectrum for DD2 ground motion level and increased target spectrum of CSB I. 37

Figure 3.14. Target spectrum for DD2 ground motion level and increased target spectrum of CSB II. 37

Figure 3.15. Mean and target acceleration spectra of CSB I for DD2 ground motion level. 39

Figure 3.16. Mean and target acceleration spectra of CSB II for DD2 ground motion level. 39

Figure 4.1. Control points of interstory drift ratios. 46

Figure 4.2. Mean interstory drift ratios of all models at P1 along x [left] and y [right]. .. 47

Figure 4.3. Mean interstory drift ratios of all models at P2 along x [left] and y [right]. .. 47

Figure 4.4. Mean interstory drift ratios of all models at P3 along x [left] and y [right]. .. 48

Figure 4.5. Maximum interstory drift ratios of all models at P1 along x [left] and y [right]. 48

Figure 4.6. Maximum interstory drift ratios of all models at P2 along x [left] and y [right]. 49

Figure 4.7. Maximum interstory drift ratios of all models at P3 along x [left] and y [right]. 49

Figure 4.8. Damage regions and performance limits. 50

Figure 4.9. Demand - capacity ratios [top] and plastic rotations [bottom] of beams..... 52

Figure 4.10. Demand - capacity ratios [top] and plastic rotations of columns, in the x-direction [middle] and in the y-direction [bottom]. 53

Figure 4.11. Structural wall labels and their locations. 54

Figure 4.12. Structural wall shear forces: SW1 and SW2 [top], SW3 and SW4 [bottom]. 55

Figure 4.13. Structural wall shear forces: SW5a and SW5b [top], SW5c [bottom]. 56

Figure 4.14. Structural wall shear forces: SW6a and SW6b [top], SW6c [bottom]. 57

Figure 4.15. Story shear forces in x and y directions. 58

Figure 4.16. Strain measurement locations on floor plan. 59

Figure 4.17. Structural wall strains: SG1 and SG2 [top], SG3 and SG4 [bottom]. 60

Figure 4.18. Structural wall strains: SG5 and SG6 [top], SG7 and SG8 [bottom]. 61

Figure 4.19. Structural wall strains: SG9 and SG10 [top], SG11 and SG12 [bottom]. 62

Figure 4.20. Structural wall strains: SG13 and SG14 [top], SG15 and SG16 [bottom]. 63

Figure 5.1. Control points of interstory drift ratios. 65

Figure 5.2. Mean interstory drift ratios of all models at P1 along x [left] and y [right]. .. 66

Figure 5.3. Mean interstory drift ratios of all models at P2 along x [left] and y [right]. .. 66

Figure 5.4. Mean interstory drift ratios of all models at P3 along x [left] and y [right]. .. 67

Figure 5.5. Maximum interstory drift ratios of all models at P1 along x [left] and y [right]. 67

Figure 5.6. Maximum interstory drift ratios of all models at P2 along x [left] and y [right]. 68

Figure 5.7. Maximum interstory drift ratios of all models at P3 along x [left] and y [right]. 68

Figure 5.8. Demand - capacity ratios [top] and plastic rotations [bottom] of beams..... 70

Figure 5.9. Demand - capacity ratios [top] and plastic rotations of columns in x [middle] and y [bottom] directions..... 71

LIST OF TABLES

Table 3.1. Stiffness modifiers of reinforced concrete elements. 30

Table 3.2. Mechanical properties of steel. 33

Table 3.3. Magnitude of uniform loads. 34

Table 3.4. Spectral acceleration coefficients for the prototype building under DD2 level earthquake. 34

Table 3.5. Local soil effect coefficient for short period. 35

Table 3.6. Local soil effect coefficient for one second period. 35

Table 3.7. Design spectral acceleration coefficients. 36

Table 3.8. Input parameters of Ground Motion Database. 38

Table 3.9. Ground motion properties for DD2 earthquake level. 40

Table 3.10. Live load participation factor. 41

Table 4.1. Seismic performance assessment metrics and corresponding limits. 45

Table 4.2. Number of beam elements in different damage regions for positive bending. 50

Table 4.3. Number of beam elements in different damage regions for negative bending. 51

Table 4.4. Number of column elements in different damage regions. 51

Table 4.5. Performance limits for tension and compression strains on walls. 59

Table 5.1. Seismic performance assessment metrics and corresponding limits. 64

Table 5.2. Number of beam elements in different damage regions for positive bending. 69

Table 5.3. Number of beam elements in different damage regions for negative bending. 69

Table 5.4. Number of column elements in different damage regions. 70

LIST OF SYMBOLS

A_s	Cross-sectional area of reinforcements
a_i	Spacing of two longitudinal bars for i^{th} pair
b_o	Width of confined concrete core
d_b	Average longitudinal reinforcement diameter in tension
E_c	Concrete tangent modulus of elasticity
$E_d^{(Z)}$	Vertical earthquake load
$(EI)_e$	Effective flexural rigidity of section
E_s	Modulus of elasticity of reinforcement
E_{sec}	Secant modulus of elasticity of reinforcement
F_1	Local soil effect coefficient for one second period
f_c	Compressive stress of confined concrete
f_{cc}	Compressive strength (peak stress) of confined concrete
f_{ce}	Expected compressive strength of concrete
f_{ck}	Characteristic compressive strength of concrete
f_{co}	Compressive strength of unconfined concrete
f_e	Effective confining pressure
f_{ex}	Effective confining pressure on X direction
f_{ey}	Effective confining pressure on Y direction
f_s	Stress of reinforcement
F_S	Local soil effect coefficient for short period
f_{su}	Ultimate strength of reinforcement
f_{sy}	Yield strength of reinforcement
f_{ye}	Expected yield strength of reinforcement
f_{yw}	Yield strength of transverse reinforcement

g	Gravitational constant
G	Dead loads
G_c	Shear modulus of concrete
G_{ce}	Effective shear modulus of concrete
h	Slab thickness
h_i	Height of ith story
h_o	Height of confined concrete core
k_e	Confinement effectiveness coefficient
k_{ex}	Confinement effectiveness coefficient on X direction
k_{ey}	Confinement effectiveness coefficient on Y direction
L_p	Plastic hinge length
L_s	Shear span
M_y	Yield Moment
n	Live load contribution factor
N	Number of ground motion pairs
Q	Live loads
Q_e	Efficient live loads
r	Ratio of tangent modulus to difference of tangent and secant modulus
R_{JB}	Closest distance from project location to projection of rupture surface
s	Spacing of transverse reinforcement
S_1	Spectral acceleration coefficient for one second period
$S_{ae}(T)$	Elastic design spectral acceleration at period T
S_{aeR}	Spectral acceleration value of ground motion record
S_{aeT}	Spectral acceleration value of target spectrum
S_{D1}	Design spectral acceleration coefficient for one second period
S_{DS}	Design spectral acceleration coefficient for short period

S_S	Spectral acceleration coefficient for short period
T	Natural vibration period
T_A	Left corner spectrum period
T_B	Right corner spectrum period
T_L	Limit period for constant displacement range
T_p	Fundamental natural vibration period
V	Shear force demand
$V_{s,30}$	Shear wave velocity at first 30 m depth of soil
w_i	Weight of natural period
$w_j^{(S)}$	Concentrated seismic weight at node j
$w_{G,j}^{(S)}$	Concentrated seismic weight at node j from dead loads
$w_{Q,j}^{(S)}$	Concentrated seismic weight at node j from live loads
x	Ratio of any strain to strain at ultimate compressive strength of confined concrete
$\delta_{i,\max}$	The maximum value of interstory drift at i^{th} story
ε_c	Confined concrete strain
ε_{cc}	Strain at ultimate strength of confined concrete
ε_{co}	Strain at ultimate strength of unconfined concrete
ε_s	Strain at reinforcement
ε_{sh}	Strain hardening initiation strain of reinforcement
ε_{su}	Ultimate strain of reinforcing steel
ε_{sy}	Yielding strain of reinforcement
$\theta_p^{(CP)}$	Plastic rotation for collapse prevention limit
$\theta_p^{(IO)}$	Plastic rotation for immediate occupancy limit
$\theta_p^{(LS)}$	Plastic rotation for life safety limit
θ_y	Yield rotation

κ	A coefficient used to set the limit interstory drift ratio
λ	Empirical coefficient used to limit the story drift
λ_c	Confined concrete strength modifier
ν_c	Poisson ratio of concrete
ρ_x	Ratio of transverse confining steel volume to volume of confined concrete core on X direction
ρ_y	Ratio of transverse confining steel volume to volume of confined concrete core on Y direction
ϕ_u	Ultimate curvature
ϕ_y	Yield curvature

LIST OF ACRONYMS/ABBREVIATIONS

3D	Three Dimensional
AFAD	Disaster and Emergency Management Presidency
BRB	Buckling Restrained Brace
CP	Collapse Prevention
CSB	Case Study Building
CSI	Computers and Structures, Inc
IO	Immediate Occupancy
LS	Life Safety
MSE	Mean Squared Error
NLTHA	Nonlinear Time History Analysis
NTW	Nailed Timber Wall
PEER	Pacific Earthquake Engineering Research Center
RC	Reinforced Concrete
RET	Retrofitted Version
SRSS	Square Root of Sum of the Squares
SS	Strike-Slip
TBSC	Turkish Building Seismic Code
TS	Turkish Standards

1. INTRODUCTION

1.1. General

A widely accepted definition of natural hazards is “those elements of the physical environment, harmful to man and caused by forces extraneous to him” [1]. Natural hazards refer to atmospheric, hydrologic, geologic, and wildfire phenomena that due to their location, severity, and frequency, have the potential to affect humans adversely [2]. Disasters are serious disruptions to the functioning of a community causing extensive damage to society that exceed its capability to cope using its resources. A logical inference from these two definitions is that while natural hazards may be inevitable, disasters are not. Therefore, communities can and should mitigate disasters by being prepared, reducing risks, and becoming more resilient.

Disaster risk is a function of the severity and frequency of the hazard, of the numbers of people and assets exposed to the hazard, and of their vulnerability or susceptibility to damage. According to the layers of risk, disaster risk can be divided into two types. The more intensive risk layers, which are characterized by exceptionally low frequency but high severity losses, are normally associated with extreme hazard events. The more extensive risk layers, which are characterized by high frequency but low severity losses, are associated with localized and recurrent hazard events [3].

Earthquakes often are among the most devastating natural hazards. According to United Nations Office for Disaster Risk Reduction (UNDRR), in the first decade of the 21st century alone, earthquake-induced disasters accounted for 60 percent of deaths from natural disasters all around the world [4]. Striking without warning, an earthquake in a populated area may result in numerous casualties and injuries along with considerable property damage.

Turkey is one of the most seismically active regions in the world since it is located at the intersection of Eurasian, African, and Arabian plates through the Anatolian plate [5].

Interactions between all surrounding plates and the Anatolian plate produce an active seismic region that encompasses most of Turkey [6]. Inescapably, earthquakes have been by far the most substantial natural hazard in the region. Since the beginning of the 20th century, all natural disasters in Turkey resulted in 97,000 casualties and almost 9.8 million people were affected. Earthquakes were responsible for 96.8% of the casualties and 73.3% of the affected population [7].

While it is not possible to predict the exact time and location of an earthquake, scientists are able to estimate whether there will be an earthquake sometime in the future on a particular fault or not [8]. The westward progression of seven large earthquakes along the North Anatolian fault since 1939 poses a significant risk of a strong earthquake near Istanbul, a rapidly growing city with a population of 15.5 million. In 2000, the probability of occurrence of a magnitude 7 or higher earthquake within 30 years was calculated as 62 ± 15% (one standard deviation) [9]. Although the probability of occurrence of a strong earthquake near Istanbul has possibly increased with the passing years, the progress made towards preparing for the next earthquake has not gone much beyond pilot studies of regional risk assessment and seismic retrofitting of a limited number of essential buildings [6]. A worst-case scenario earthquake with a magnitude of 7.5 near Istanbul is estimated to result in 35,000 to 40,000 heavily damaged (damaged beyond repair) buildings with 5,000 to 6,000 of them reaching collapse and an estimated number of 30,000 to 50,000 casualties [10].

Although the degree of hazard due to earthquakes primarily depend on depth, distance, duration, peak ground velocity and spectral intensities of the resulting ground motion, and soil properties of the affected region, the main reason for this natural hazard to become a disaster with a large number of casualties and physical losses are primarily the result of building and infrastructure failure induced by earthquake effects [11].

Since 1940, due to fast industrialization action, migration from rural to urban areas and high population growth rate resulted in the construction of a considerable number of multistory residential buildings in the cities. In Turkey, the most frequent form of construction for multistory residential buildings has been reinforced concrete structural frames. This type of building has experienced the greatest portion of damages and casualties during earthquakes [12]. There have been many studies worldwide to determine the main

reasons behind extensive damage observed in multistory reinforced concrete buildings due to earthquakes and the following issues have been reported as the major reasons: non-ductile detailing, strong-beam weak-column condition, short-column effect, soft and weak floor mechanisms, irregularity in plan and elevation, unconfined gable/infill walls, bad workmanship, and low material strength. When the scope of the research is limited to Turkey, researchers remarked that most of the collapses and damages that occur in multistory reinforced concrete buildings due to earthquakes mainly result from insufficient material and construction quality, and poor design practice [11]. Moreover, inadequate lateral stiffness of the building structural systems is also one of the most important inferences made from the post-earthquake investigations in Turkey [13, 14].

Based on what has been discussed so far, it should be clear that a significant portion of building stock in Turkey is vulnerable to earthquakes. Unfortunately, a substantial number of those vulnerable buildings are located in the Marmara region where a strong earthquake with a magnitude of greater than seven is expected in near future. For these buildings to withstand the effects of the expected earthquake, immediate actions should be taken. Replacement and retrofitting are the two options that the building owners have. Although replacement of a building should result in a seismically safe building that is designed and constructed in compliance with the latest seismic code provisions, it is an expensive and time-consuming option that should only be considered when seismic retrofitting is deemed ineffective.

While many conventional and innovative solutions have been developed for seismic retrofitting of existing reinforced concrete frame buildings, the commonly utilized retrofitting technique is the addition of reinforced concrete infill shear walls [12, 15]. The retrofitting process includes demolishing of brick walls, embedment of anchorage rebars within columns and beams, placement of reinforcing steel and building formwork, drilling of slabs, and casting of concrete. It is usually effective in terms of improving the seismic performance of existing buildings, but it requires a long-lasting construction work. Considering the current situation of building stock in Turkey, a fast, affordable, and effective retrofitting technique is undoubtedly necessary in order to prevent a possible disaster.

Cross laminated timber (CLT) panels have been attracting increasing interest in construction sector due to their seismic performances, low environmental impact, ease of construction, etc. Furthermore, in recent years, CLT panels are getting more recognized as a structural solution for seismic retrofitting of existing structures such as reinforced concrete frame buildings. [16]

In this study, the use of cross laminated nailed timber walls (NTW) as a fast, affordable, and effective seismic retrofitting alternative is investigated. Such walls may be produced with relative ease using local materials so that their material and workmanship cost could be expected to be significantly less than concrete walls. The stiffness and strength values for such walls may be expected to be affected by the number of nails and the type of wood species used, with a glued cross-laminated timber wall representing the upper bound that could be attained by increasing the number of nails.

The objective of the effectiveness in terms of improving the seismic performance is investigated throughout this study. In order to assess the improvements on seismic performance that is gained via installation of NTWs, two case study buildings are investigated. A typical 5-story substandard reinforced concrete building is selected as the first case study. The first case study building is a RC frame building with structural walls which is initially designed in compliance with the latest seismic code provisions ; to introduce shortcomings due to material quality, material properties are assumed to be worse than the initial design assumptions, so that the characteristic compressive strength of concrete is assumed to be 10 MPa and the steel class is assumed to be S220, to imitate pre-2000 building stock. The seismic performance of the first case study building is compared with two retrofitting scenarios. The first scenario includes retrofitting with a wall that has relatively low stiffness and strength values and the second scenario with relatively high stiffness and strength values due to the number of nails per meter square. The first timber wall contains half of the number of nails that the second wall has. The load-deformation characteristics of the NTWs under cyclic shear loading are obtained from the experiments conducted at Boğaziçi University's Structural Lab. CSI Perform3D software is used to construct nonlinear models and to perform nonlinear response history analyses of the three building scenarios, namely: plain RC, retrofitted with Wall I (RET I), and retrofitted with

Wall II (RET II). Comparative evaluation of nonlinear analysis results for the three computational models of the first case study building is interpreted.

As a second case study building, a RC frame building that represents a typical existing building in Turkey which suffers from most of the typical construction deficiencies that are common for the buildings constructed before recent earthquake design codes such as poor material quality, inadequate transverse reinforcement, inadequate column dimensions and poor placement choices. Additionally, analysis results of the building shows that it also suffers from strong beam weak column problem. Similar to the first case study building, characteristic compressive strength of concrete is assumed to be 10 MPa and steel class is assumed to be S220. The procedure followed to investigate the effect of retrofitting with NTWs on seismic performance of the first case study building is repeated for the second case study building.

1.2. Research Significance

Immediate action should be taken in order to prevent a major disaster due to a high magnitude earthquake that is expected to hit Marmara Region in near future. Therefore, existing buildings in this region should be seismically rehabilitated to limit the number of injuries and casualties. Two options are available for seismic rehabilitation: retrofitting and replacement. Retrofitting is usually a much more convenient option in the case of existing buildings since replacement is unnecessary and expensive in most cases. In this study, a new retrofitting method is introduced and investigated in terms of its effect on the seismic performance of two substandard reinforced concrete buildings. The retrofitting method consists of the installation of NTWs. The introduced retrofitting method uses locally produced timber and nails so that it is a relatively more affordable retrofitting alternative. Additionally, since timber has adequate stiffness and strength properties, it provides high seismic capacity and, due to its exceptionally low self-weight, it generates low seismic demand. Therefore, the investigated retrofitting method is expected to improve the seismic performances of the two case study buildings. In this study it is aimed to thoroughly discuss the effectiveness of the introduced retrofitting method.

1.3. Objective and Scope of the Study

Two different retrofitting scenarios are implemented to two substandard RC buildings and their seismic performances are compared to investigate the effectiveness of retrofitting with NTWs. A 5-story RC frame building with structural walls assumed to be constructed with substandard structural materials is investigated as the first case study building and a 6-story RC frame building is investigated as the second case study building. Afterward, computational simulations of implementation of two different types of NTWs are generated in two separate nonlinear models for each CSB. The three structural models for each CSB are analyzed with Nonlinear Time History Analysis (NLTHA) method and based on analysis results seismic performances of the nonlinear models are compared. Observations and recommendations on the effectiveness of retrofitting with NTWs are presented.

1.4. Thesis Outline

The outline of this thesis is divided into six chapters. In Chapter 1, general information about the subject and primary objectives of the study are presented. This study is based on the experimental tests conducted on NTWs and in Chapter 2, the experimental test setup and modeling of the experimental test setup in CSI Perform3D are explained in detail. Additionally, backbone curves for NTWs that are assumed to be installed in the case study buildings are provided in this chapter. Chapter 3 addresses the procedure followed for nonlinear structural modeling of the case study buildings. Seismic performance analysis of the three structural models of the first case study building and their comparison in terms of interstory drift ratio, beam and column plastic rotation, shear force in structural walls, concrete compressive strain, and reinforcing steel tensile strain values are provided in Chapter 4. Similarly in Chapter 5, seismic performance analysis and comparison of the three structural models of the second case study building in terms of interstory drift ratio, and beam and column plastic rotations are presented. Finally, in Chapter 6, an overview with closing comments as well as recommendations for future studies are presented.

2. EXPERIMENT

2.1. Experimental Test Setup

The experimental tests are conducted in the structural laboratory of Boğaziçi University to investigate the response of NTWs under cyclic shear loading. The timber used in the specimens is black pine (Pinus Nigra) growing on the Anatolian peninsula of Turkey. 12 cm locally produced nails are used to reinforce the timber panels. Nails are driven into the wood by a framing nailer as shown in Figure 2.1 along with the nailing pattern. The two test specimens of the full-scale NTWs are five-layered 120 mm thick panels without openings. The width and height of the test specimens are 1500 mm and 2810 mm, respectively. The only difference between the two test specimens is the number of nails. The first specimen has been prepared with 1200 nails, and the second specimen has been prepared with 2400 nails. From now on, the first and second NTW specimens will be labeled as NTW I and NTW II, respectively.



Figure 2.1. Framing nailer with nails and the nailing pattern.

At the bottom of the wall, at concrete-to-timber joints, angle brackets are used to transfer tensile and shear forces. Rothoblaas© WHT620 is used for tensile forces and Rothoblaas© TCF200 is used for shear forces. At the top of the wall, in order to transfer shear forces, Rothoblaas© TTF200 is used.

The lateral load was applied to the specimens using a hydraulic jack at a height of 2860 mm from the bottom of the specimens. The lateral load was measured by the load cell inside the hydraulic jack. Two displacement transducers were placed at the bottom and the top of the wall. The top displacement transducer measured the lateral displacement of the entire wall whereas the bottom displacement transducer aimed to measure the sliding displacement of the wall relative to the concrete foundation. Lateral displacement values presented in Figure 2.3 and Figure 2.4 are the difference of the values measured by the top and the bottom displacement transducers. Two additional displacement transducers that are positioned vertically were also placed to measure the uplifting of the walls. However, the uplifting effect is assumed not to be a primary concern while evaluating lateral displacement of the specimens. In addition, lateral guides with rollers were used to ensure a steady and consistent unidirectional movement of the walls.



Figure 2.2. Front and side view of the test setup.

2.2. Experimental Tests Results

2.2.1. NTWs Response

Two retrofitting scenarios are investigated throughout this thesis. The first retrofitting scenario consists of the addition of BRB elements into the CSI Perform3D model that are the representation of NTWs prepared with 1200 nails (NTW I). The second retrofitting scenario consists of the addition of BRB elements into the CSI Perform3D model that are the representation of NTWs prepared with 2400 nails (NTW II). The properties of the models are derived from the cyclic shear tests results for nailed timber panels presented in Figure 2.3 and Figure 2.4.

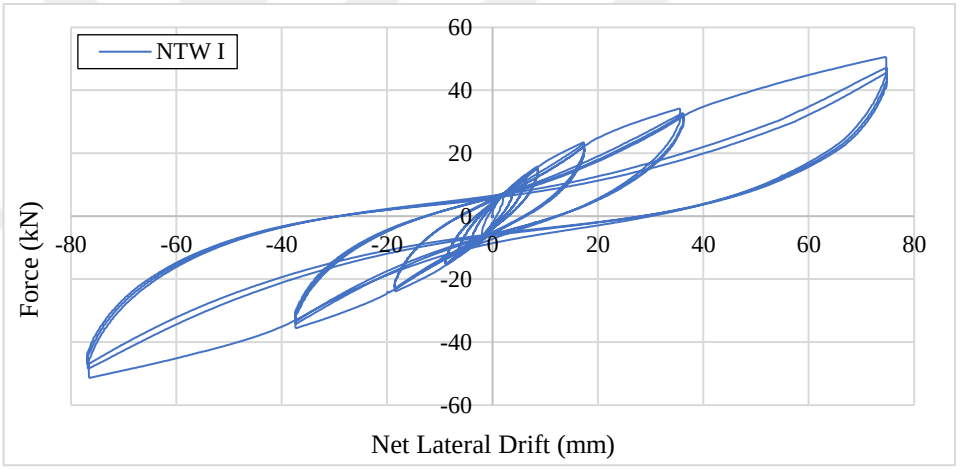

Figure 2.3. Hysteresis curve obtained from the experimental test of NTW I.

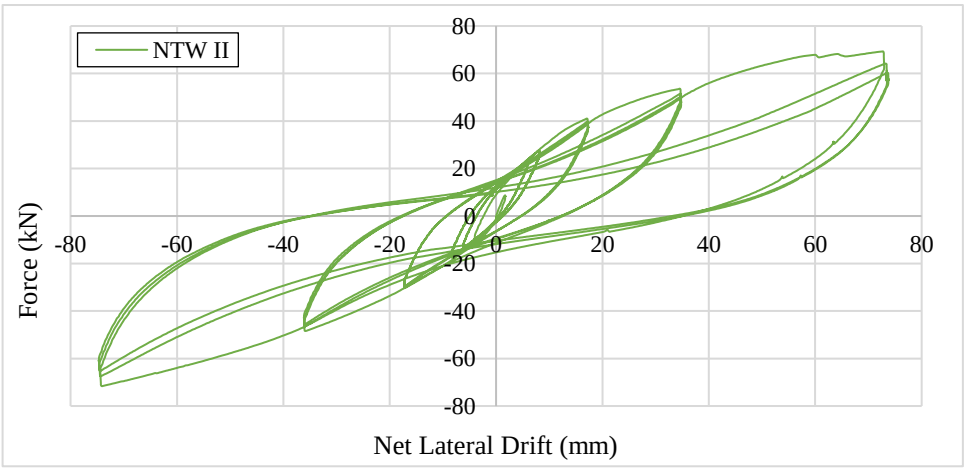

Figure 2.4. Hysteresis curve obtained from the experimental test of NTW II.

2.2.2. Connection Response

Connections are overdesigned such that shear deformation governs the behavior of experimented NTWs. As expected, no noticeable deformation occurred in connections.

2.3. Modeling the Experimental Test Setup

The experimental test setup is modeled in CSI Perform3D with buckling restrained brace (BRB) elements, infinitely rigid bar elements, pin connections, and fixed supports as shown in Figure 2.5. Key parameters referred to in analytical modeling of the wall are explained in Figure 2.6.

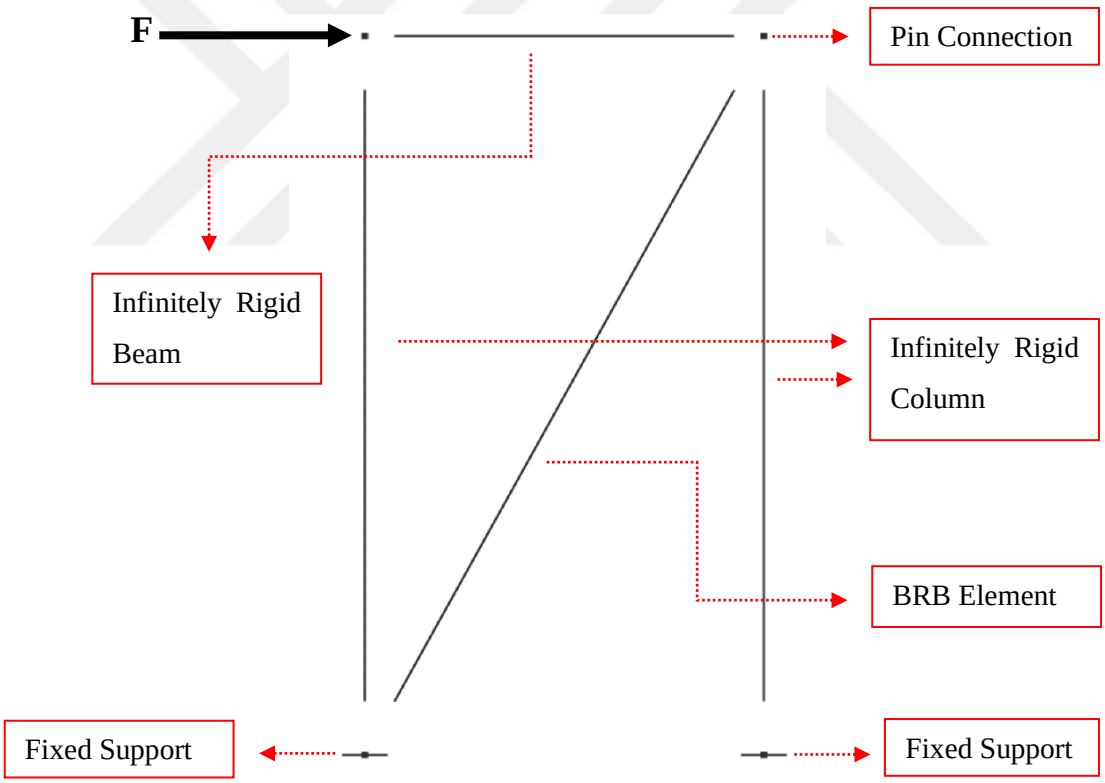

Figure 2.5. Experimental test model in CSI Perform3D.

The properties of the BRB elements are determined in a way that the net lateral displacement values obtained from the CSI Perform3D model are approximately the same as the net lateral displacement values obtained from the experimental tests under the same loading.

The procedure followed while determining the properties of the BRB elements is explained in detail below. Initially, backbone curves (BC) corresponding to hysteresis curves obtained from the experimental tests for both NTWs are converted into bilinear backbone curves as shown in Figure 2.7. Then, lateral deformations of the NTWs are converted into axial deformations in BRB elements by

$$\delta' = L' - L = \sqrt{(x+\delta)^2 + y^2} - \sqrt{x^2 + y^2}\,, \tag{2.1}$$

where L represents the initial length of the BRB element and L' represents the length of the BRB element after the force applies (see Figure 2.6 for the geometric representations of the parameters involved) and they are calculated as

$$L = \sqrt{x^2 + y^2}\,, \tag{2.2}$$

$$L' = \sqrt{(x+\delta)^2 + y^2}\,, \tag{2.3}$$

where x and y are width and height of the NTW, respectively. Finally, the applied force on the representative BRB element is calculated as

$$F' = \frac{F}{\cos\theta}, \tag{2.4}$$

where F is the force applied to the NTW by the hydraulic jack. Backbone curves obtained for each NTW are presented in Figure 2.8 and Figure 2.9, along with the test results they are representative of. The force time history of the experiments is provided in Figure 2.10.

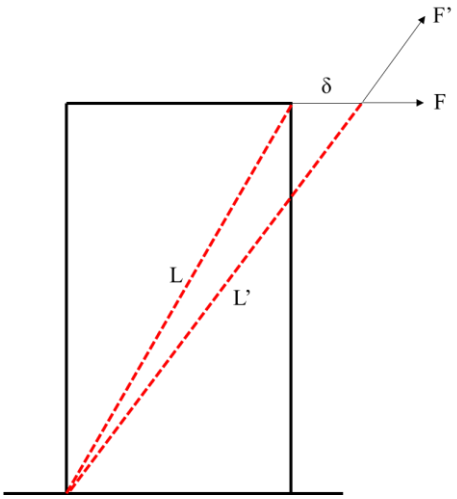

Figure 2.6. Representative experimental test setup.

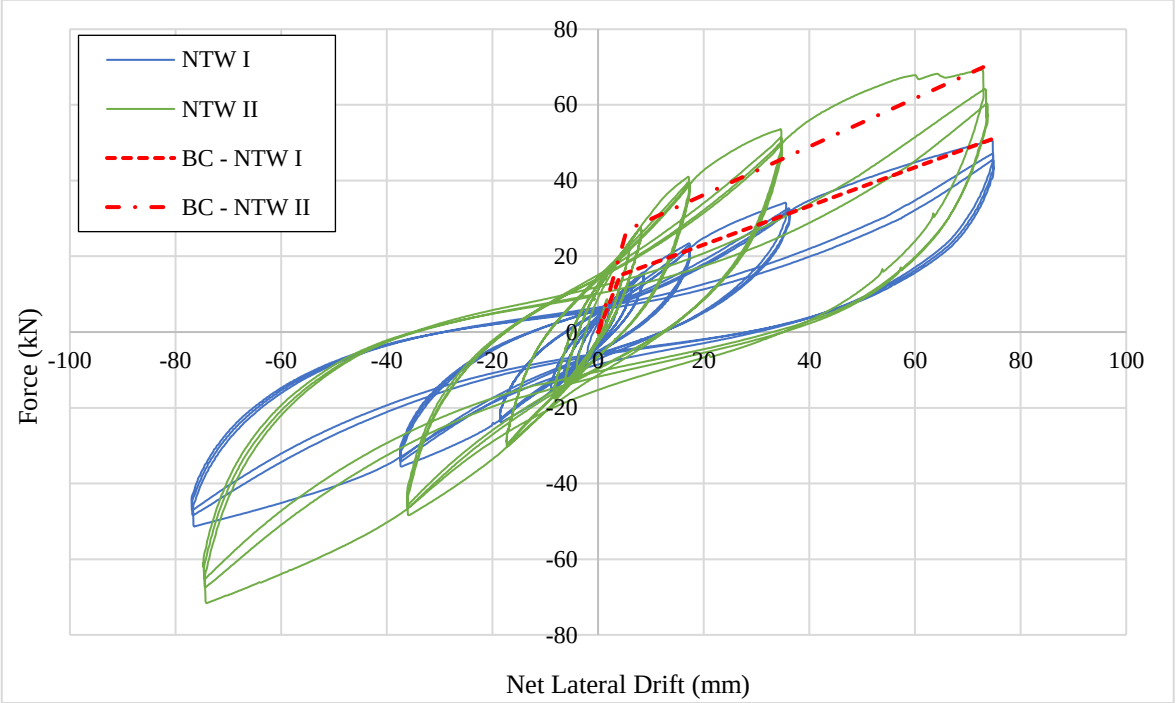

Figure 2.7. Hysteresis curves obtained from experimental tests and corresponding backbone curves.

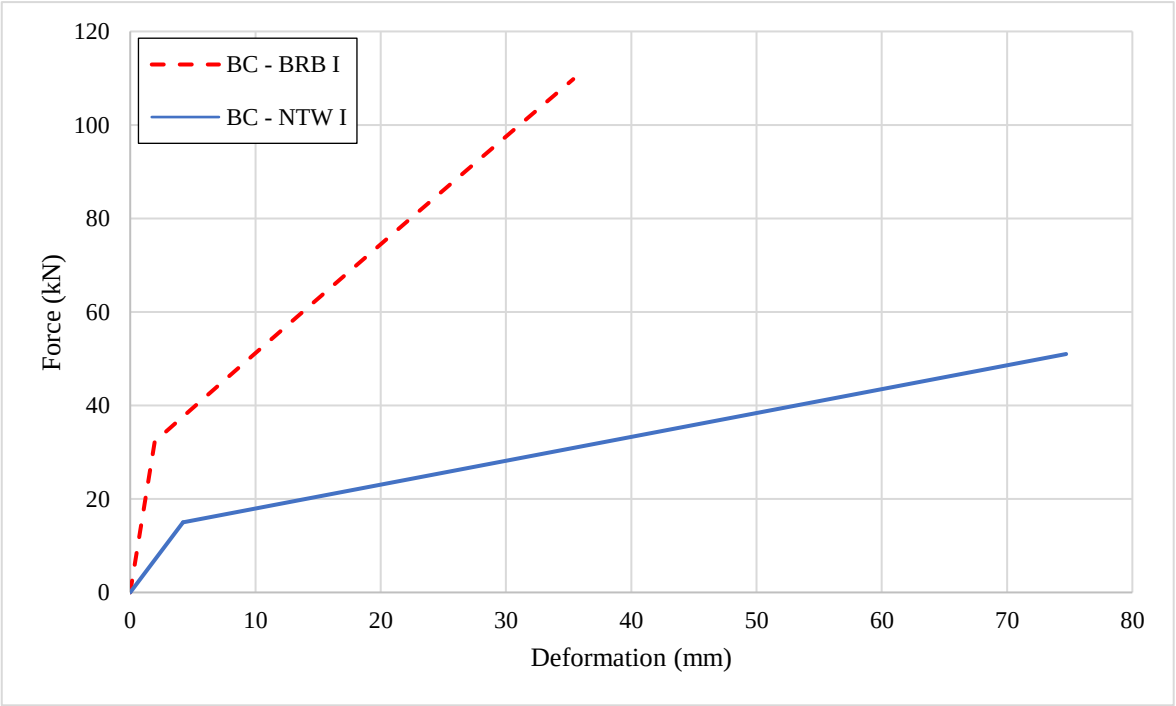

Figure 2.8. Backbone curve generated based on experiment results of NTW I, and backbone curve of representative brace element used in CSI Perform3D model of the experiment.

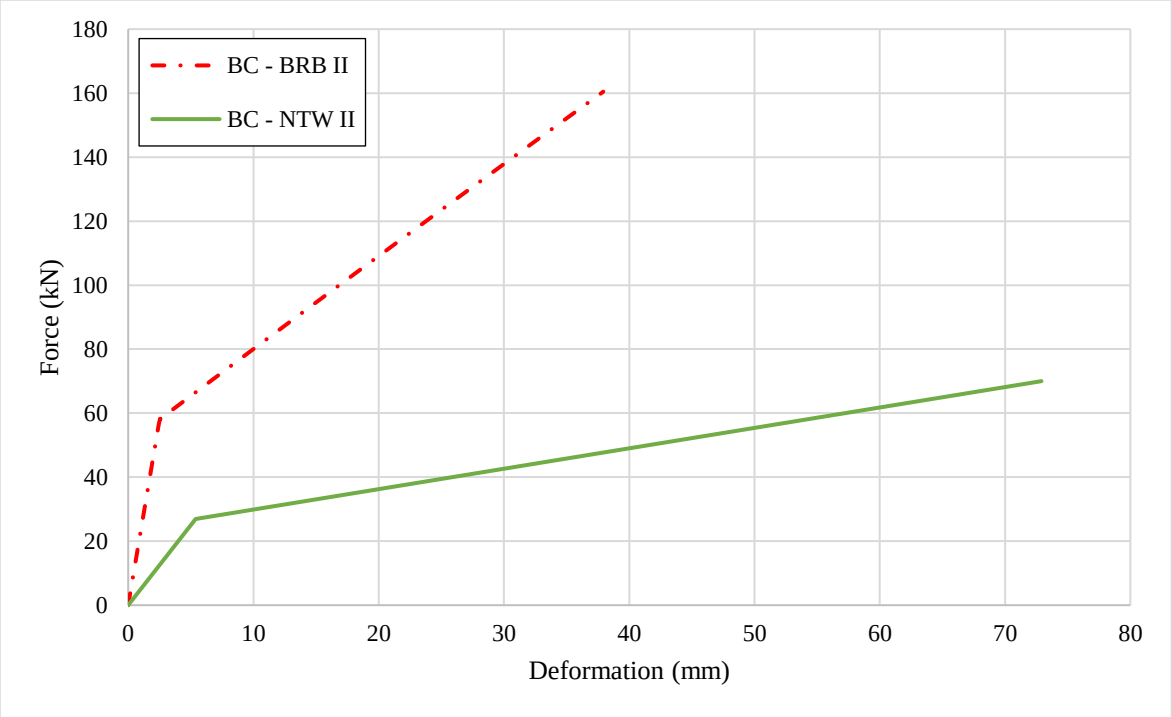

Figure 2.9. Backbone curve generated based on experiment results of NTW II, and backbone curve of representative brace element used in CSI Perform3D model of the experiment.

2.4. Results of CSI Perform3D Models of the Experimental Tests

The results for the two walls are summarized in Figure 2.11 through Figure 2.17. The net lateral displacement values for NTW I and NTW II for both experimental tests and CSI Perform3D models are presented in Figure 2.11 and Figure 2.15. BRB I and BRB II are referred to as the computational models of NTW I and NTW II generated in CSI Perform3D, respectively. Even though an exact match of experimental tests results and results obtained from models generated in CSI Perform3D is not possible to achieve due to limitations of the software, obtaining an adequately good match of displacements under the same loading is prioritized. However, prioritizing matching displacements resulted in unmatching dissipated energies as shown in Figure 2.13 and Figure 2.17.

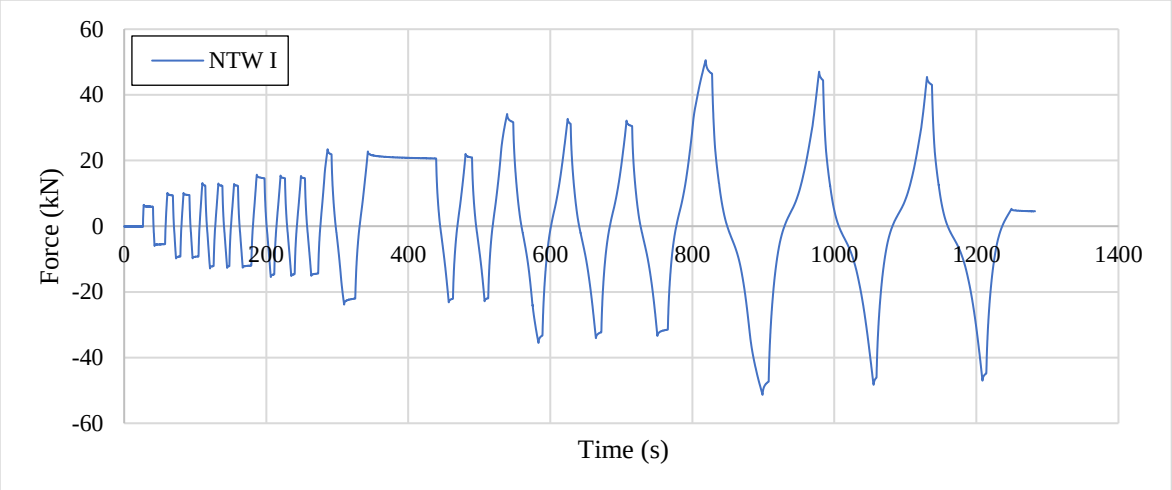

Figure 2.10. Force record of the experiment of NTW I.

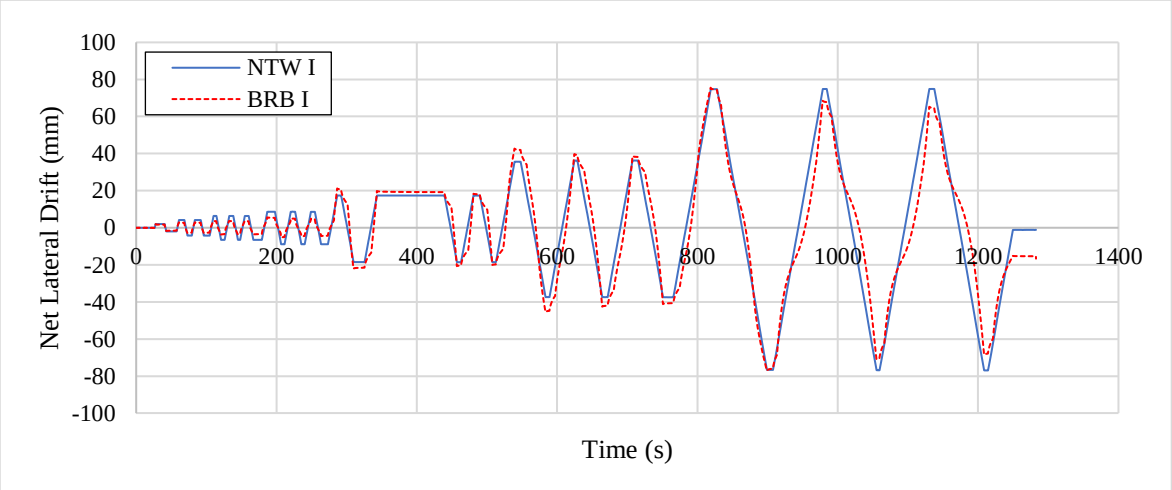

Figure 2.11. Displacement results of the experiment (NTW I) and the computational model (BRB I).

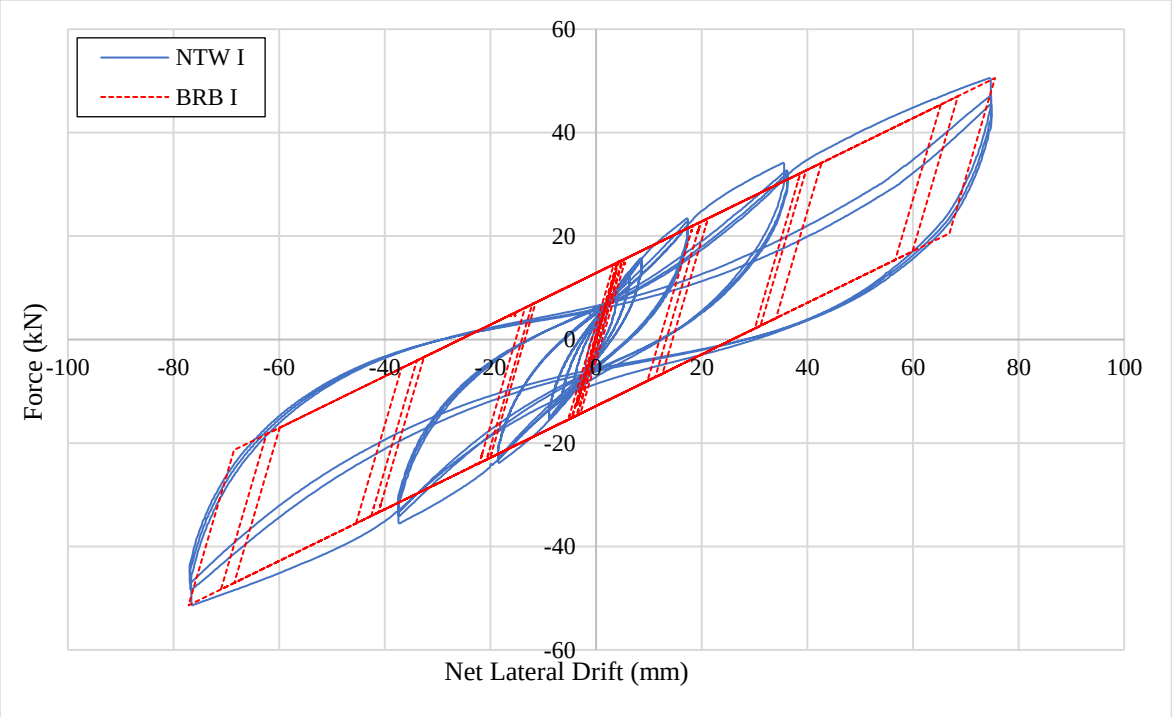

Figure 2.12. Hysteresis curves of the experiment (NTW I) and the computational model (BRB I).

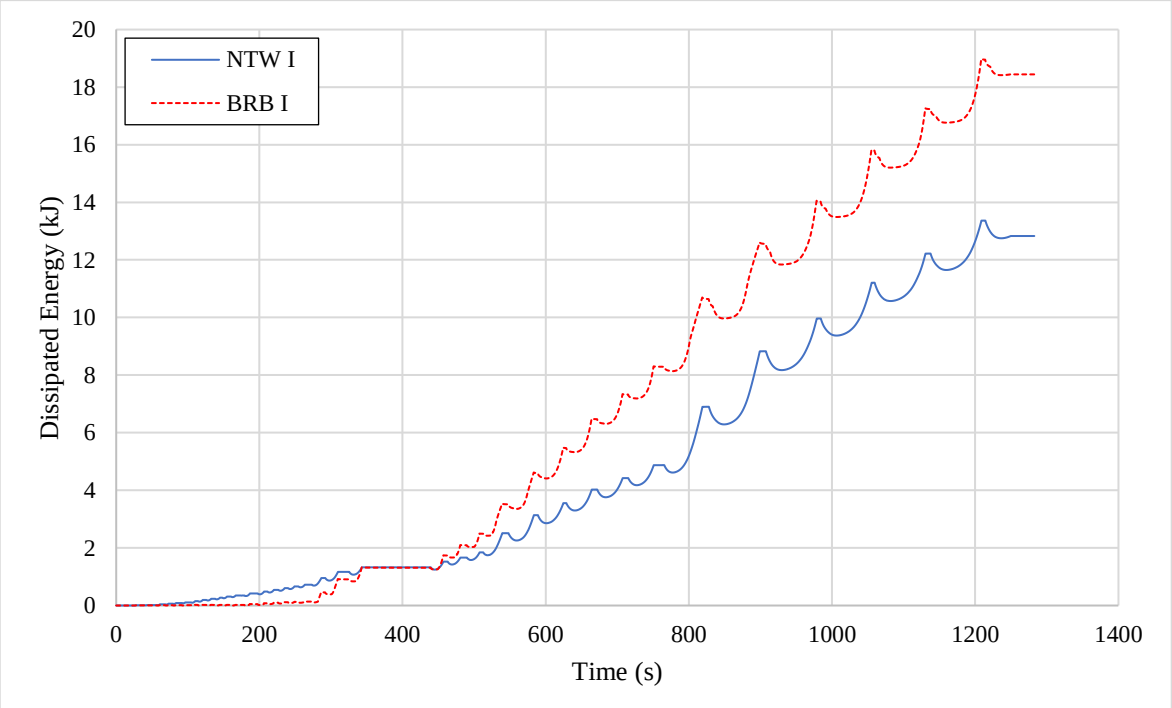

Figure 2.13. Dissipated energies of the experiment (NTW I) and the computational model (BRB I).

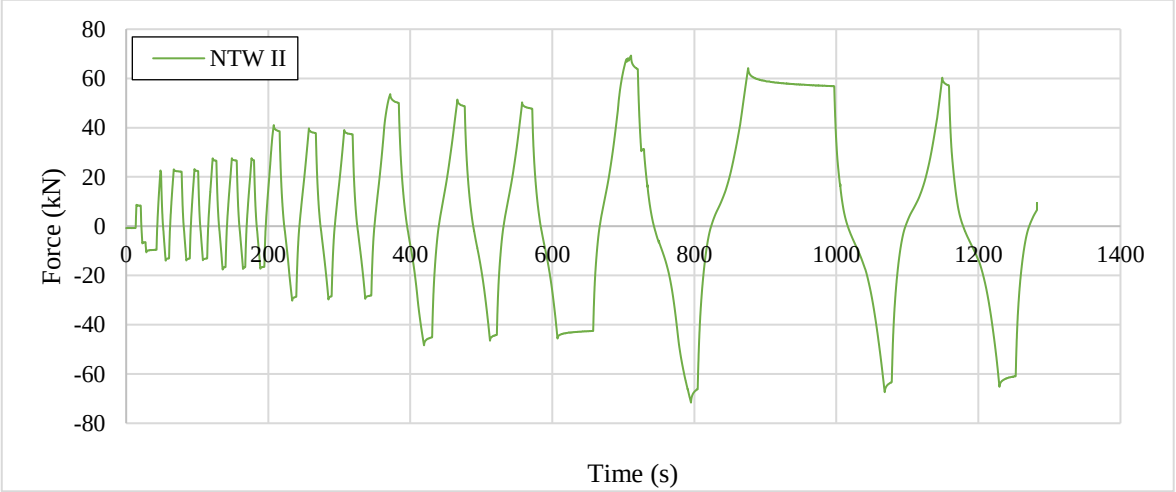

Figure 2.14. Force record of the experiment of NTW II.

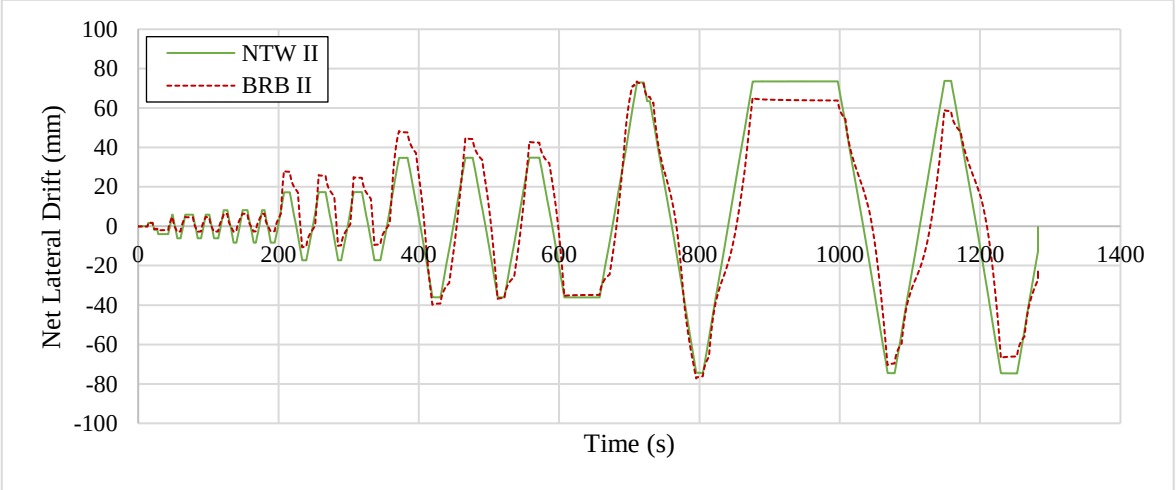

Figure 2.15. Displacement results of the experiment (NTW II) and the computational model (BRB II).

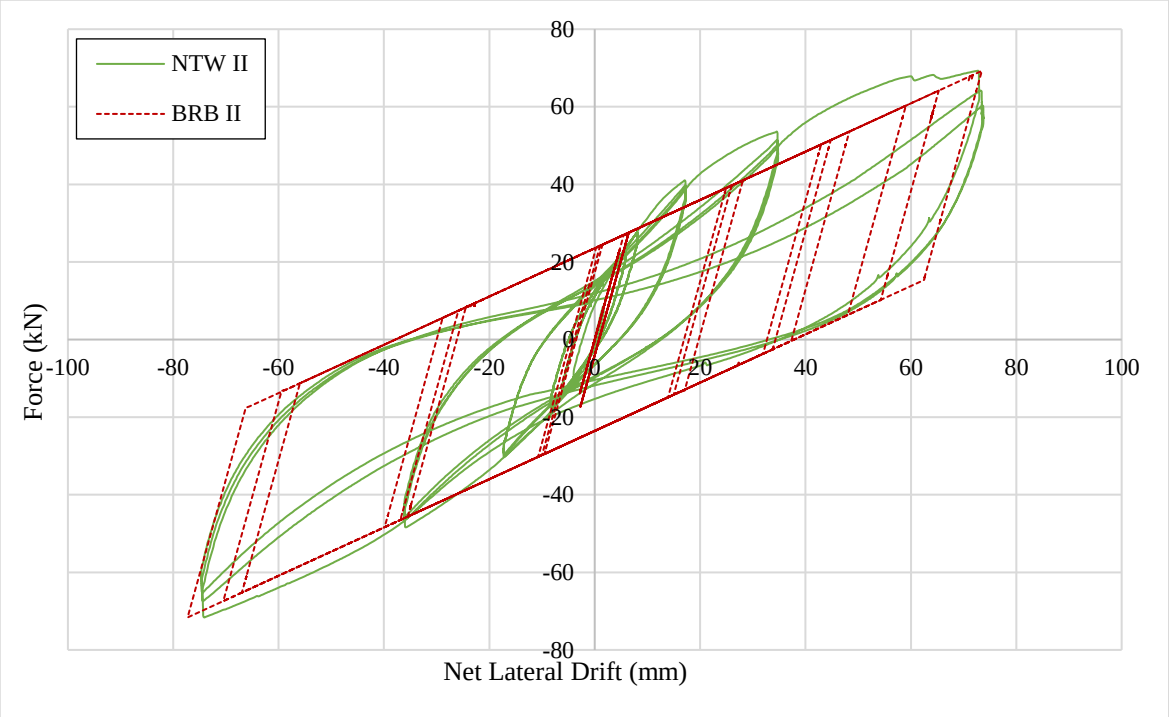

Figure 2.16. Hysteresis curves of the experiment (NTW II) and the computational model (BRB II).

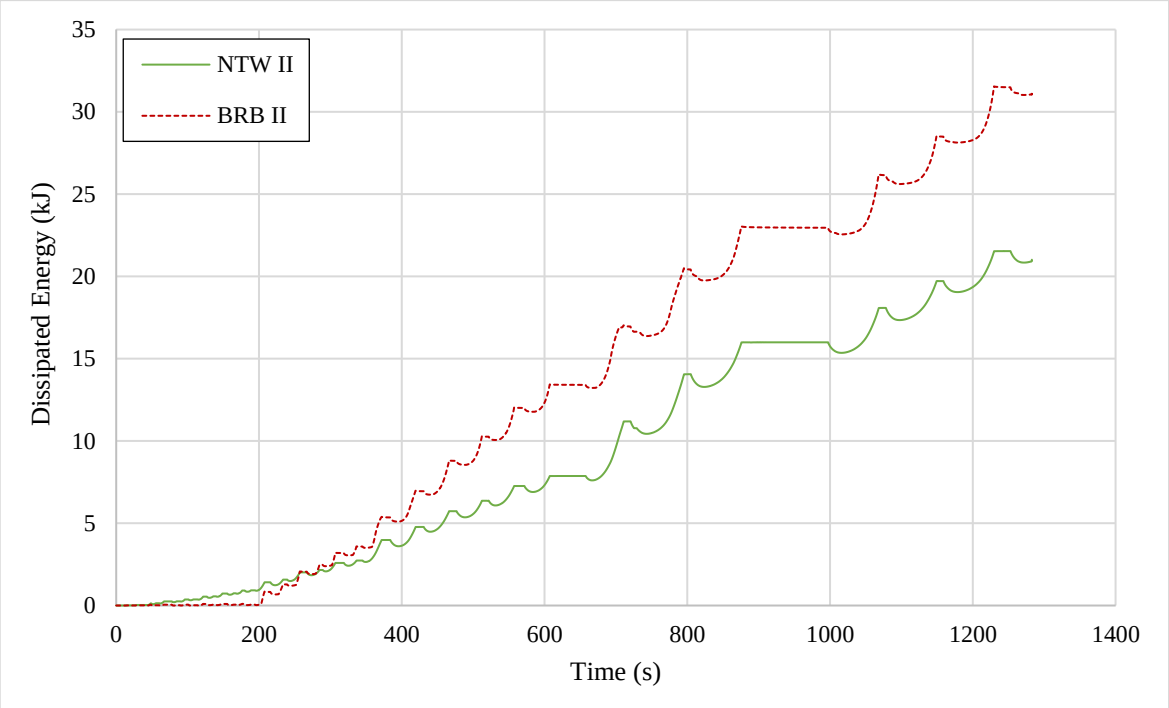

Figure 2.17. Dissipated energies of the experiment (NTW II) and the computational model (BRB II).

2.5. Parameters for Braces used in CSBs

Assumptions and calculations made in order to determine the parameters of the BRB elements used in the two CSBs are presented in this chapter. In previous chapters, the parameters for the BRB elements that represent the behavior of the NTWs used in the experimental tests with dimensions of 2860 mm height and 1500 mm width are presented for each NTW specimen. The backbone curves that are determined for each NTW specimen in the previous chapter are modified according to the dimensions of the NTWs used in the two case study buildings.

The modifications because of the change in height and width are made according to two assumptions: the deformation of the NTW is due to shear only and strength of the panel is reached when a limit angular deformation of the panel is reached. Therefore, the shear strength of NTW does not depend on the height of the panel, and the stiffness of the panel is inversely proportional to its height. Additionally, strength and stiffness are linearly proportional to the width of the NTWs.

The placement of NTWs for CSB I and CSB II are shown in Figure 2.18 and Figure 2.19, respectively. In order to demonstrate the method of modification properties of BRB elements used in CSB I are presented. For the first story of CSB I, the height and width of the NTWs that are used in the CSI Perform3D model are 4500 mm and 6000 mm, respectively. On the upper floors, the height of the NTWs drops to 3500 mm with the same width value. Backbone curves converted for the first structural model which simulates the seismic response of retrofitted CSB I with NTW I are presented in Figure 2.20 and Figure 2.21. Backbone curves converted for the second structural model which simulates the seismic response of retrofitted CSB I with NTW II are presented in Figure 2.22 and Figure 2.23.

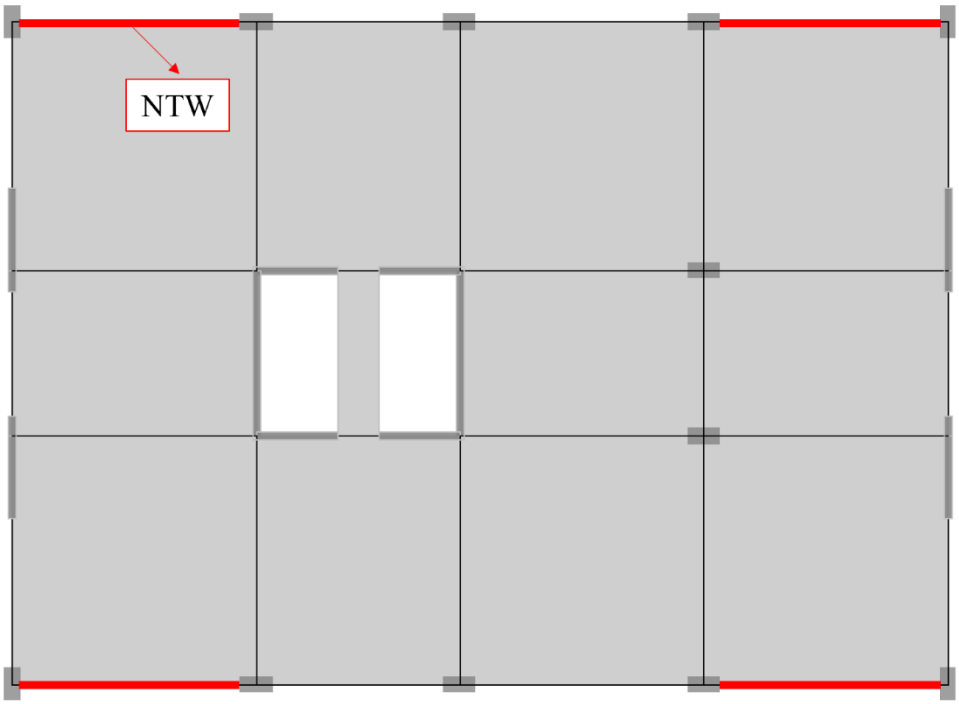

Figure 2.18. Positions of NTWs in plan view of CSB I.

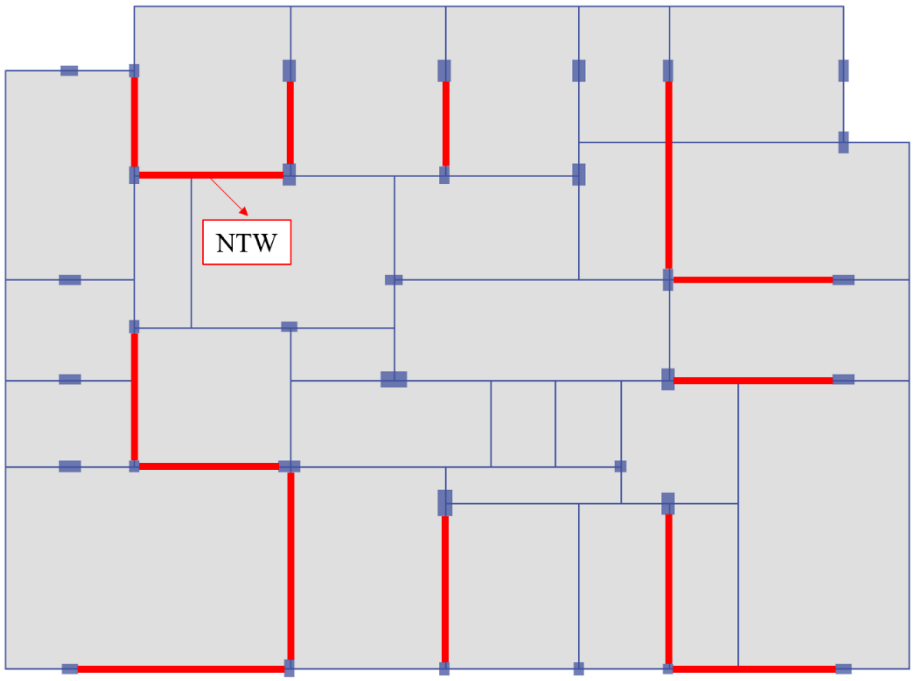

Figure 2.19. Positions of NTWs in plan view of CSB II.

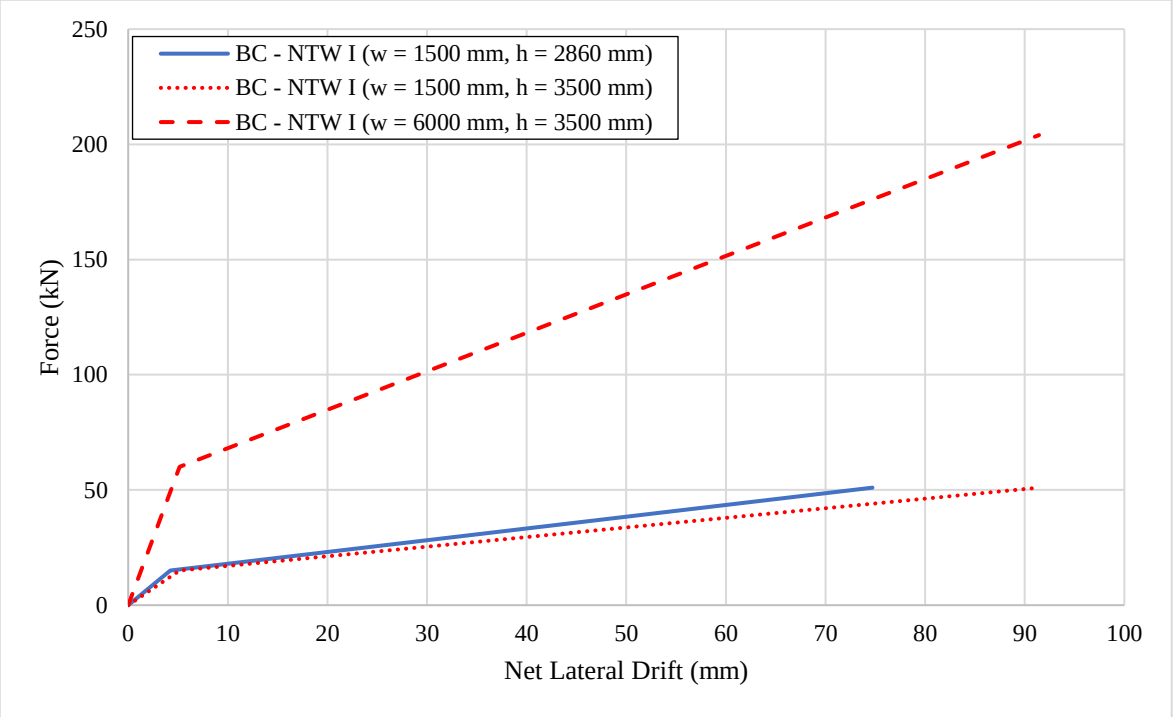

Figure 2.20. Backbone curves of NTW I used in CSB I for 3.5 m height and different width values.

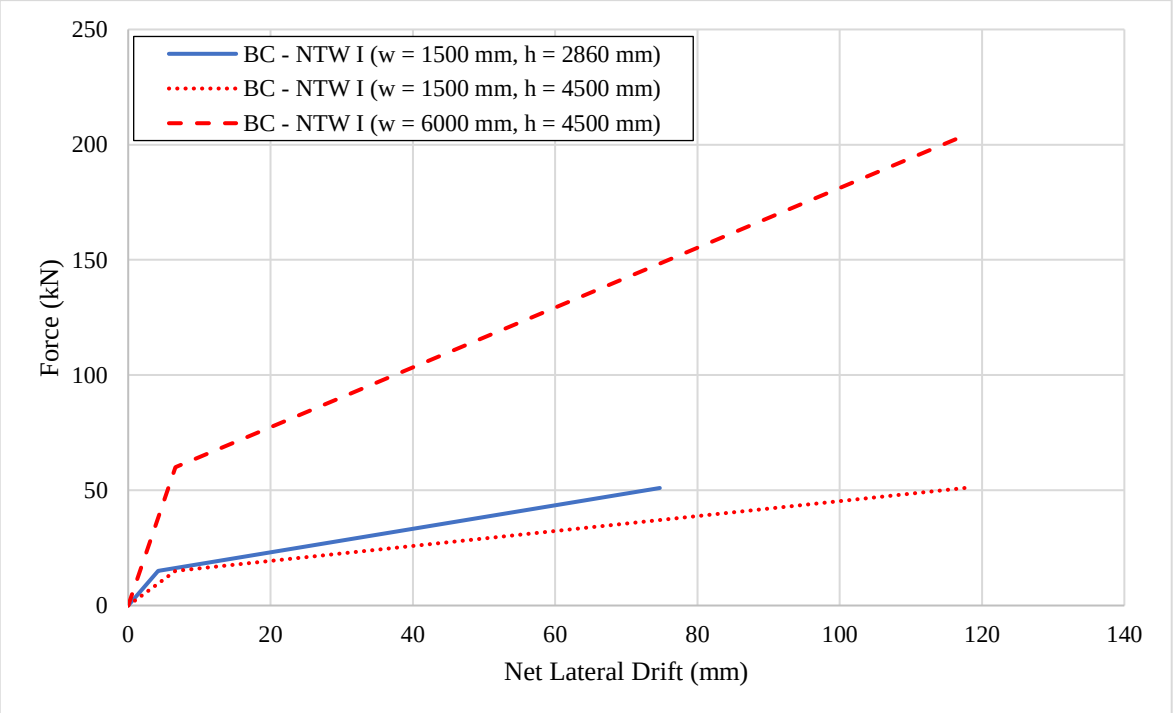

Figure 2.21. Backbone curves of NTW I used in CSB I for 4.5 m height and different width values.

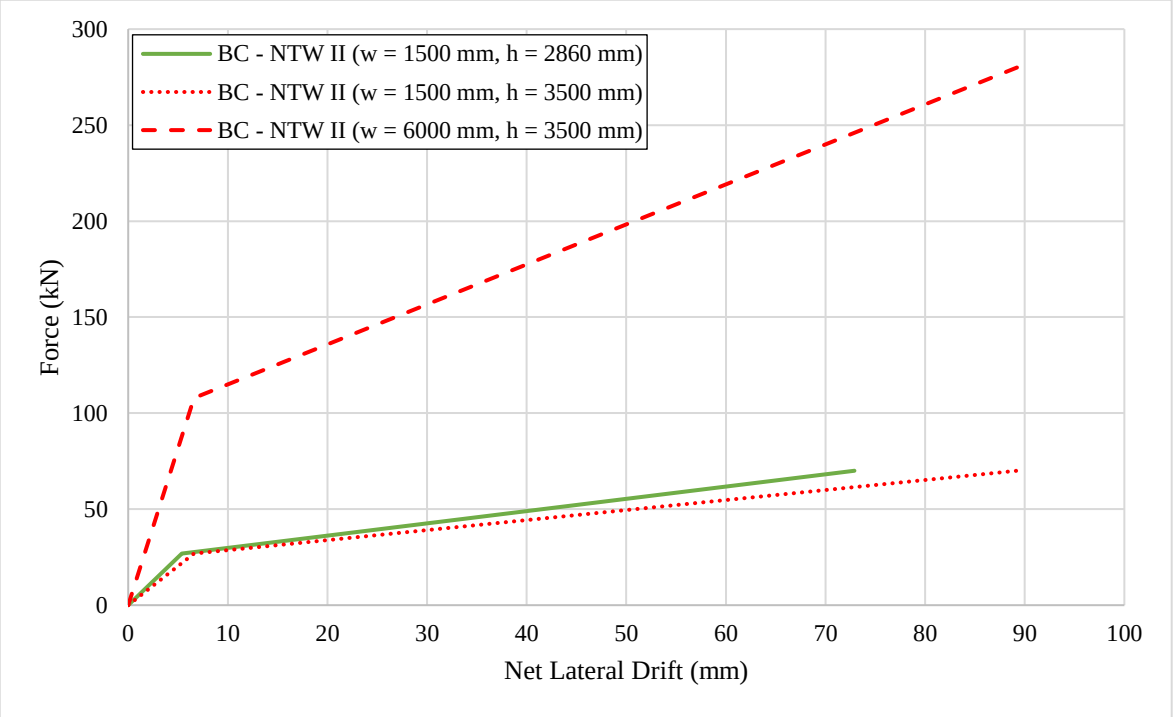

Figure 2.22. Backbone curves of NTW II used in CSB I for 3.5 m height and different width values.

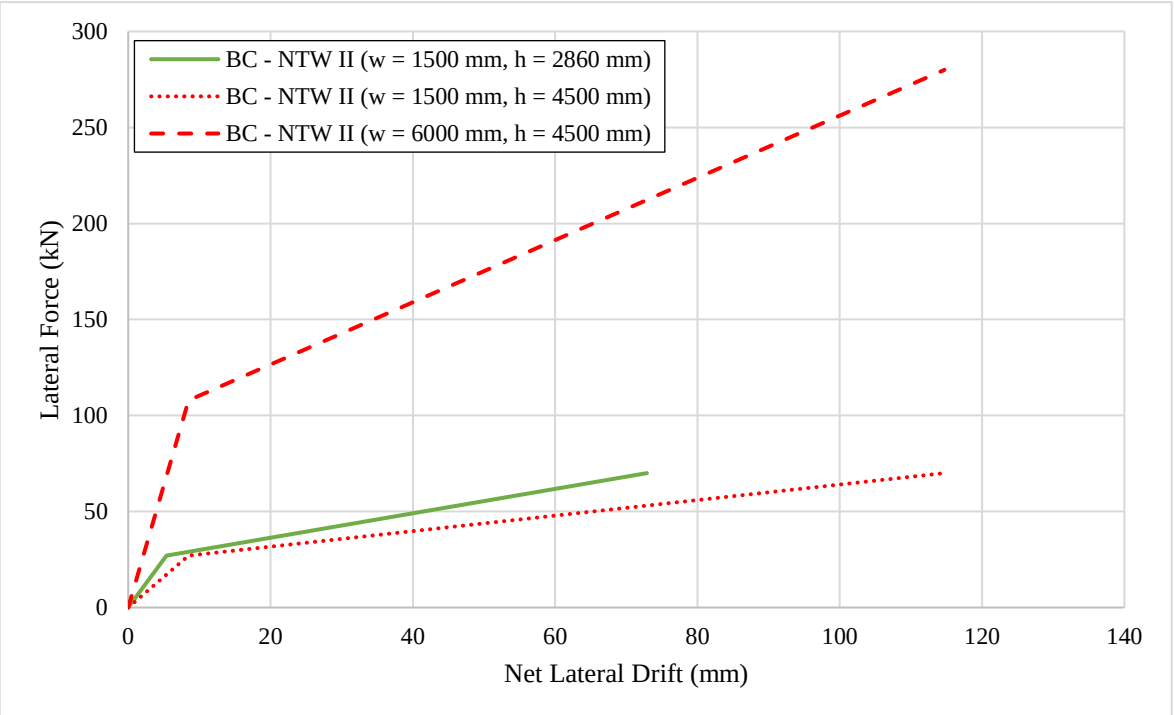

Figure 2.23. Backbone curves of NTW II used in CSB I for 4.5 m height and different width values.

3. NONLINEAR MODELING AND ANALYSIS

3.1. CSB Properties

Two substandard reinforced concrete residential case study buildings are investigated within the scope of this research. The buildings are assumed to be located at coordinates 40°58’50.96” N, 28°43’22.8” E in Avcilar, Istanbul, shown representatively in Figure 3.1, on site class ZD soil.



Figure 3.1. The case study buildings’ location and source-to-site distance [20].

The total height of the first case study building shown in Figure 3.2 is 18.5 m from the foundation to the roof, and each story has a 3.5 m height except the first story which has a 4.5 m height (Figure 3.3). The structural design of CSB I is initially done in compliance with TBSC 2018 [17] with the assumption that concrete class of C25 and steel class of S420 will be used during construction. However, to represent material properties often encountered in pre-2000 common building stock, the characteristic compressive strength of concrete is assumed to be 10 MPa and characteristic yield strength of reinforcement is assumed to be 220 MPa. The lateral load resisting system of CSB I consists of two C-shaped core walls and four rectangular walls placed around the perimeter of the structure. Plan area of the building is 368 m^2 (Figure 3.4). Beams have 500 mm x 600 mm cross-sections, except

for the beams between core walls which have 400 mm x 600 mm cross-sections. Columns have 400 mm x 800 mm cross-sections. The thickness of slabs and walls are 150 mm and 200 mm, respectively. Finally, clear cover is assumed to be 15 mm.



Figure 3.2. 3D view of CSB I.

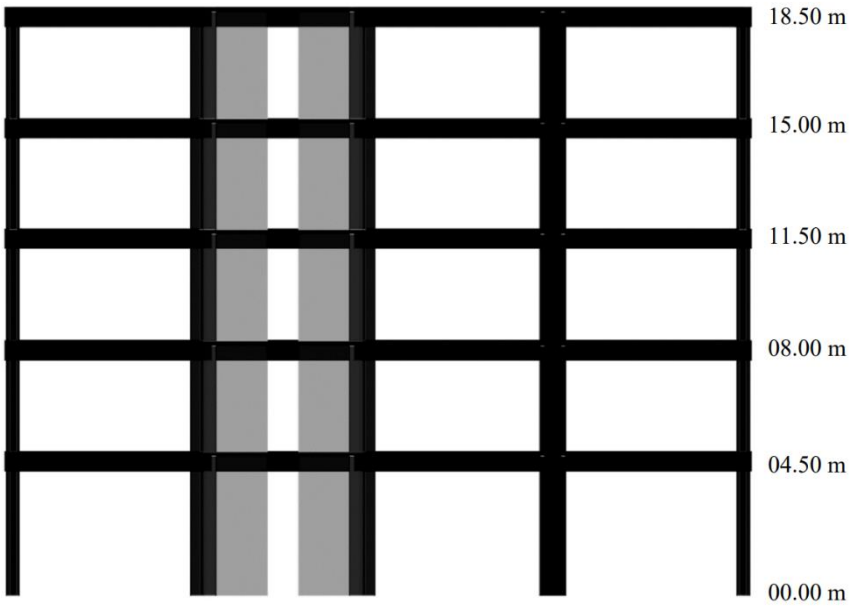

Figure 3.3. Elevation view of CSB I.

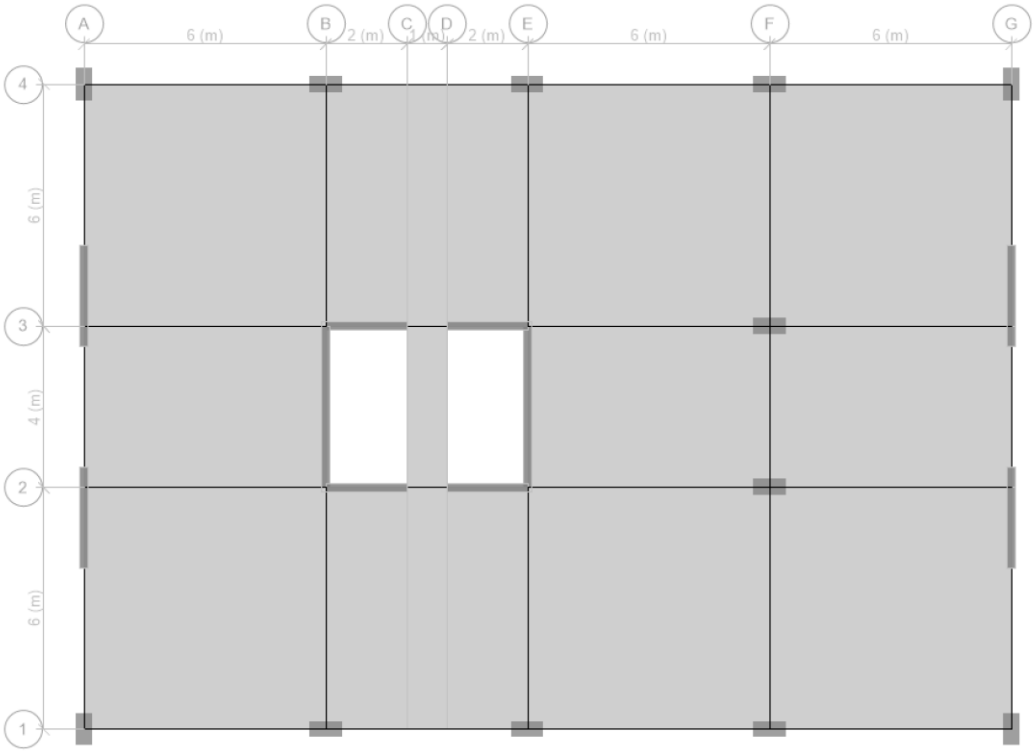

Figure 3.4. Floor plan view of CSB I.

The second case study building shown in Figure 3.5 is a 6-story building with 3 m story height as shown in Figure 3.6 and a plan area around 315 m^2 as shown in Figure 3.7. CSB II is a RC frame building which is constructed before recent earthquake design codes and has poor material quality same as CSB I (f_{ck} = 10 MPa, f_{sy} = 220 MPa). Beams have 300 mm x 450 mm cross-sections and columns have varying cross-sections which are relatively small when compared to the cross sections enforced by TBSC 2018. Also, since the structural system is not symmetric in any of the directions, and the columns and their orientations are not distributed evenly, CSB II has an irregular structural system. The thickness of slabs and clear cover are 150 mm and 15 mm, respectively.

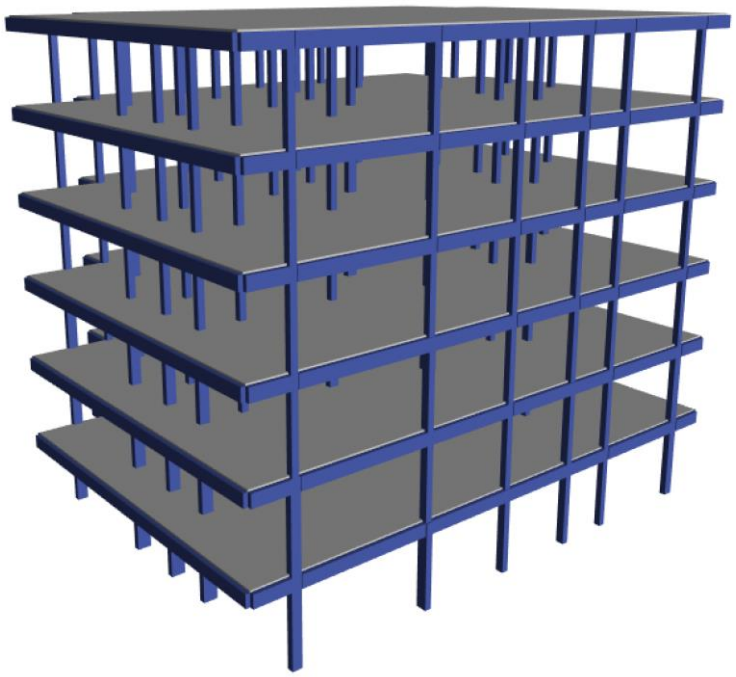

Figure 3.5. 3D view of CSB II.

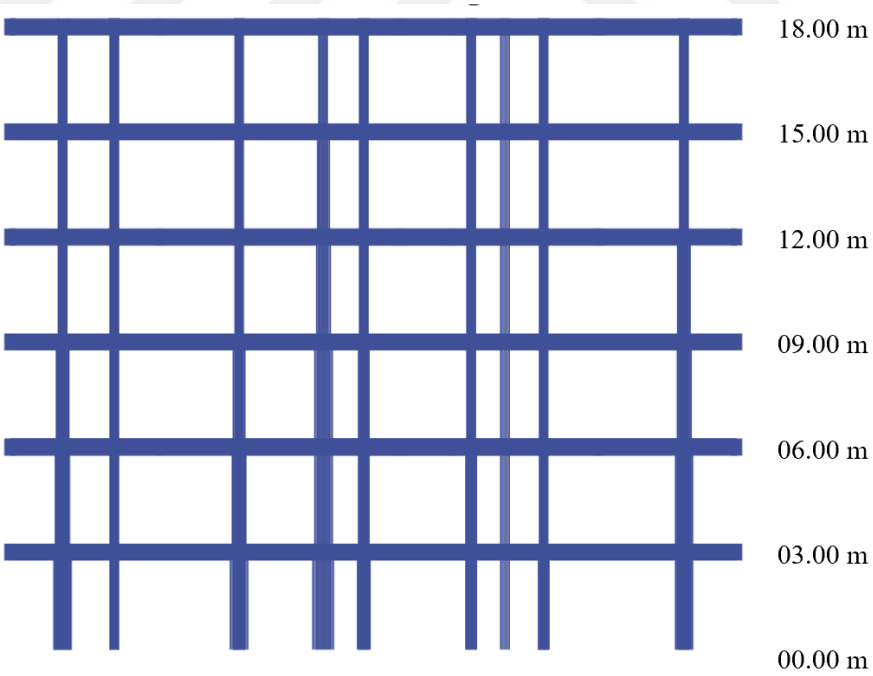

Figure 3.6. Elevation view of CSB II.

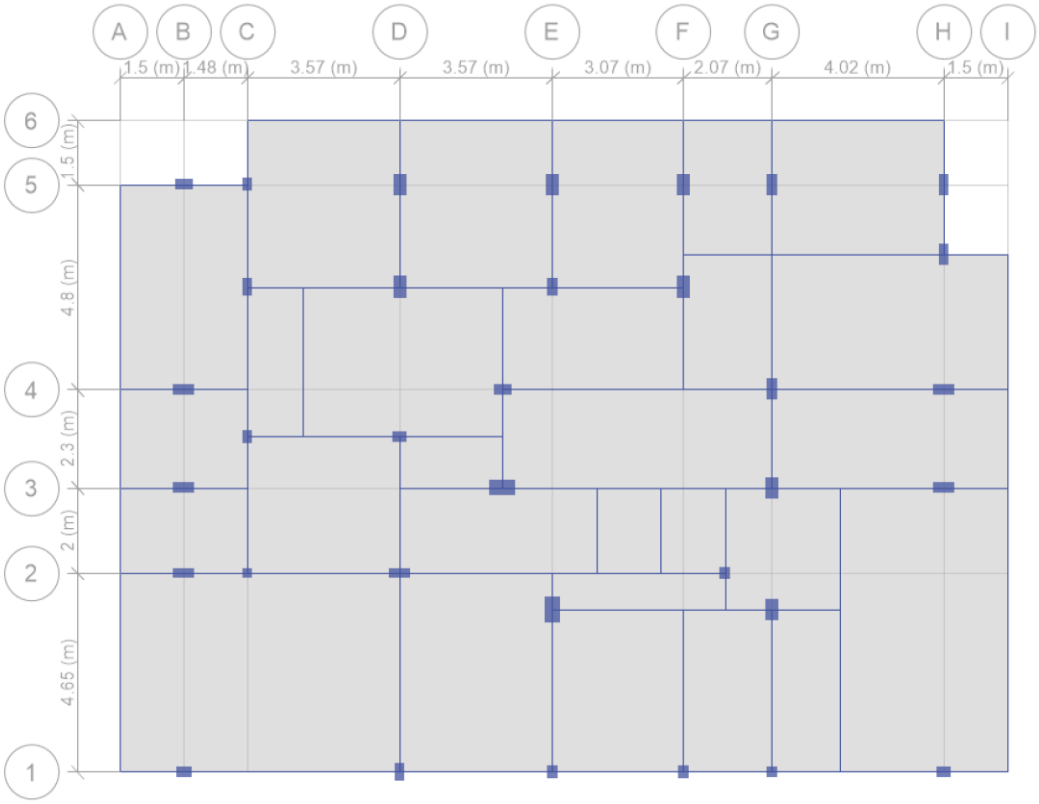

Figure 3.7. Floor plan view of CSB II.

3.2. Nonlinear Models

Reliable representation of nonlinear behavior of a structure under seismic loading is a complex problem. Moreover, uncertainty in the expected ground motion characteristics is another difficulty that further complicates the process. Even though it is more time-consuming and computationally demanding, NLTHA provides reliable results on the seismic performance of structures. Besides, seismic codes allow engineers to make realistic and safe assumptions while implementing NLTHA.

In this study, nonlinear modeling, and analysis of the CSBs are conducted using CSI Perform3D software according to the specifications in TBSC 2018. Three nonlinear models for each CSB are generated in CSI Perform3D. The first structural models are generated to simulate the seismic response of CSBs as they are, second and third structural models are generated to simulate the seismic response of retrofitted versions of CSBs with NTW I and NTW II, respectively.

In all nonlinear models, the foundation is assumed to rest on fixed supports, slabs are modeled with elastic slab elements using the rigid diaphragm assumption, as typically suggested.

From now on, the CSBs without any retrofitting will be called Plain RC building, buildings retrofitted with NTW I will be called RET I, building retrofitted with NTW II will be called RET II.

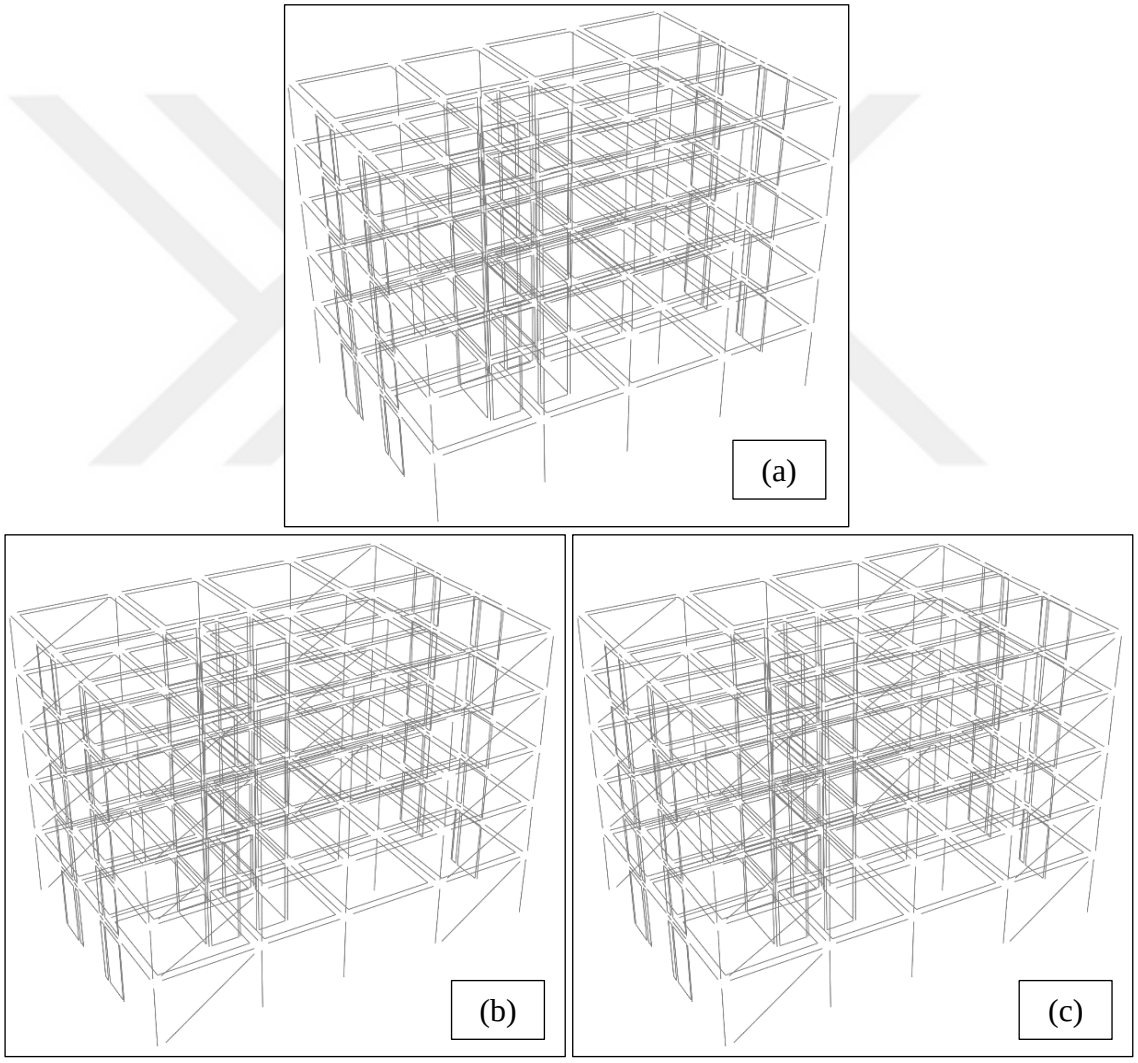

Figure 3.8. 3D views of nonlinear models of CSB I. (a)Plain RC, (b) RET I, (c) RET II.

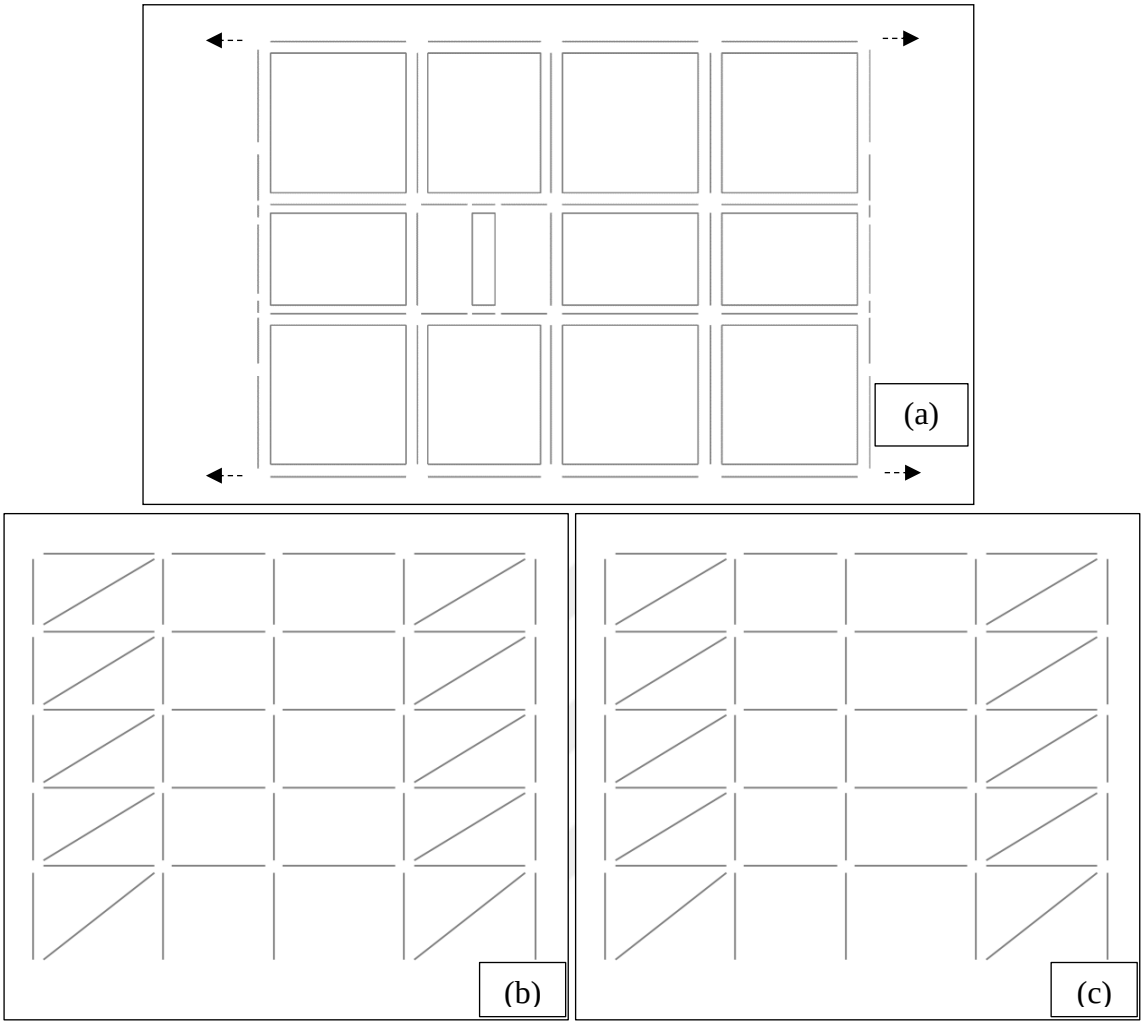

Figure 3.9. (a) Plan view of RET I and RET II of CSB I (b) A-A section (c) B-B section.

3D views of the three nonlinear models of CSB I are shown in Figure 3.8. Also, positions of NTWs to be installed in CSB I are presented in Figure 3.9 along with Figure 2.18. Similarly, 3D views of the three nonlinear models of CSB II are shown in Figure 3.10. Positions of the NTWs to be installed in CSB II is shown in Figure 2.19.

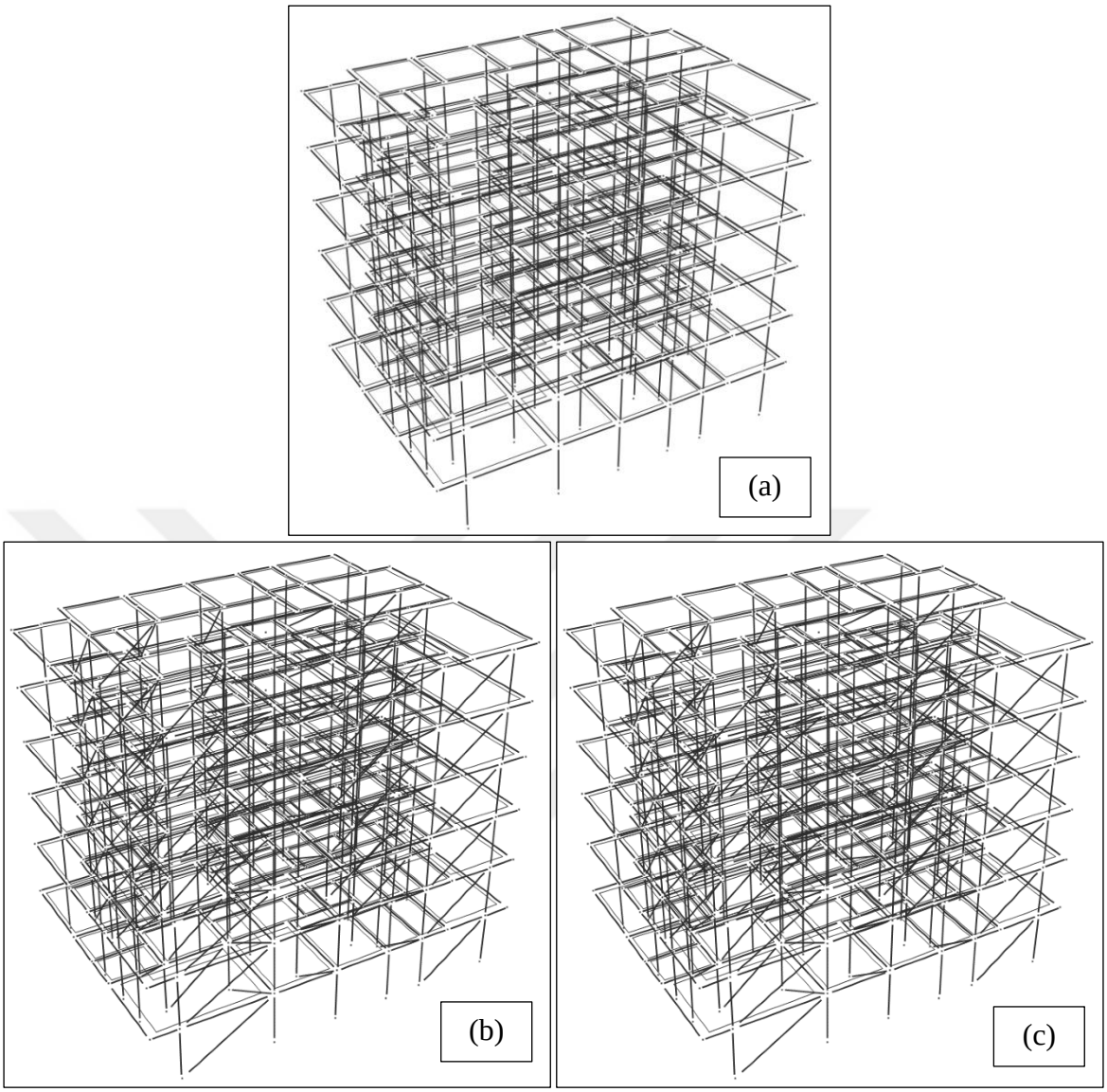

Figure 3.10. 3D views of nonlinear models of CSB II. (a)Plain RC, (b) RET I, (c) RET II.

3.3. Nonlinear Modeling

3.3.1. Material Properties

TBSC 2018 specifies that existing material strength values shall be used for the seismic performance assessment of existing buildings. In this study, existing characteristic compressive strength of concrete is assumed to be 10 MPa and characteristic yield strength of reinforcement is assumed to be 220 MPa in both CSBs.

3.3.1.1 Elastic Shear Modulus of Structural Walls. Since no nonlinear shear deformation is expected in structural walls, shear behavior is modeled linear elastically by defining an Elastic Shear Material in CSI Perform3D. The shear modulus of structural walls in CSB I is calculated as

$$G_c = \frac{E_c}{2(1+\nu_c)}, \tag{3.1}$$

and tangent modulus of elasticity of concrete, E_c calculated as

$$E_c = 3250\sqrt{f_{ck}} + 14000, \tag{3.2}$$

where f_{ck} is characteristic compressive strength of concrete used.

However, using gross sectional rigidities of RC structural members is not realistic since cracking of concrete due to reversed cyclic loading is not considered. Therefore, it results in an overestimation of structural rigidity under seismic loading. Thus, the corresponding stiffness modifier presented in Table 3.1 is applied according to TBSC 2018.

Table 3.1. Stiffness modifiers of reinforced concrete elements.

RC Structural Element	Effective Rigidity	
Wall-Slab (In-Plane)	Axial	Shear
Structural Wall	0.50	0.50
Basement Wall	0.80	0.50
Slab	0.25	0.25
Wall-Slab (Out of Plane)	Bending	Shear
Structural Wall	0.25	1.00
Basement Wall	0.50	1.00
Slab	0.25	1.00
Line Element	Bending	Shear
Coupling Beam	0.15	1.00
Moment Frame Beam	0.35	1.00
Moment Frame Column	0.70	1.00
Wall (Modeled as Equivalent Line Element)	0.50	0.50

3.3.1.2 Elastic Modulus for Slabs. In this study, slabs are modeled elastically, and the corresponding stiffness modifier which is provided in Table 3.1 is used to simulate effective flexural rigidities of slabs.

3.3.1.3 Concrete. A theoretical stress-strain model which is generated according to the specifications of TBSC 2018 for both unconfined and confined concrete is used in NLTHA [18]. To generate the confined and unconfined concrete stress-strain relationships defined in the model, compressive stress of confined concrete, f_c is calculated as

$$f_c = \frac{f_{cc} x r}{r - 1 + x^r}, \tag{3.3}$$

where the coefficient x which represents the ratio of any strain to strain at ultimate compressive strength of confined concrete is calculated as

$$x = \frac{\varepsilon_c}{\varepsilon_{cc}}, \tag{3.4}$$

where strain at ultimate compressive strength of confined concrete, ε_{cc} is calculated as

$$\varepsilon_{cc} = \varepsilon_{co}\left[1 + 5\left(\lambda_c - 1\right)\right]. \tag{3.5}$$

As well as the coefficient r which represents ratio of tangent modulus to difference of tangent and secant modulus is calculated as

$$r = \frac{E_c}{E_c - E_{\text{sec}}}, \tag{3.6}$$

where secant modulus of elasticity of reinforcement, E_{sec} is expressed as

$$E_{\text{sec}} = \frac{f_{cc}}{\varepsilon_{cc}}, \tag{3.7}$$

where tangent modulus of elasticity of concrete, E_c is expressed as

$$E_c = 5000\sqrt{f_{co}}\,. \tag{3.8}$$

Furthermore, compressive strength (peak stress) of confined concrete, f_{cc} is computed as

$$f_{cc} = \lambda_c f_{co}, \tag{3.9}$$

where confined concrete strength modifier, λ_c is expressed as

$$\lambda_c = 2.254\sqrt{1+7.94\frac{f_e}{f_{co}}} - 2\frac{f_e}{f_{co}} - 1.254, \tag{3.10}$$

where effective confining pressure in each direction, f_{ex} and f_{ey} are calculated as

$$f_{ex} = k_{ex}\rho_x f_{yw}, \tag{3.11}$$

$$f_{ey} = k_{ey}\rho_y f_{yw}, \tag{3.12}$$

where confinement effectiveness coefficient, k_e for each direction are calculated as

$$k_e = \left(1-\frac{\sum a_i^2}{6b_o h_o}\right)\left(1-\frac{s}{2b_o}\right)\left(1-\frac{s}{2h_o}\right)\left(1-\frac{A_s}{b_o h_o}\right)^{-1}. \tag{3.13}$$

The stress-strain relationships for unconfined and confined concrete are converted into polylines shown in Figure 3.11. Tensile strength and cyclic degradation of stress-strain behavior of concrete are not considered.

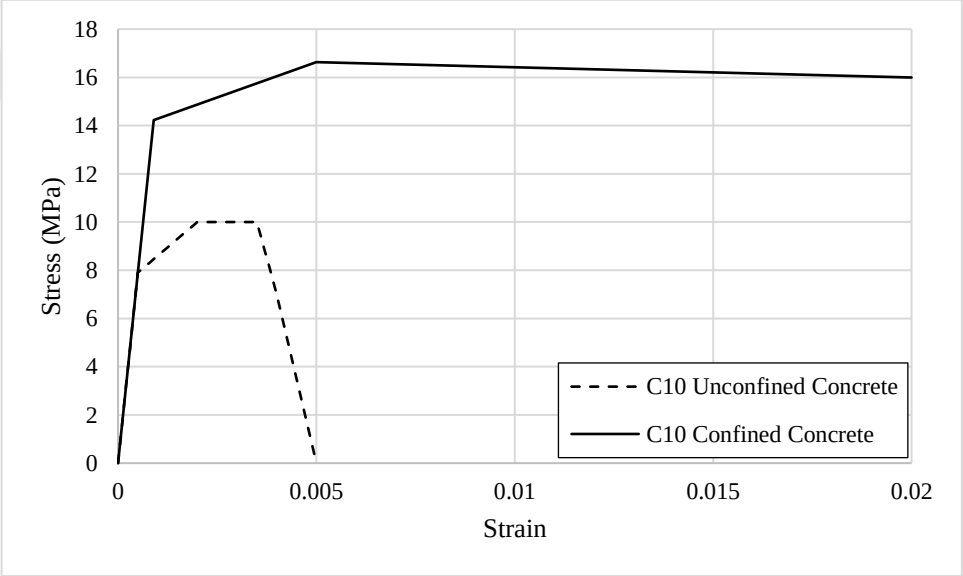

Figure 3.11. Linearized stress-strain relationship of concrete.

3.3.1.4 Reinforcement. The stress-strain model of the reinforcing steel used in CSBs is generated according to specifications of TBSC 2018. Modulus of elasticity, existing yield strength, and existing ultimate strength values are provided in Table 3.2. The buckling behavior of reinforcing steel is neglected in modeling. The stress-strain relationship that is plotted in Figure 3.12 is computed as

$$f_s = E_s \varepsilon_s , \qquad \left(\varepsilon_s \le \varepsilon_{sy}\right) \tag{3.14}$$

$$f_s = f_{sy} , \qquad \left(\varepsilon_{sy} < \varepsilon_s \le \varepsilon_{sh}\right) \tag{3.15}$$

$$f_s = f_{su} - \left(f_{su} - f_{sy}\right)\frac{\left(\varepsilon_{su} - \varepsilon_s\right)^2}{\left(\varepsilon_{su} - \varepsilon_{sh}\right)^2} . \qquad \left(\varepsilon_{sh} < \varepsilon_s \le \varepsilon_{su}\right) \tag{3.16}$$

Table 3.2. Mechanical properties of steel.

Steel Class	E_s (MPa)	$f_{sy}(MPa)$	ε_{sy}	ε_{sh}	ε_{su}	f_{su}/f_{sy}
B220C	200000	220	0.0011	0.011	0.12	1.2

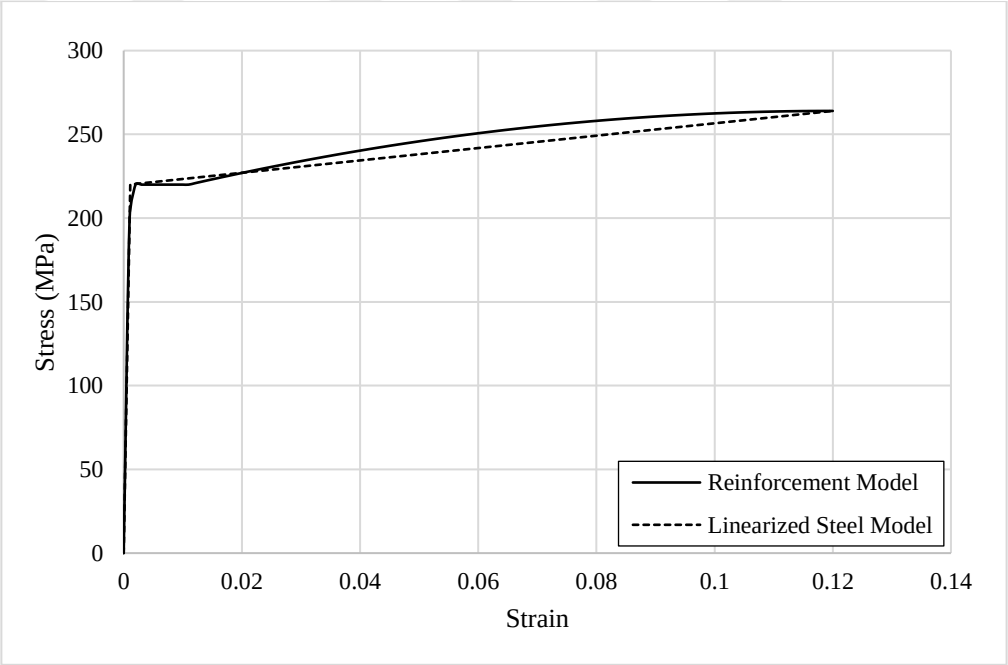

Figure 3.12. Stress-strain relationship of reinforcement.

3.3.2. Gravity Loads

Since the nonlinear response of columns and structural walls are controlled by axial loads in nonlinear analysis, realistic assignment of gravity loads is crucial to obtain a dependable nonlinear model. The expected gravity loads for the case study building consist of self-weight, superimposed dead loads, and live loads. While self-weight and superimposed dead loads are assigned directly to the model, live loads are assigned after reduction with live load participation factors according to TBSC 2018.

Self-weights for each structural member are calculated by the CSI ETABS analysis software and superimposed dead loads and reduced live loads are assigned to slabs as uniformly distributed loads. Magnitudes specified in TS 498 [19] for live loads are used. The magnitudes of all loads are listed in Table 3.3.

Table 3.3. Magnitude of uniform loads.

Type of Load	Uniform Load (kN/m^2)
Live Load Residential	2.00
Partition Walls	1.50
Floor finishes, bedding, and ceiling plaster	2.20
Snow Load	0.75

3.3.3. Seismic Loads

3.3.3.1 Determination of Target Spectrum. According to TBSC 2018, the DD2 earthquake hazard level should be used to define the design spectrum for seismic performance assessment of existing buildings. DD2 level is defined in TBSC 2018 as the standard design earthquake ground motion with a probability of exceedance of 10% in 50 years and reoccurrence period of 475 years. The spectral acceleration coefficients are obtained from the Turkish Earthquake Hazard Map website [20] for the hypothetical location of the CSBs at coordinates 40°58'50.96" N, 28°43'22.8" E. Spectral acceleration coefficients for this site are for a reference soil condition that falls into ZD soil class with first 30m depth shear wave velocity ($V_{s,30}$) of 360 m/s, under the DD2 earthquake level, and for 5% damping. The spectral acceleration coefficients assumed for the case study building are listed in Table 3.4.

Table 3.4. Spectral acceleration coefficients for the prototype building under DD2 level earthquake.

	S_S	S_1
DD2	1.271	0.343

Spectral acceleration coefficients obtained from the Turkish Earthquake Hazard Map website were then used to calculate design spectral acceleration coefficients which are calculated as

$$S_{DS} = S_S F_S, \tag{3.17}$$

$$S_{D1} = S_1 F_1, \tag{3.18}$$

considering local soil conditions at the hypothetical construction site. Assuming that the local soil class is ZD, local soil effect coefficients according to TBSC 2018 are obtained as $F_s = 1.000$ for short period and $F_1 = 1.957$ for one second period, from Table 3.5 and Table 3.6, and also from the Turkish Earthquake Hazard Map website [20].

Table 3.5. Local soil effect coefficient for short period.

Local Soil Class	Local Soil Effect Coefficient for short period, F_s					
	$S_s \le 0.25$	$S_s = 0.50$	$S_s = 0.75$	$S_s = 1.00$	$S_s = 1.25$	$S_s \ge 1.50$
ZA	0.8	0.8	0.8	0.8	0.8	0.8
ZB	0.9	0.9	0.9	0.9	0.9	0.9
ZC	1.3	1.3	1.2	1.2	1.2	1.2
ZD	1.6	1.4	1.2	1.1	1.0	1.0
ZE	2.4	1.7	1.3	1.1	0.9	0.8
ZF	Site specific soil behavior must be done.					

Table 3.6. Local soil effect coefficient for one second period.

Local Soil Class	Local Soil Effect Coefficient for one second period, F_1					
	$S_s \le 0.10$	$S_s = 0.20$	$S_s = 0.30$	$S_s = 0.40$	$S_s = 0.50$	$S_s \ge 0.60$
ZA	0.8	0.8	0.8	0.8	0.8	0.8
ZB	0.8	0.8	0.8	0.8	0.8	0.8
ZC	1.5	1.5	1.5	1.5	1.5	1.4
ZD	2.4	2.2	2.0	1.9	1.8	1.7
ZE	4.2	3.3	2.8	2.4	2.2	2.0
ZF	Site specific soil behavior must be done.					

Design spectral acceleration coefficients are presented in Table 3.7. Finally, elastic design spectrum for the DD2 earthquake level which is shown in Figure 3.13 is generated by

$$S_{ae}(T) = \left(0.4 + 0.6\frac{T}{T_A}\right) S_{DS}, \qquad (0 \le T \le T_A) \tag{3.19}$$

$$S_{ae}(T) = S_{DS}, \qquad (T_A \le T \le T_B) \tag{3.20}$$

$$S_{ae}(T) = \frac{S_{D1}}{T}, \qquad (T_B \le T \le T_L) \tag{3.21}$$

$$S_{ae}(T) = \frac{S_{D1}T_L}{T^2}, \qquad (T_L \le T) \tag{3.22}$$

where corner periods T_A, T_B and limit period for constant displacement range T_L are calculated as

$$T_A = 0.2\frac{S_{D1}}{S_{DS}}, \tag{3.23}$$

$$T_B = \frac{S_{D1}}{S_{DS}}, \tag{3.24}$$

$$T_L = 6\,s. \tag{3.25}$$

Table 3.7. Design spectral acceleration coefficients.

	S_{DS}	S_{D1}
DD2	1.271	0.671

To obtain the increased target spectrum, the values between $0.2T_p$ and $1.5T_p$ are increased by 30%,.where T_p is the first mode fundamental natural vibration period of the CSBs. For CSB I, the first mode fundamental natural period of vibration is 0.58 s, and the second mode fundamental natural period of vibration is 0.52 s. For CSB II, the first mode fundamental natural period of vibration is 1.64 s, and the second mode fundamental natural period of vibration is 1.55 s.

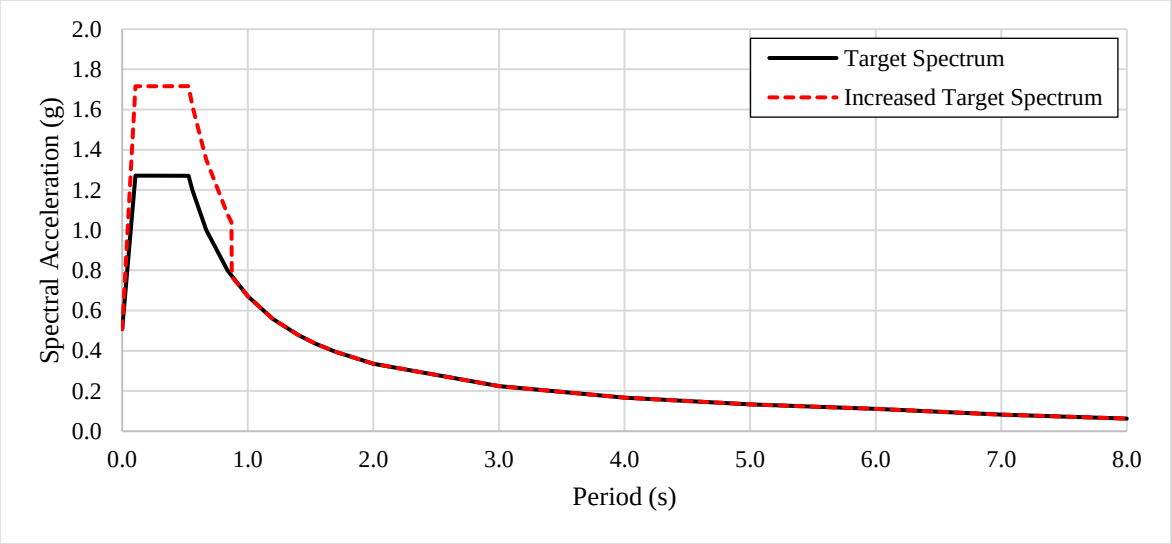

Figure 3.13. Target spectrum for DD2 ground motion level and increased target spectrum of CSB I.

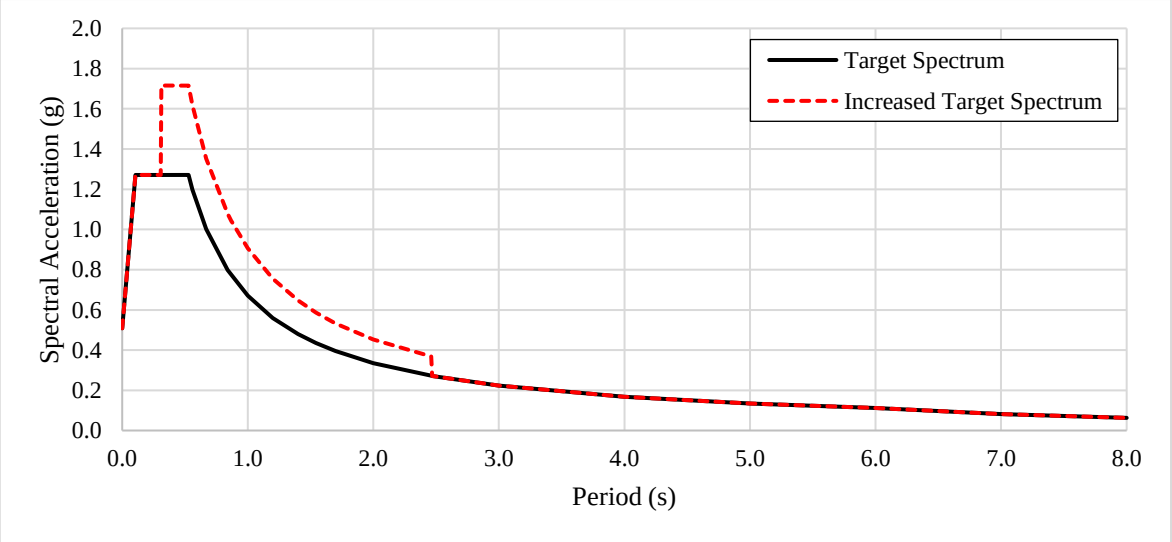

Figure 3.14. Target spectrum for DD2 ground motion level and increased target spectrum of CSB II.

According to TBSC 2018, a vertical acceleration response spectrum must also be constructed in some cases. However, if the structure does not have columns supported by beams, inclined columns, beams with spans larger than 20 m, or cantilever beams longer than 5 m, TBSC 2018 allows the vertical earthquake effect to be included only as equivalent static vertical load which is expressed as

$$E_d^{(Z)} \approx (2/3) S_{DS} G \,. \tag{3.26}$$

3.3.3.2. Earthquake Ground Motion Records. Ground motion records are selected from NGAWest2 Ground Motion Database [21]. Some of the parameters that are considered while selecting ground motion records fault mechanism, magnitude, shear wave velocity ($V_{s,30}$), closest distance from project location to projection of rupture surface (R_{JB}), etc. (Table 3.8) There are many grounds motion records that are compatible with these parameters. However, TBSC 2018 enforces that the average resultant spectrum of selected ground motions shall be greater than the increased target spectrum where the resultants are calculated using SRSS.

While selecting the most suitable set of ground motions, the mean square error (MSE) method is used. It is a method to calculate the mean error between spectral accelerations of a record and target spectrum for a specified period range ($0.2T_p$ and $1.5T_p$ in our case) and MSE is expressed as

$$MSE = \frac{1}{N}\sum_{i=1}^{N} w_i \left(S_{aeT} - S_{aeR}\right)^2 . \tag{3.27}$$

After choosing the most suitable records for the target spectrum, ground motions are linearly scaled to match the target spectrum (simple scaling method). It is enforced by TBSC 2018 that at least eleven ground motion record pairs must be selected and at most three record pairs can be selected from the same earthquake. Ultimately, the average SRSS spectrum of the selected ground motion records must not be smaller than the increased target spectrum.

Table 3.8. Input parameters of Ground Motion Database.

Fault Type	Strike-Slip (SS)
Magnitude Range	6.5 - 7.5
$V_{s,30}$ Range (m/s)	150 - 750
R_{JB} Range (km)	10 - 40

Comparison of mean acceleration spectrum that is calculated with the scaled ground motions using SRSS method and the increased target acceleration spectrum for CSB I and CSB II are presented in Figure 3.15 and Figure 3.16. Additionally, the selected ground

motions and their characteristic properties are listed in Table 3.9, where it can be seen from that for both CSBs same earthquake records with different scale factors are used.

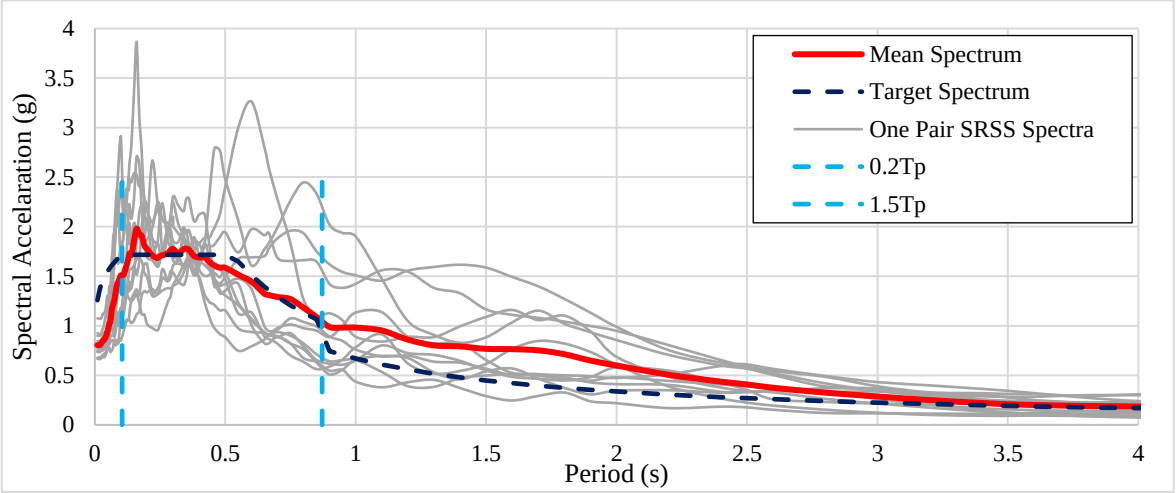

Figure 3.15. Mean and target acceleration spectra of CSB I for DD2 ground motion level.

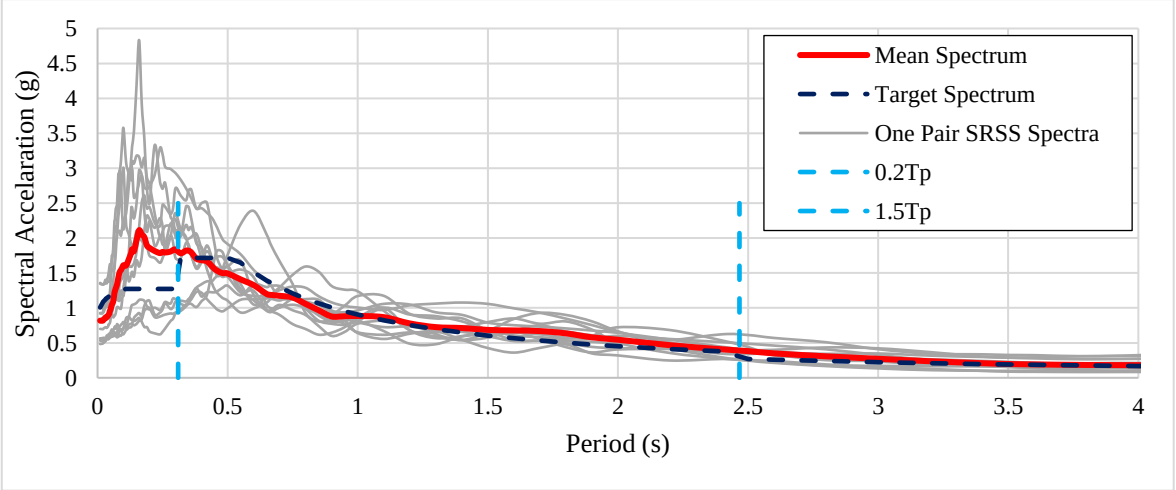

Figure 3.16. Mean and target acceleration spectra of CSB II for DD2 ground motion level.

Table 3.9. Ground motion properties for DD2 earthquake level.

Record Sequence Number	Earthquake Name	Scale Factor CSB I	Scale Factor CSB II	Magnitude	R_{JB} (km)	$V_{s,30}$ (m/s)
RSN20	Northern California	3.23	2.15	6.50	26.7	219
RSN167	Imperial Valley	3.81	5.59	6.53	13.5	260
RSN719	Superstition Hills	4.85	5.01	6.54	17.0	209
RSN720	Superstition Hills	3.30	4.13	6.54	27.0	206
RSN722	Superstition Hills	4.35	2.95	6.54	18.5	266
RSN881	Landers	2.77	2.03	7.28	17.4	396
RSN1101	Kobe	1.73	1.13	6.90	11.3	256
RSN1107	Kobe	1.81	1.99	6.90	22.5	312
RSN1115	Kobe	3.33	3.50	6.90	28.1	256
RSN1633	Manjil	1.01	1.27	7.37	12.6	724
RSN6879	Darfield	4.94	5.82	7.00	28.5	249

3.3.4. Load Combinations

In the nonlinear analysis model, dead loads, live loads, and earthquakes loads are combined as

$$G + Q_e + 0.2S + E_d^{(H)}, \tag{3.28}$$

where efficient live load is calculated as

$$Q_e = nQ, \tag{3.29}$$

where n represents live load participation factor which is specified in TBSC 2018.

3.3.5. Seismic Masses

To properly simulate the dynamic response of the structure, seismic masses are determined according to TBSC 2018. While dead loads are permanent loads that directly contribute to seismic mass, only a portion of live loads are included since the structure may not be fully loaded during a ground motion. Therefore, seismic masses are calculated as

$$m_j^{(S)} = \frac{w_j^{(S)}}{g}, \tag{3.30}$$

$$w_j^{(S)} = w_{G,j}^{(S)} + n w_{Q,j}^{(S)}, \tag{3.31}$$

where live loads are multiplied by live load participation factors. Live load reduction factors that are specified in TBSC 2018 are listed in Table 3.10.

Table 3.10. Live load participation factor.

Load Type	Live Load Participation Factor (n)
Live Load Residential	0.3
Snow Load	0.3

In order to automatically calculate the seismic masses of the case study buildings, structural models are generated in CSI ETABS software. In CSI ETABS, imposed loads and self-weights of slabs are assigned to joints as concentrated masses according to the allocated masses in the tributary areas of the joints. Then, automatically assigned joint masses by CSI ETABS are transferred to CSI Perform3D software. In the CSI Perform3D model, calculated story masses are assigned in both lateral directions at the center of mass of each story.

3.3.6. Modeling of Structural Members

To decrease the computational demand of NLTHA, only the behavioral characteristics of the members that nonlinearity is expected are involved in the nonlinear models. The two most common approaches to simulate the nonlinear behavior of structural members are the concentrated plasticity model (plastic hinge model) and the distributed plasticity model (fiber model). In the concentrated plasticity model, plastic hinges are placed in regions where nonlinearity is expected. Expected force-deformation relationships are assigned to the regions to simulate nonlinear behavior. In this study, the nonlinear flexural behavior of columns and beams is modeled using concentrated plasticity model. In the distributed plasticity approach, cross-sections of structural members are divided into small pieces called fibers. To represent the nonlinear flexural behavior of fiber sections, uniaxial stress-strain relationships of materials are assigned to each fiber section. In this study,

structural walls are modeled using distributed plasticity model where the fiber sections represent both axial and flexural behavior.

3.3.6.1 Structural Walls. Since structural walls are significant contributors to the lateral load-bearing system of a structure, realistic simulation of the nonlinear behavior of structural walls is crucial. In this study, the nonlinear behavior of structural walls is modeled using distributed plasticity model. In CSI Perform3D, two methods are available to apply distributed plasticity model, namely “Auto Section” and “Fixed Section”. Auto section method assigns concrete and steel fiber and coordinates of the tributary area automatically. However, the auto section method allows using only one type of concrete material throughout the cross-section. In this study, it is assumed that structural walls consist of confined and unconfined concrete regions (web and boundary regions). Therefore, the fixed section method which provides the ability to model confined concrete in the boundary regions and unconfined concrete in the web regions is implemented.

Performances levels of structural walls are determined according to the strain limits for concrete and reinforcement which are provided in TBSC 2018. To measure the strain values of structural walls under seismic loading, strain gage elements are placed at both ends of structural walls in nonlinear models.

3.3.6.2 Beams. Generally, nonlinearities in the flexural behavior of beam elements are concentrated at the end regions. Therefore, in this study, the nonlinear behavior of beams is modeled with concentrated plasticity model. Assumed nonlinearity zones are modeled using rotation-type moment hinges. CSI Perform3D allows users to define nonlinearity characteristics of plastic hinges with backbone curves and to reflect hysteretic strength and stiffness degradation.

In this study, the force-deformation relationship of moment hinges for beams are defined with elastic perfectly plastic backbone curves, and strength and stiffness degradation due to hysteretic behavior is omitted.

3.3.6.3 Columns. Similarly, nonlinearities in the flexural behavior of columns are concentrated at the end regions. However, unlike beams, characteristics of flexural behavior are controlled by the level of axial load carried by the cross-section.

Therefore, rotation-type PMM hinges are used to model the plastic hinges at the end regions of column elements. PMM yield surface for initiation of plastic deformation is determined according to sectional analysis results. In this study, similar to beams, the force-deformation relationship of moment hinges for columns are defined with elastic perfectly plastic backbone curves, and strength and stiffness degradation due to hysteretic behavior is omitted.

Columns and beams are modeled in CSI Perform3D as two plastic hinges placed at the end of rigid end zones and one elastic cross-section in between the two plastic hinges. Elastic section effective flexural rigidity $(EI)_e$ is calculated as

$$(EI)_e = \frac{M_y L_s}{\theta_y 3}, \tag{3.32}$$

where yield rotation, θ_y is calculated as

$$\theta_y = \frac{\phi_y L_s}{3} + 0.0015\eta\left(1+1.5\frac{h}{L_s}\right) + \frac{\phi_y d_b f_{ye}}{8\sqrt{f_{ce}}}. \tag{3.33}$$

Effective flexural rigidities of the column and beam sections are multiplied by the corresponding stiffness modifiers provided in Table 3.1.

According to TBSC 2018, for the structural elements that are modeled using the concentrated plasticity model, plastic rotation capacities for collapse prevention limit is computed as

$$\theta_p^{(CP)} = \frac{2}{3}\left[\left(\phi_u - \phi_y\right)L_p\left(1-0.5\frac{L_p}{L_s}\right) + 4.5\phi_u d_b\right], \tag{3.34}$$

and plastic rotation capacities for life safety limit is computed as

$$\theta_p^{(LS)} = 0.75\theta_p^{(CP)}, \tag{3.35}$$

and plastic rotation capacities for immediate occupancy limit is specified as

$$\theta_p^{(IO)} = 0 . \tag{3.36}$$

3.3.6.4 Slabs. Slabs are modeled elastically in nonlinear models to consider the contribution of slab elements to the whole structural system rigidity. Additionally, constraints are assigned to floor nodes at each to simulate rigid diaphragm behavior.

3.3.7. Damping

Although a significant portion of dissipated energy sources is simulated in the nonlinear models by hysteretic behavior of structural members, some energy dissipating members or mechanisms are omitted such as internal friction, structural elements, etc. For this reason, it is recommended by TBSC 2018 that 2.5% viscous damping should be assigned to the nonlinear models. In this study, 2.4% modal damping and 0.1% Rayleigh damping are assigned to the nonlinear models in CSI Perform3D.

4. SEISMIC PERFORMANCE OF THE CASE STUDY BUILDING I

4.1. General

In this section, a comparison of NLTHA results for three structural models of CSB I under DD2 level ground motion records are presented. Interstory drift ratio, beam and column plastic rotation, shear force in structural walls, concrete compressive strain, and reinforcing steel tensile strain values and limits are presented. An overview of the seismic performance metrics and corresponding limits specified in TBSC 2018 are presented in Table 4.1.

Table 4.1. Seismic performance assessment metrics and corresponding limits.

Earthquake Level	DD2 Earthquake Level
Target Performance Level	Life Safety
Analysis Method	NLTHA in 3D
Interstory Drift Ratio Limits	TBSC 2018 Equation (4.34a)
Column Plastic Rotation Limits	TBSC 2018 Equation (5.7b)
Beam Plastic Rotation Limits	TBSC 2018 Equation (5.7b)
Structural Wall Shear Checks	TBSC 2018 Equation (7.7) & TS 500 Equation (8.7)
Concrete Strain Limits	TBSC 2018 Equation (5.4a)
Reinforcement Strain Limits	TBSC 2018 Equation (5.7a)

4.2. Interstory Drift Ratios

Interstory drift ratio (IDR) values obtained from NLTHA of three structural models of CSB I at the specified three points shown in Figure 4.1 for eleven ground motions are presented in this section. TBSC 2018 states that the mean of maximum IDRs for each analysis shall be lower than the limit value which is calculated as

$$\lambda \frac{\delta_{i,\max}}{h_i} \leq 0.008\kappa . \tag{4.1}$$

IDR limit for each nonlinear model is found to be around 2%. Additionally, a maximum limit value of 3% is also set by following the same procedure specified in TBSC 2018 which is a maximum IDR limit value that is 50% higher than the mean IDR limit value is applied for tall buildings.

While Figure 4.2, Figure 4.3 and Figure 4.4 show the mean of maximum IDRs obtained under eleven pairs of DD2 level ground motions at P1, P2, and P3, respectively, Figure 4.5, Figure 4.6 and Figure 4.7 show the maximum of maximum IDRs obtained under eleven pairs of DD2 level ground motions at P1, P2, and P3, respectively

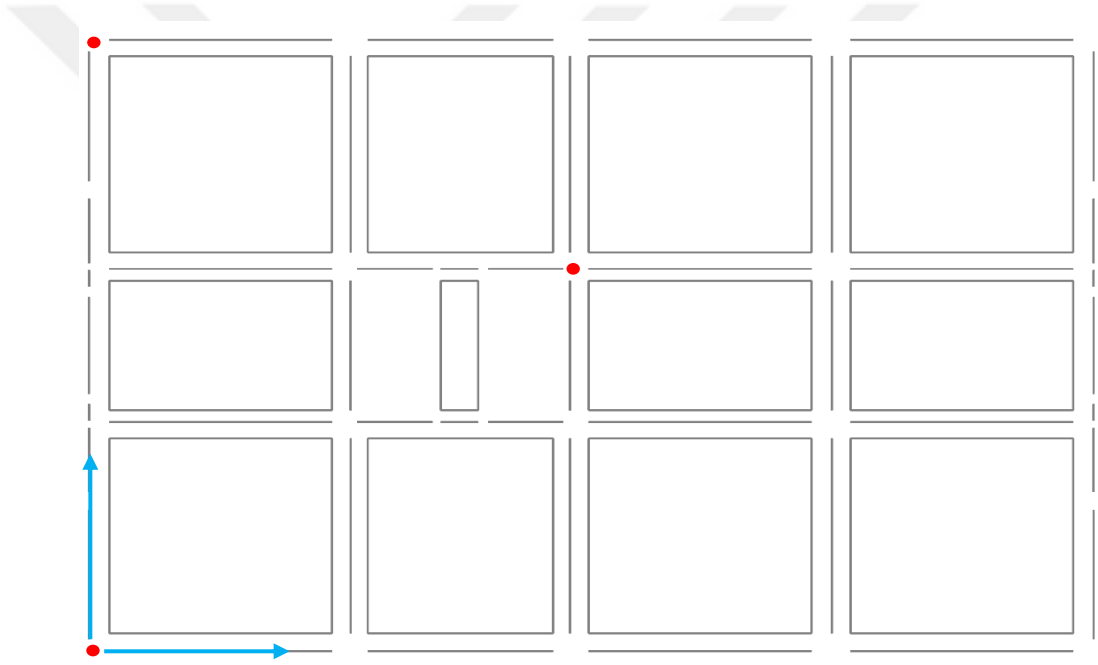

Figure 4.1. Control points of interstory drift ratios.

According to NLTHA analysis results, mean IDR values obtained from Plain RC model of CSB I were already below the mean IDR limit and retrofitting seemed to cause no significant improvement. However, when maximum IDR limits are compared both retrofitting options especially RET II successfully decreased the IDR values under the maximum IDR limits.

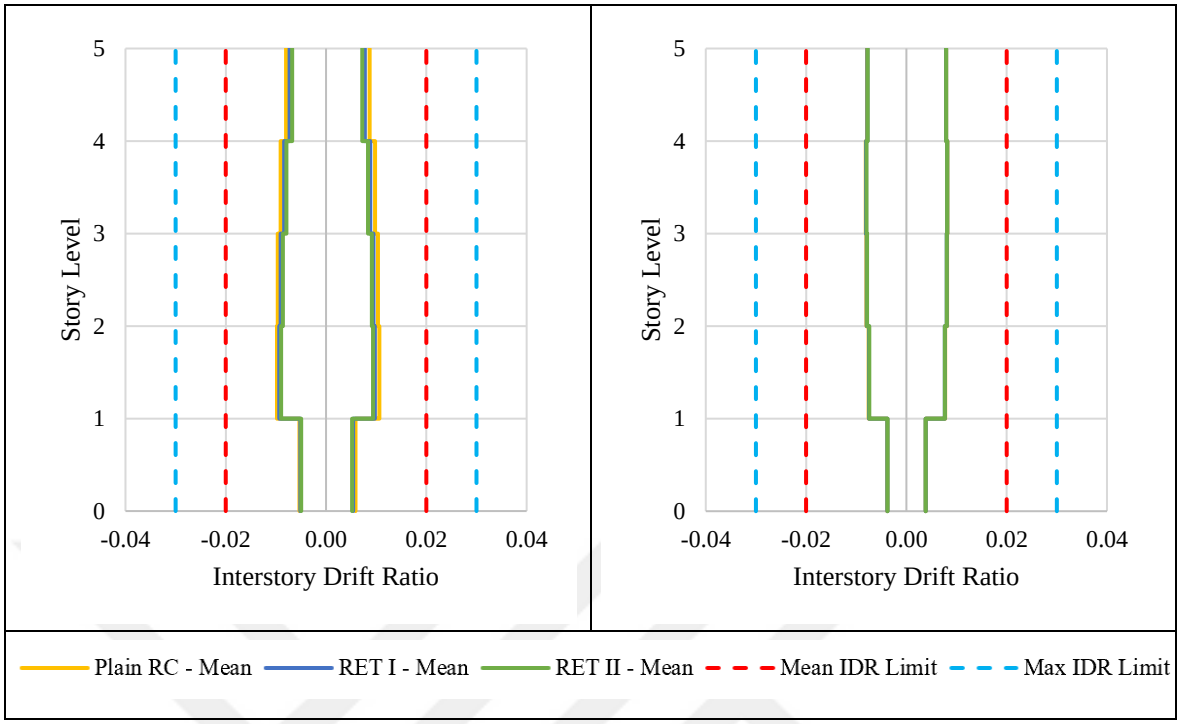

Figure 4.2. Mean interstory drift ratios of all models at P1 along x [left] and y [right].

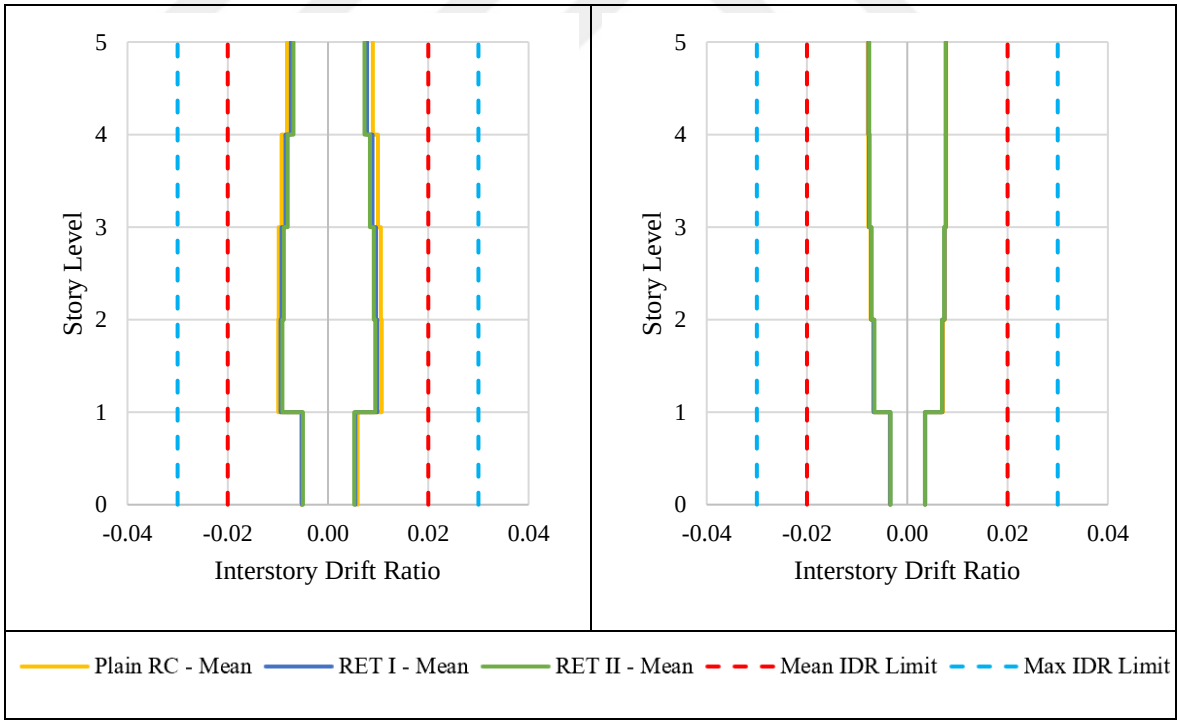

Figure 4.3. Mean interstory drift ratios of all models at P2 along x [left] and y [right].

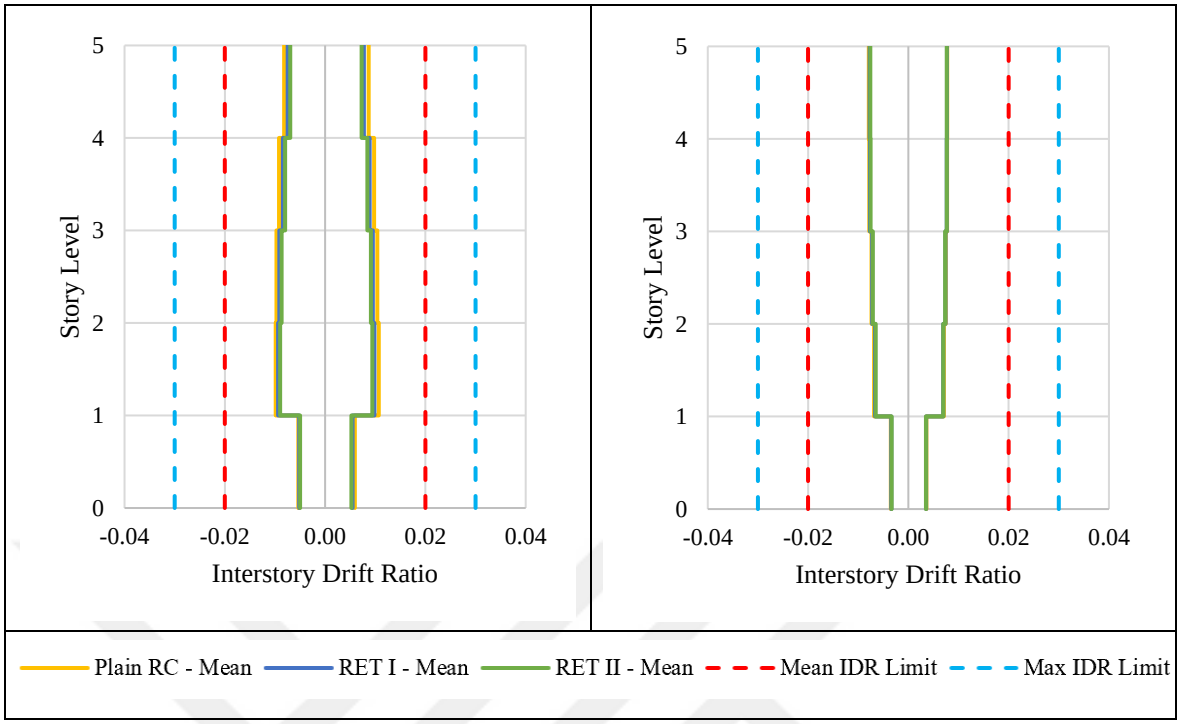

Figure 4.4. Mean interstory drift ratios of all models at P3 along x [left] and y [right].

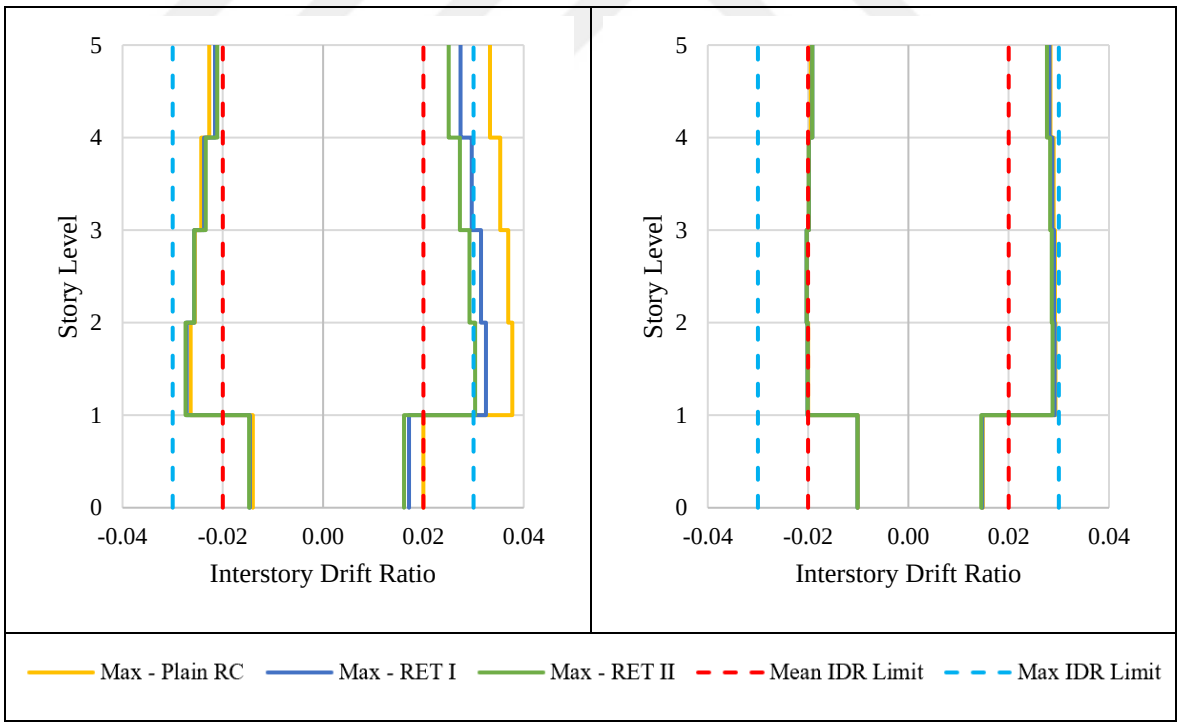

Figure 4.5. Maximum interstory drift ratios of all models at P1 along x [left] and y [right].

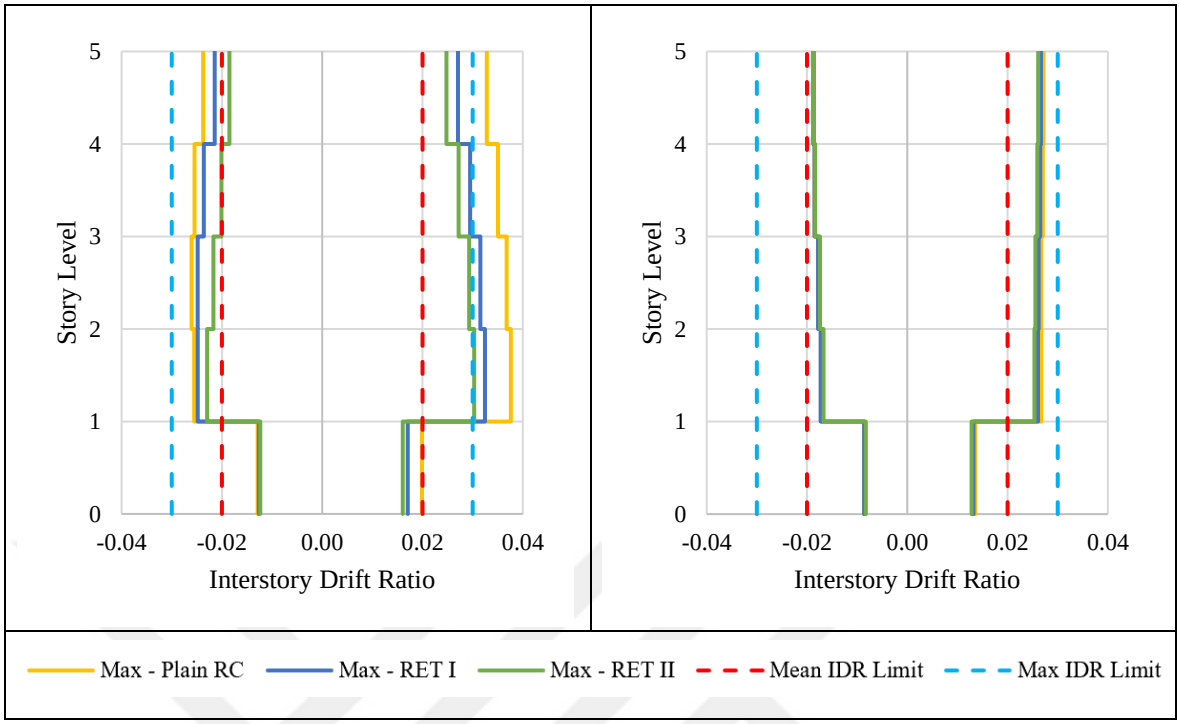

Figure 4.6. Maximum interstory drift ratios of all models at P2 along x [left] and y [right].

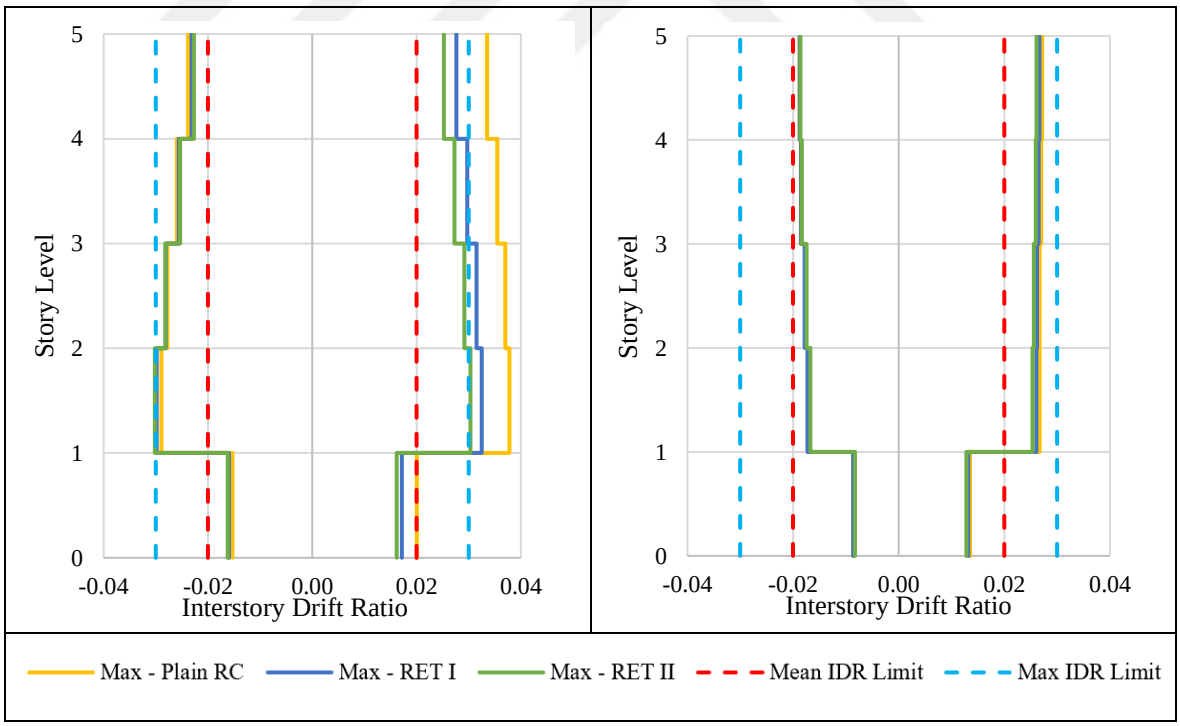

Figure 4.7. Maximum interstory drift ratios of all models at P3 along x [left] and y [right].

4.3. Column and Beam Plastic Rotations

The mean of maximum plastic rotations at both ends of all beam and column elements under eleven pairs of DD2 level ground motions are compared with their capacities for three structural models of CSB I (and). Limit plastic rotation values are calculated according to TBSC 2018. Damage regions specified in TBSC 2018 are presented in Figure 4.8. Number of beam elements in different damage zones under positive and negative bending conditions are presented in Table 4.2 and Table 4.3, respectively. The number of column elements in different damage zones are presented in Table 4.4.

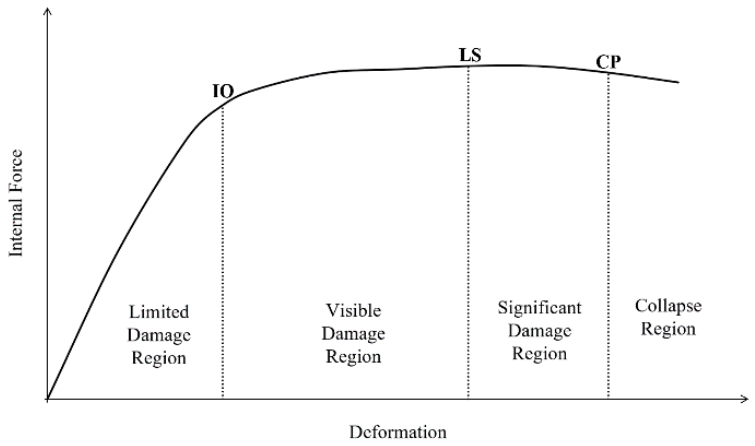

Figure 4.8. Damage regions and performance limits.

Table 4.2. Number of beam elements in different damage regions for positive bending.

Beam+	Limited Damage Region	Visible Damage Region	Significant Damage Region	Collapse Region
Plain RC	0	121	17	7
RET I	0	124	15	6
RET II	0	125	14	6

Table 4.3. Number of beam elements in different damage regions for negative bending.

Beam-	Limited Damage Region	Visible Damage Region	Significant Damage Region	Collapse Region
Plain RC	0	120	21	4
RET I	0	131	10	4
RET II	0	132	9	4

Table 4.4. Number of column elements in different damage regions.

Column	Limited Damage Region	Visible Damage Region	Significant Damage Region	Collapse Region
Plain RC	5	55	0	0
RET I	3	57	0	0
RET II	2	58	0	0

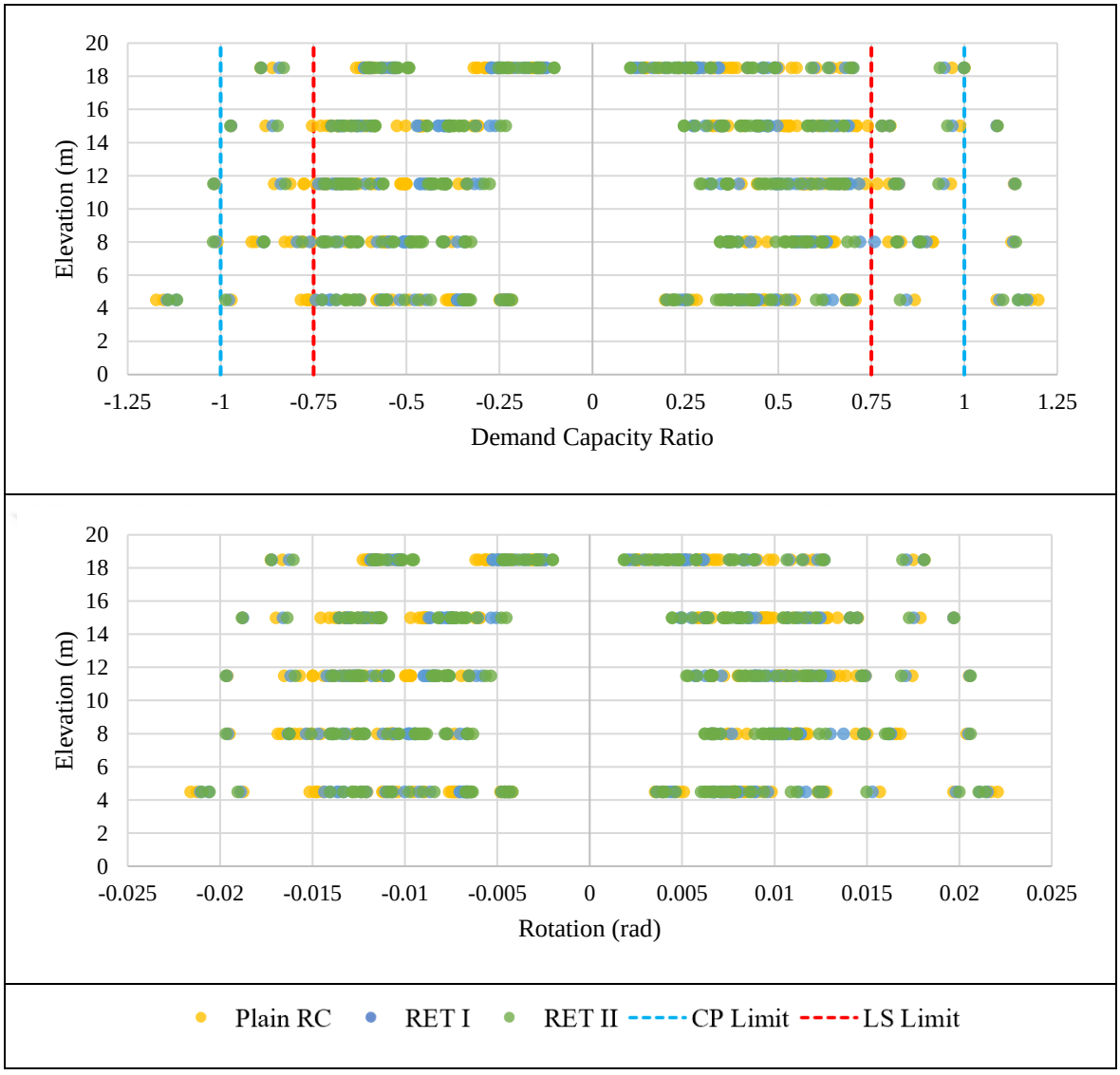

Figure 4.9. Demand - capacity ratios [top] and plastic rotations [bottom] of beams.

It can be clearly seen from tables and figures that none of the retrofitting options result in a significant improvement on seismic performance in terms of plastic hinge rotations of the frame elements for CSB I.

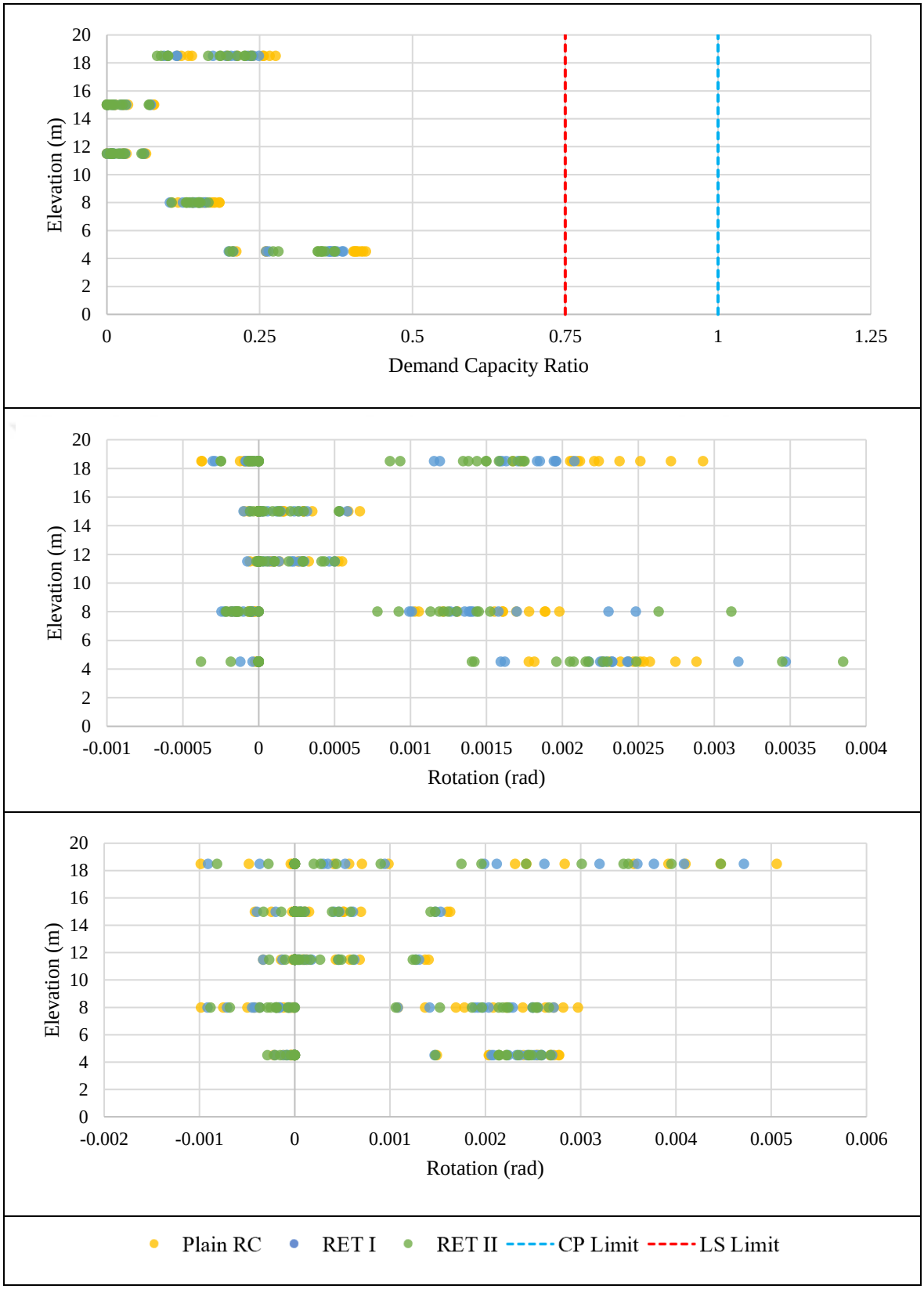

Figure 4.10. Demand - capacity ratios [top] and plastic rotations of columns, in the x-direction [middle] and in the y-direction [bottom].

4.4. Structural Wall Shear Force

In this section, the shear force demands of the structural walls of CSB I identified in Figure 4.11 are compared with allowable shear capacities. Shear force demands are calculated based on the mean plus one standard deviation of maximum absolute values obtained from analysis results of eleven pairs of ground motions for each structural model. Shear capacities of structural walls are calculated as

$$V \leq 0.85 A_{ch} \sqrt{f_c} \ . \tag{4.2}$$

Additionally, since TS 500 specifications tend to give more conservative shear capacity values for poor concrete quality and CSB I is assumed to have relatively low characteristic concrete compressive strength (10 MPa), capacity values specified in TS 500 which are calculated as

$$V \leq 0.22 A_{ch} f_c \ , \tag{4.3}$$

are also included. The shear force demand and capacity for each structural wall of each structural model are shown in Figure 4.12, Figure 4.13 and Figure 4.14. Additionally, story shear values are provided in Figure 4.15.

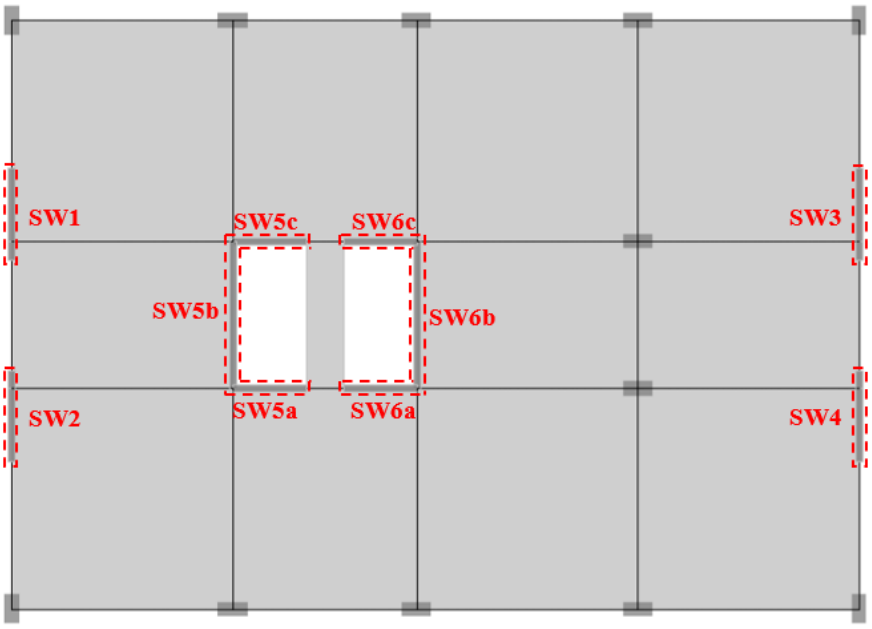

Figure 4.11. Structural wall labels and their locations.

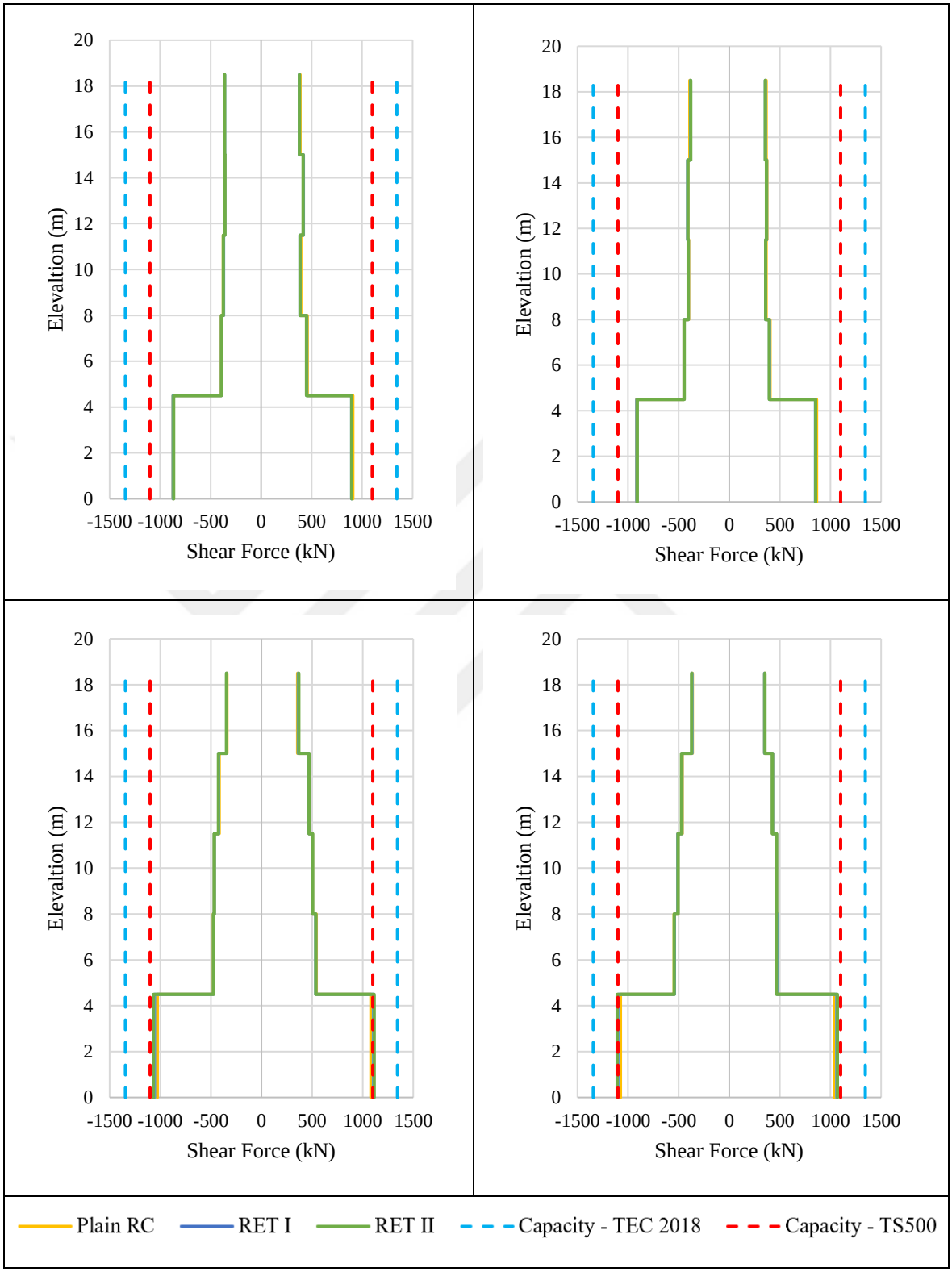

Figure 4.12. Structural wall shear forces: SW1 and SW2 [top], SW3 and SW4 [bottom].

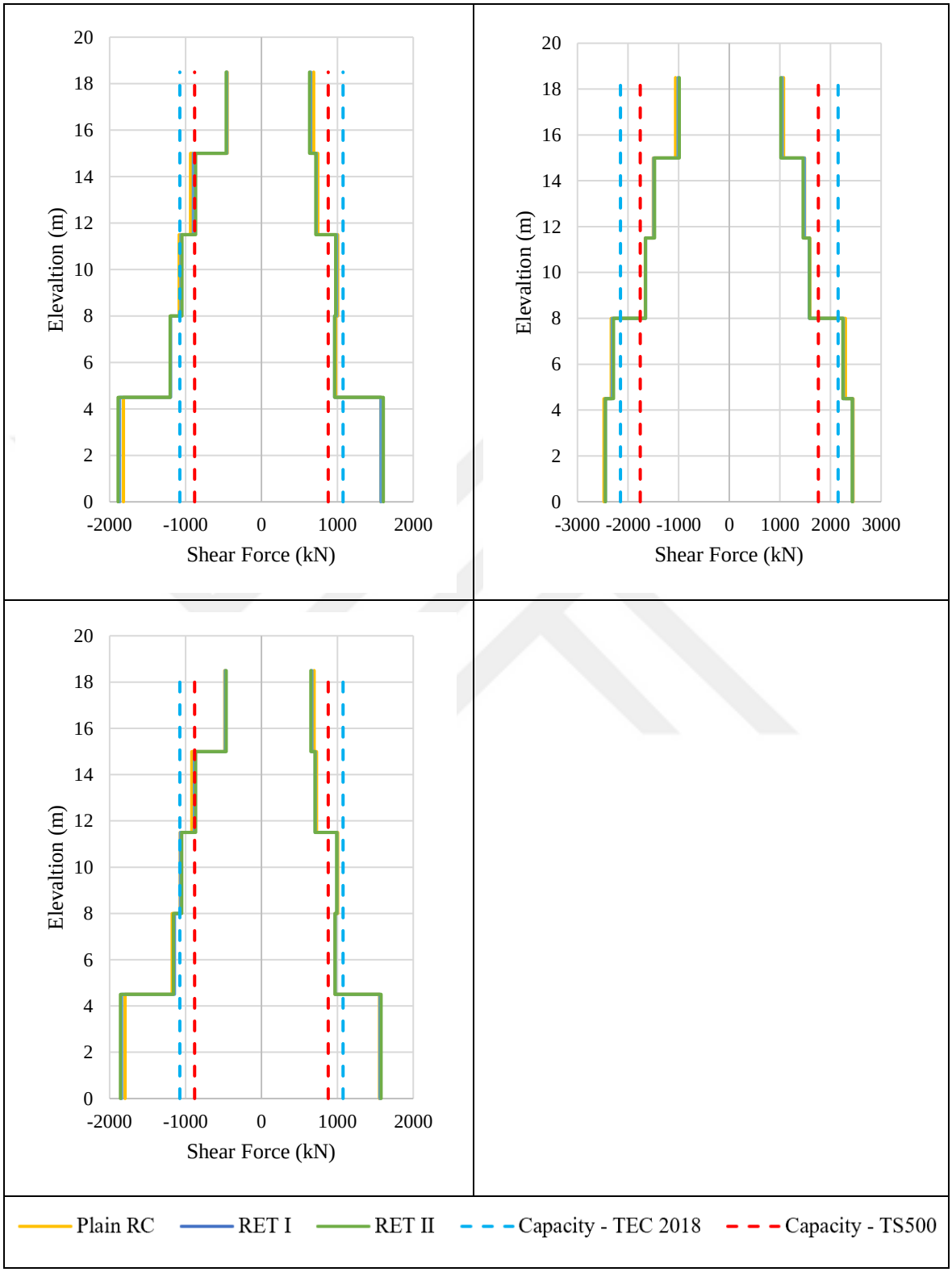

Figure 4.13. Structural wall shear forces: SW5a and SW5b [top], SW5c [bottom].

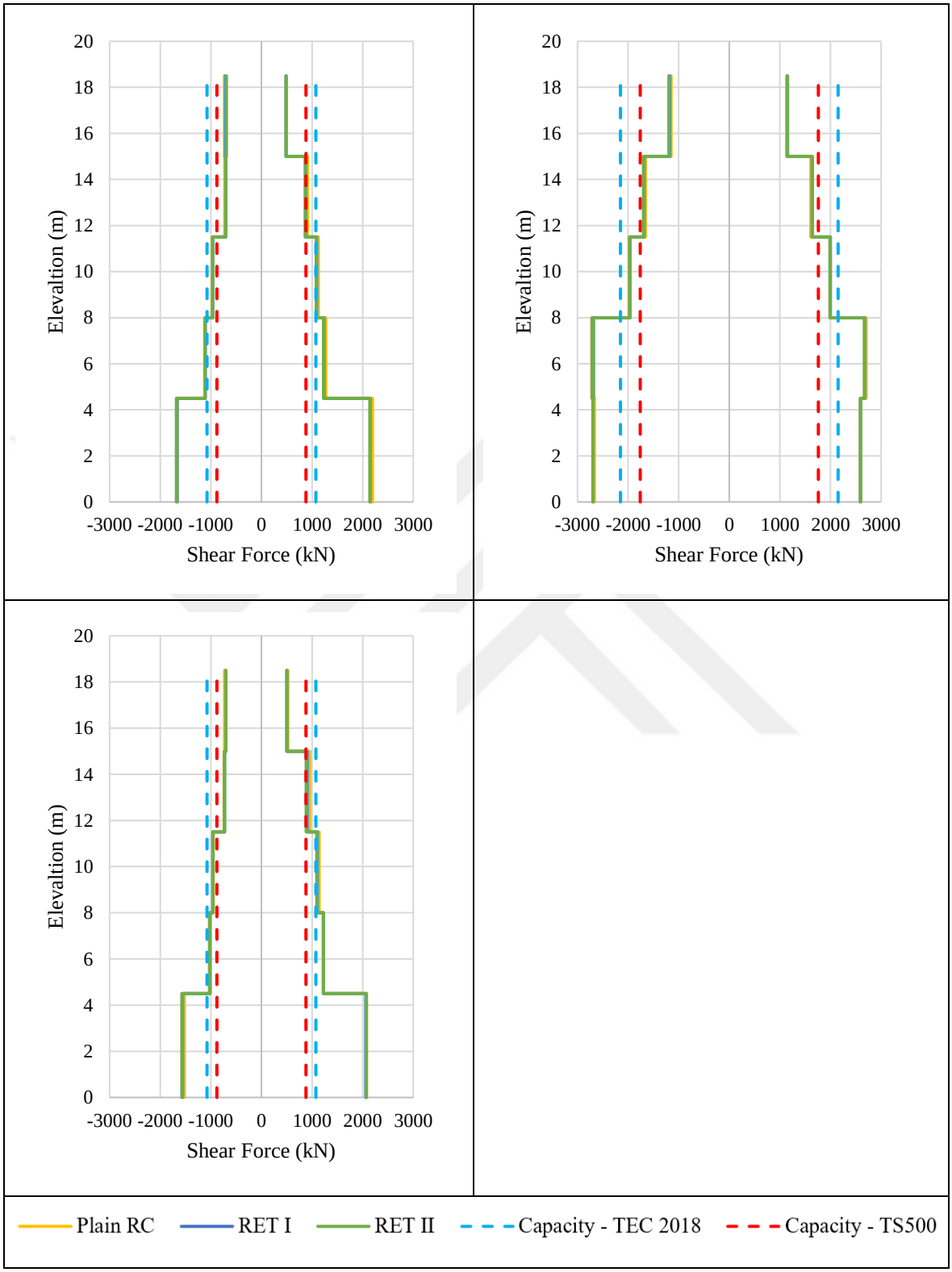

Figure 4.14. Structural wall shear forces: SW6a and SW6b [top], SW6c [bottom].

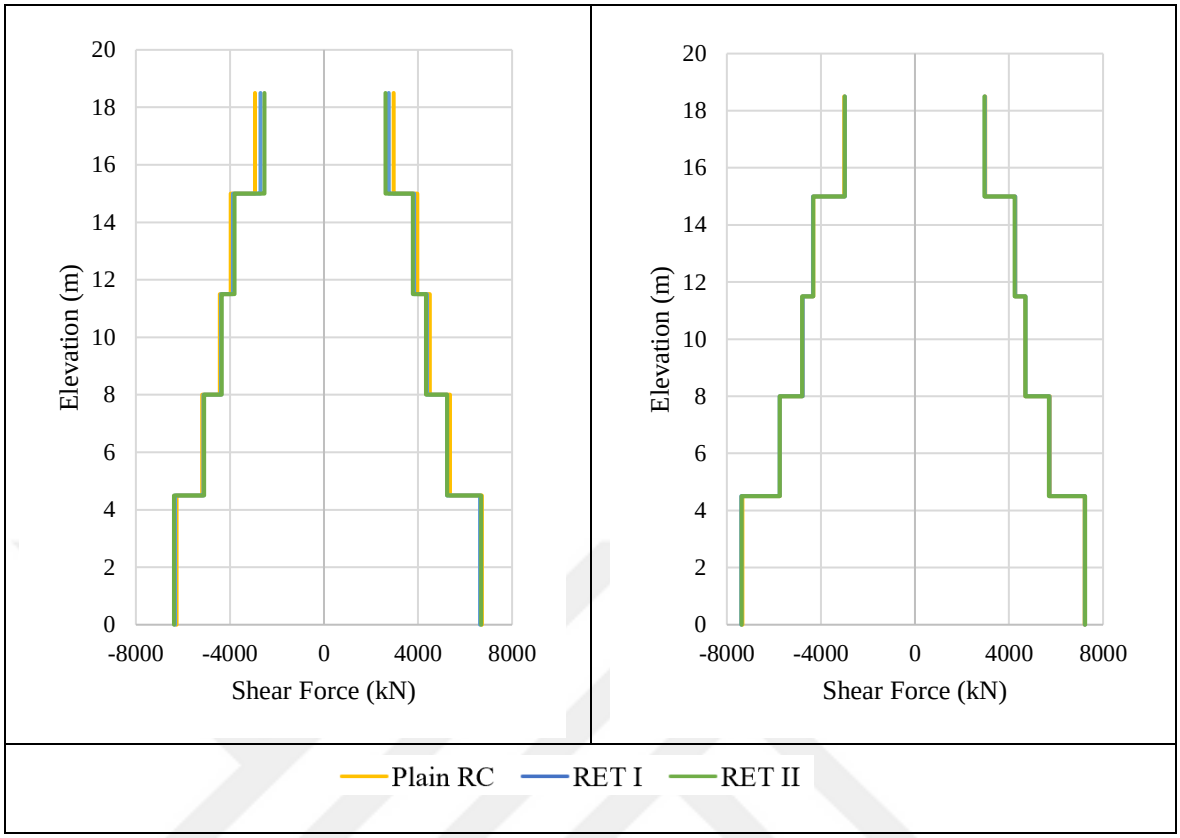

Figure 4.15. Story shear forces in x and y directions.

NLTHA results show that for the Plain RC model of CSB I, while rectangular walls have adequate shear capacity, core walls have insufficient shear capacity. Additionally, neither RET I nor RET II provides any noticeable reduction in shear demands of structural walls.

4.5. Strain Values of Structural Walls

Strain gages are implemented to the wall ends to measure strain. The strain gage locations on the building plan are provided in Figure 4.16. The mean of maximum strain values from the eleven pairs of ground motions for each structural model are compared.

The inelastic longitudinal concrete compressive strain (negative) demands and reinforcing steel tensile strain (positive) demands along with only IO strain limits at both ends of each structural wall for eleven pairs of ground motions for each structural model are presented in Figure 4.17, Figure 4.18, Figure 4.19 and Figure 4.20. Since strain demands are so small that they do not reach LS and CP strain limits, only IO strain limits are shown in

these figures. Corresponding strain limits for each seismic performance level are calculated according to TBSC 2018 and provided in Table 4.5.

According to the results, most of the strain values obtained from Plain RC model structural walls are already below the IO performance limit but with retrofitted structural models (RET I and RET II), all structural walls satisfy IO performance level.

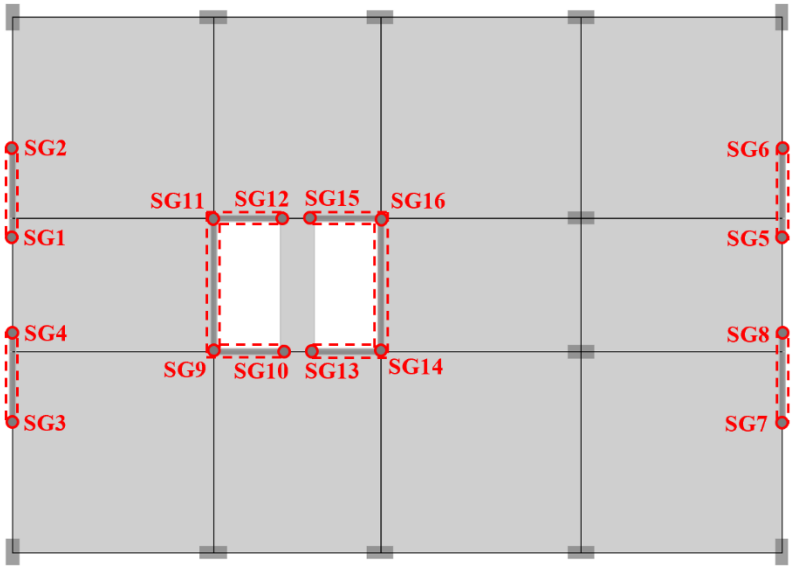

Figure 4.16. Strain measurement locations on floor plan.

Table 4.5. Performance limits for tension and compression strains on walls.

Performance Criteria	Compression	Tension
IO	-0.00250	0.00750
LS	-0.00975	0.03600
CP	-0.01300	0.04800

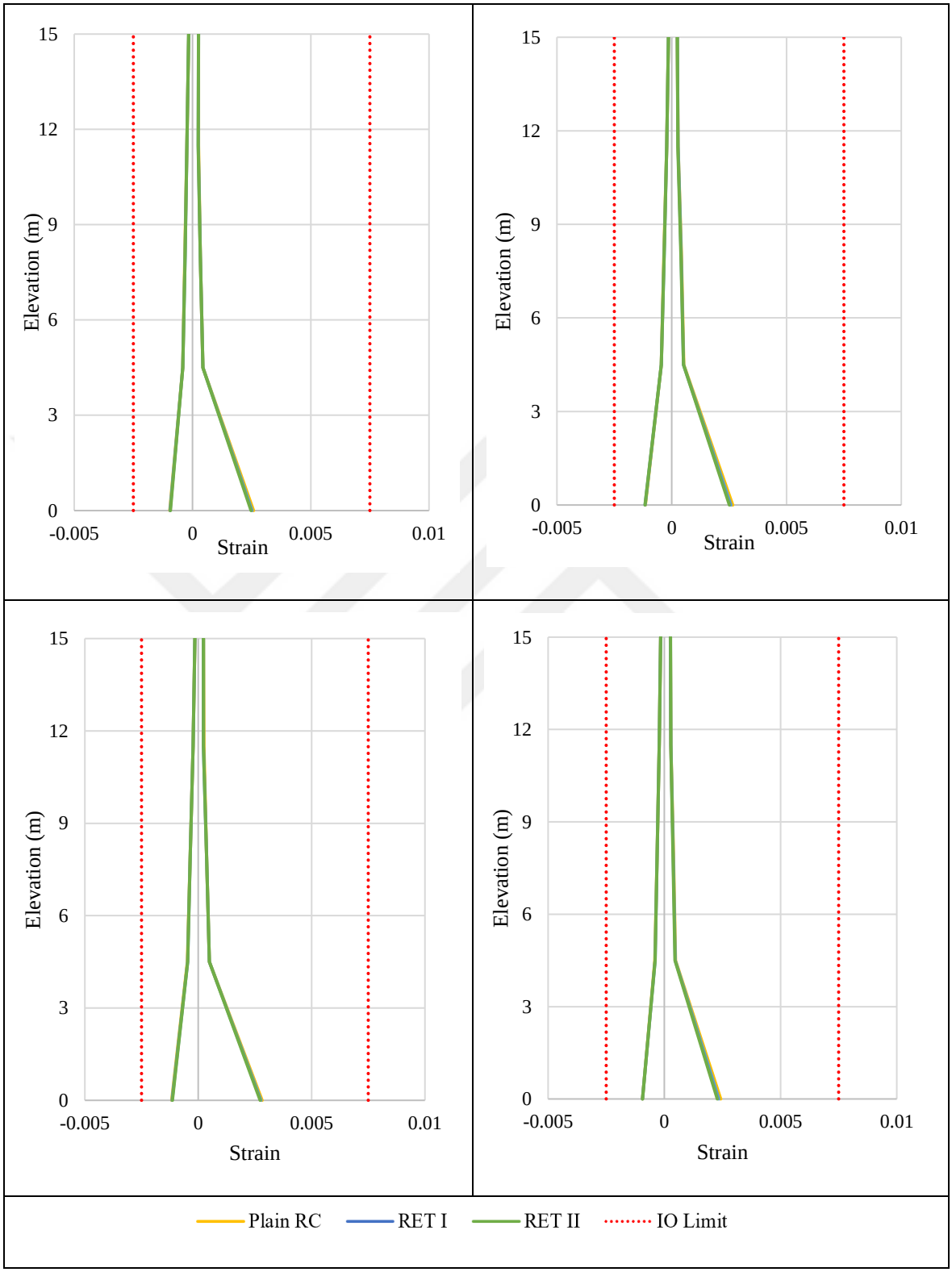

Figure 4.17. Structural wall strains: SG1 and SG2 [top], SG3 and SG4 [bottom].

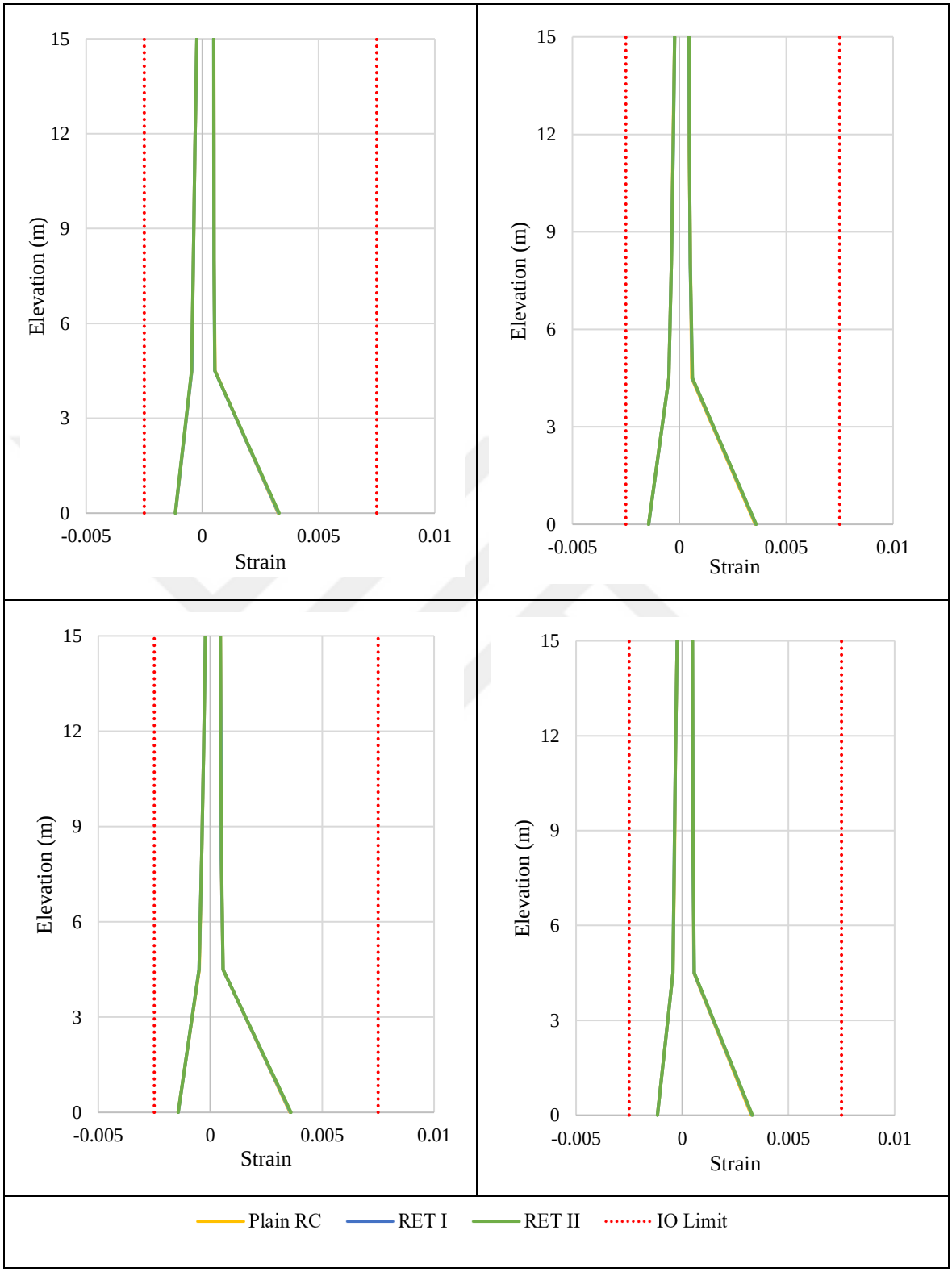

Figure 4.18. Structural wall strains: SG5 and SG6 [top], SG7 and SG8 [bottom].

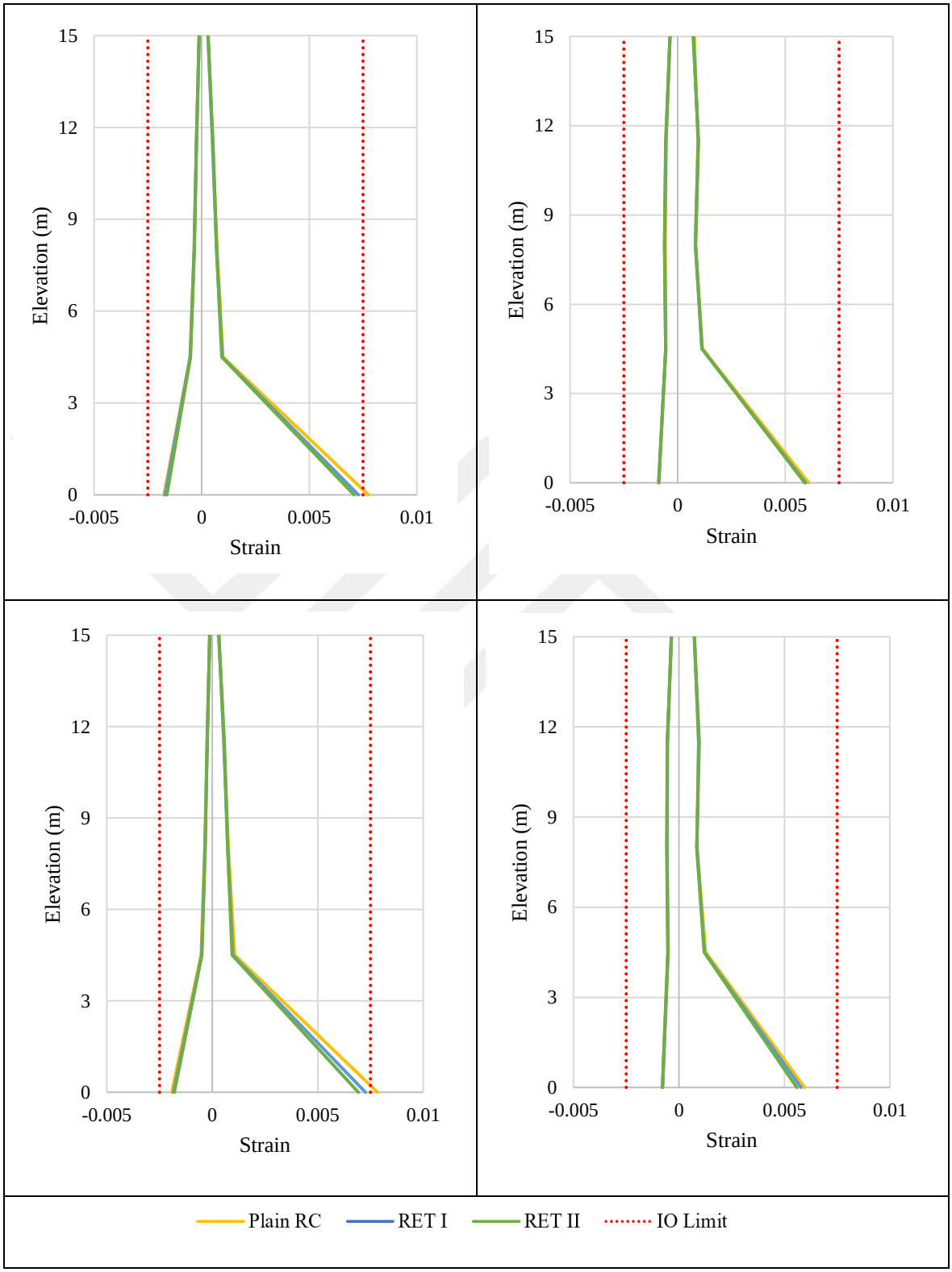

Figure 4.19. Structural wall strains: SG9 and SG10 [top], SG11 and SG12 [bottom].

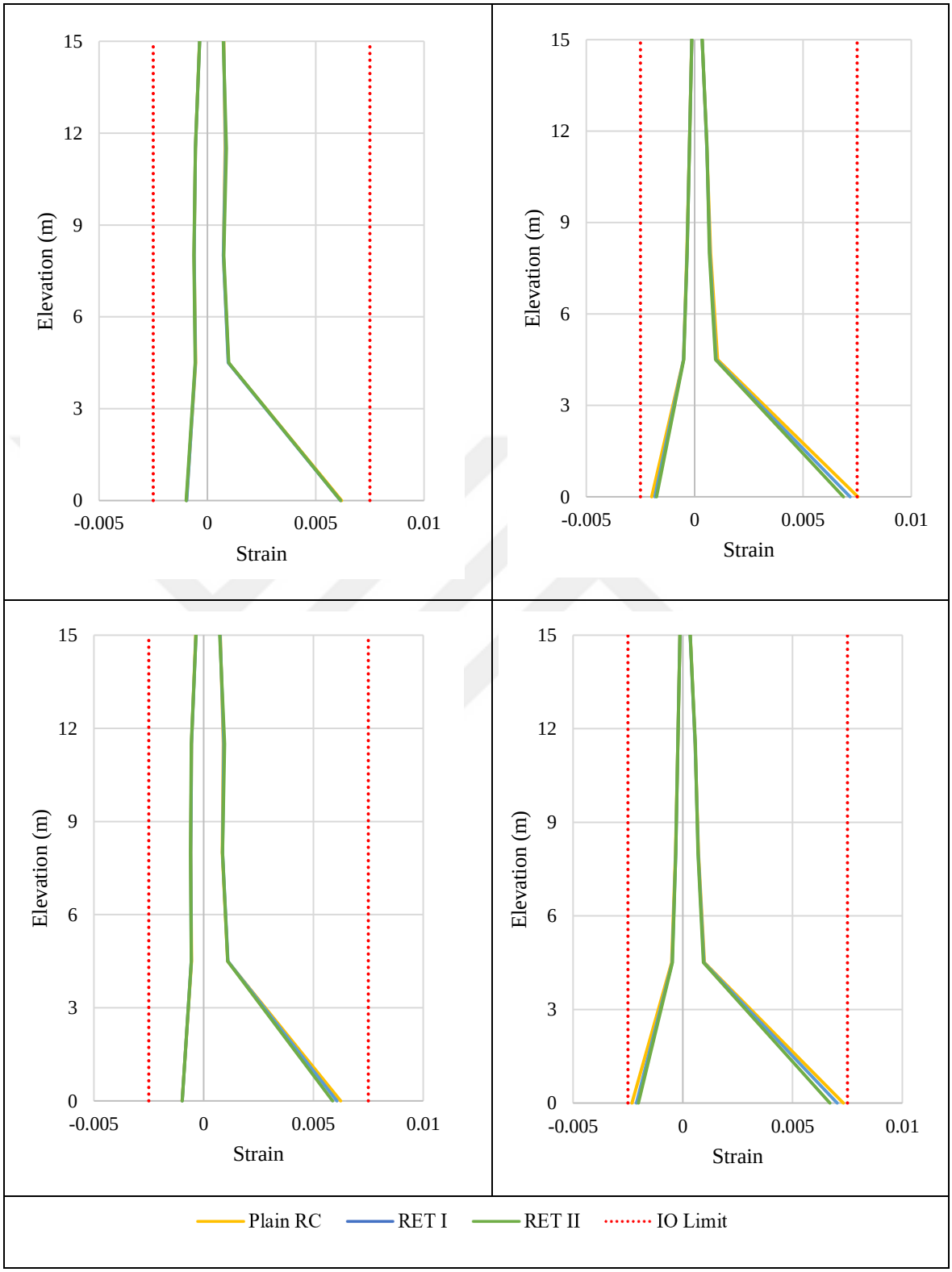

Figure 4.20. Structural wall strains: SG13 and SG14 [top], SG15 and SG16 [bottom].

5. SEISMIC PERFORMANCE OF THE CASE STUDY BUILDING II

5.1. General

In this section, a comparison of NLTHA results for three structural models of CSB II under DD2 level ground motion records are presented. Interstory drift ratio, and beam and column plastic rotation values are compared with corresponding limits in order to assess the effectiveness of retrofitting of CSB II with the two types of NTWs. An overview of the seismic performance metrics and corresponding limits specified in TBSC 2018 are presented in Table 5.1.

Table 5.1. Seismic performance assessment metrics and corresponding limits.

Earthquake Level	DD2 Earthquake Level
Target Performance Level	Life Safety
Analysis Method	NLTHA in 3D
Interstory Drift Ratio Limits	TBSC 2018 Equation 4.34a
Column Plastic Rotation Limits	TBSC 2018 Equation 5.7b
Beam Plastic Rotation Limits	TBSC 2018 Equation 5.7b

5.2. Interstory Drift Ratios

Interstory drift ratio (IDR) values at the specified three points shown in Figure 5.1 for eleven ground motions are presented in this section. TBSC 2018 states that the mean of max IDRs for each analysis shall be lower than the limit value calculated by Equation (4.1). IDR limit calculated for each nonlinear model is also 2% for CSB II. Similarly, a maximum limit value of 3% is also set for CSB II.

Figure 5.2, Figure 5.3 and Figure 5.4 shows the mean IDRs obtained under eleven pairs of DD2 level ground motions at P1, P2, and P3, respectively; Figure 5.5, Figure 5.6 and Figure 5.7 show the maximum IDRs obtained under the same eleven pairs of earthquakes.

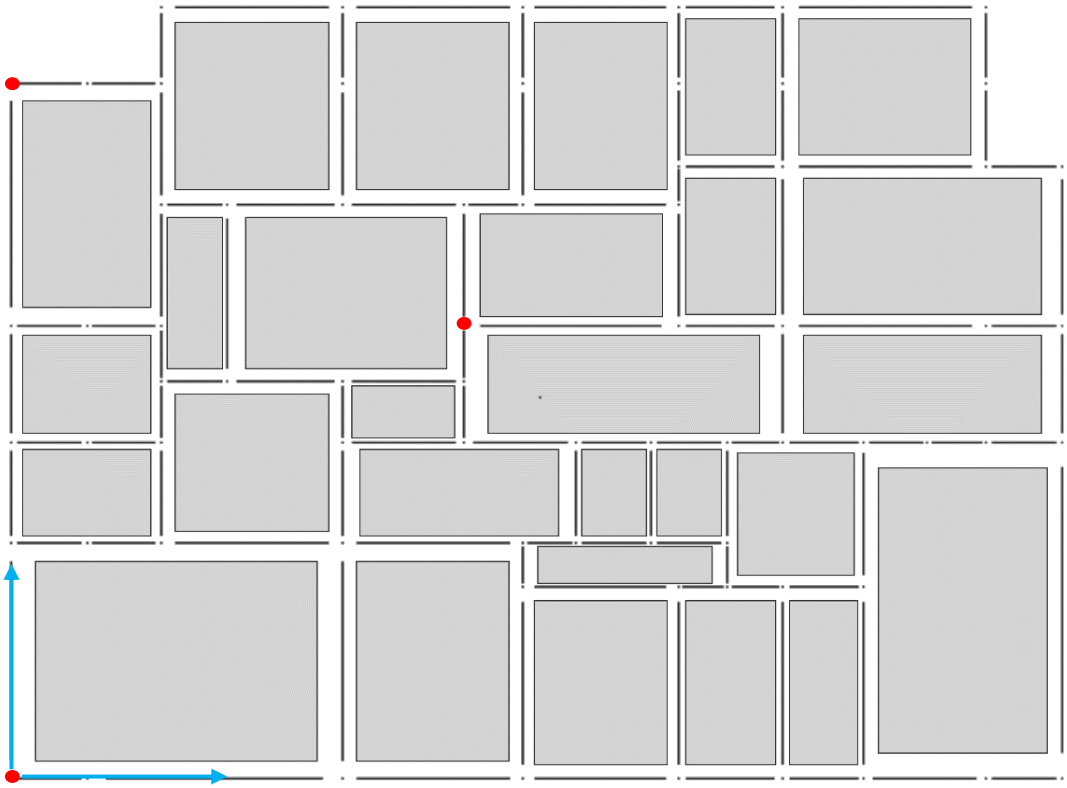

Figure 5.1. Control points of interstory drift ratios.

According to analysis results, retrofitting of CSB II with NTWs resulted in significant reductions in IDR values such that in both retrofitting scenarios mean IDR values are between mean IDR limits. However, when compared to NTW I, NTW II did not cause any noticeable improvement in reduction of IDR values even though it has much higher stiffness and strength values.

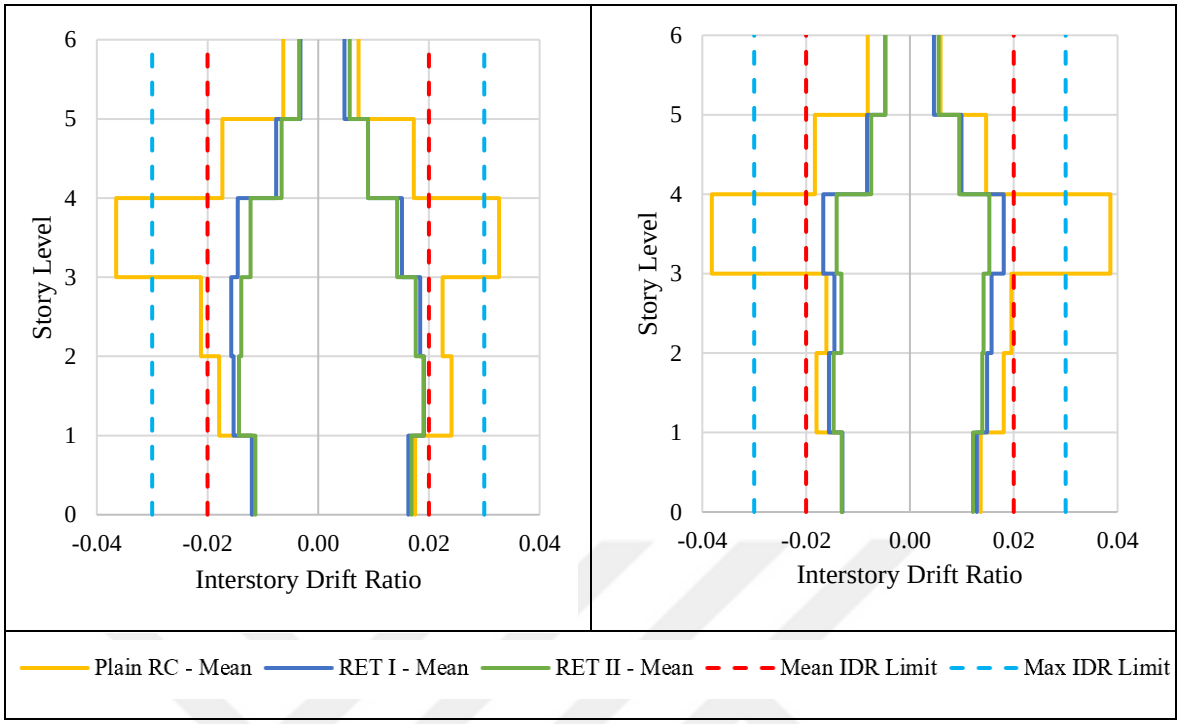

Figure 5.2. Mean interstory drift ratios of all models at P1 along x [left] and y [right].

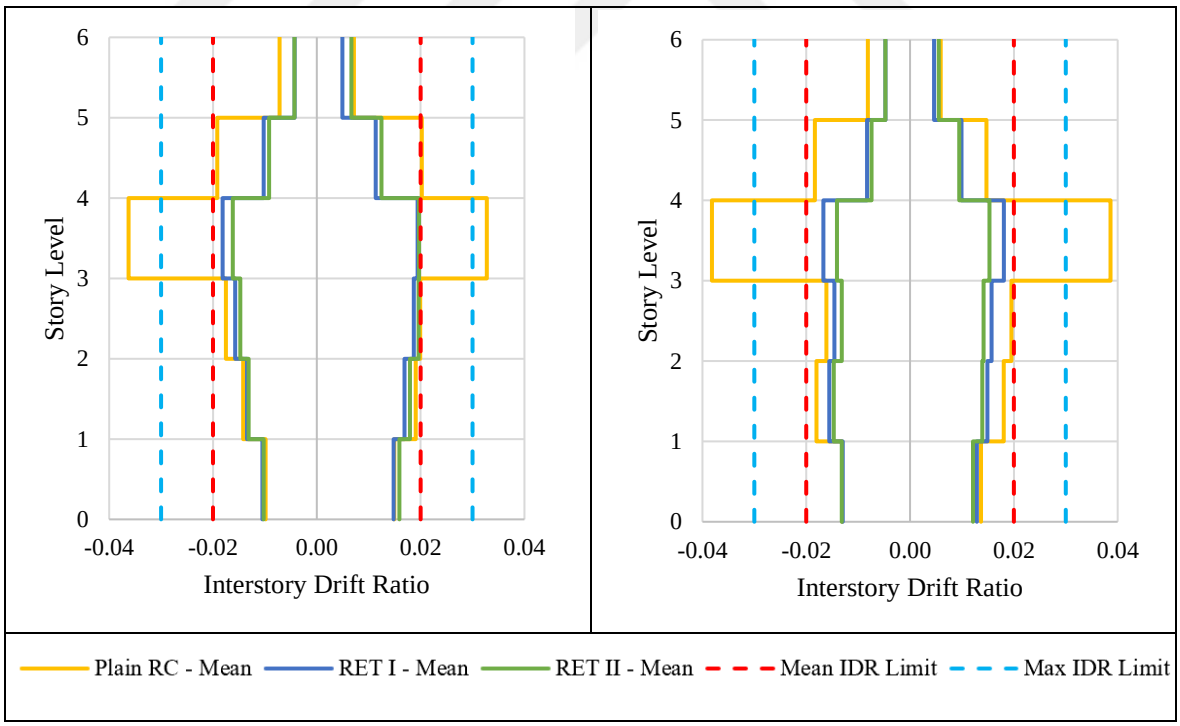

Figure 5.3. Mean interstory drift ratios of all models at P2 along x [left] and y [right].

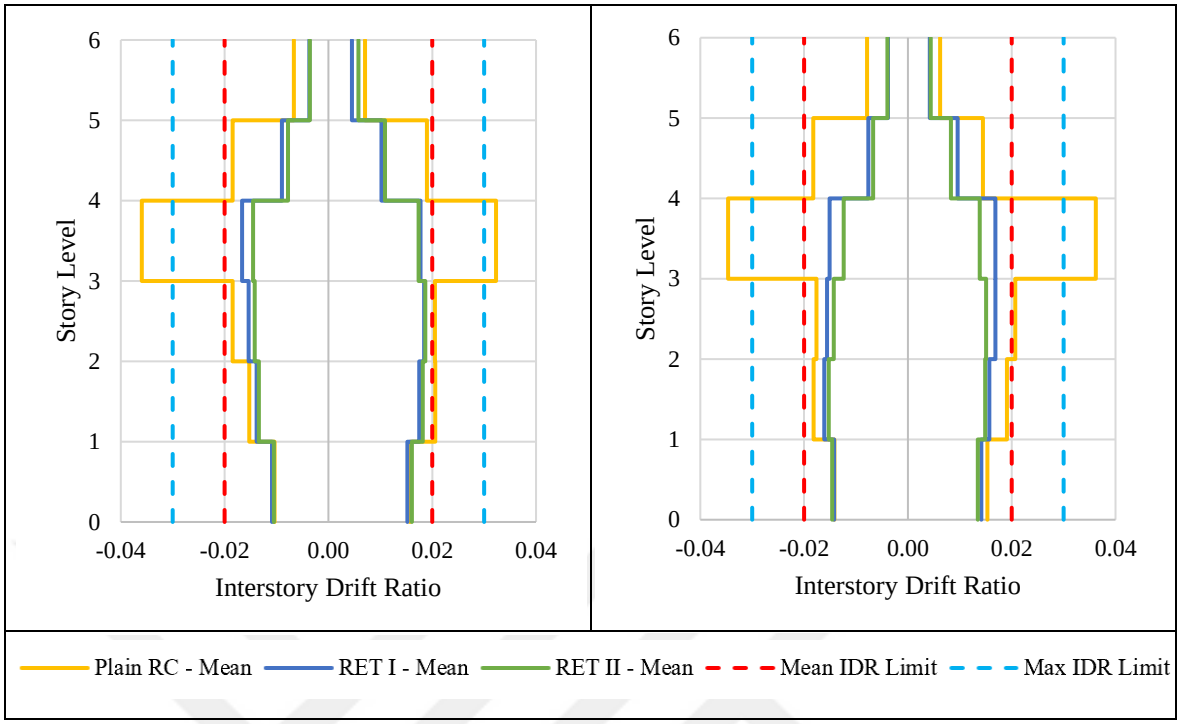

Figure 5.4. Mean interstory drift ratios of all models at P3 along x [left] and y [right].

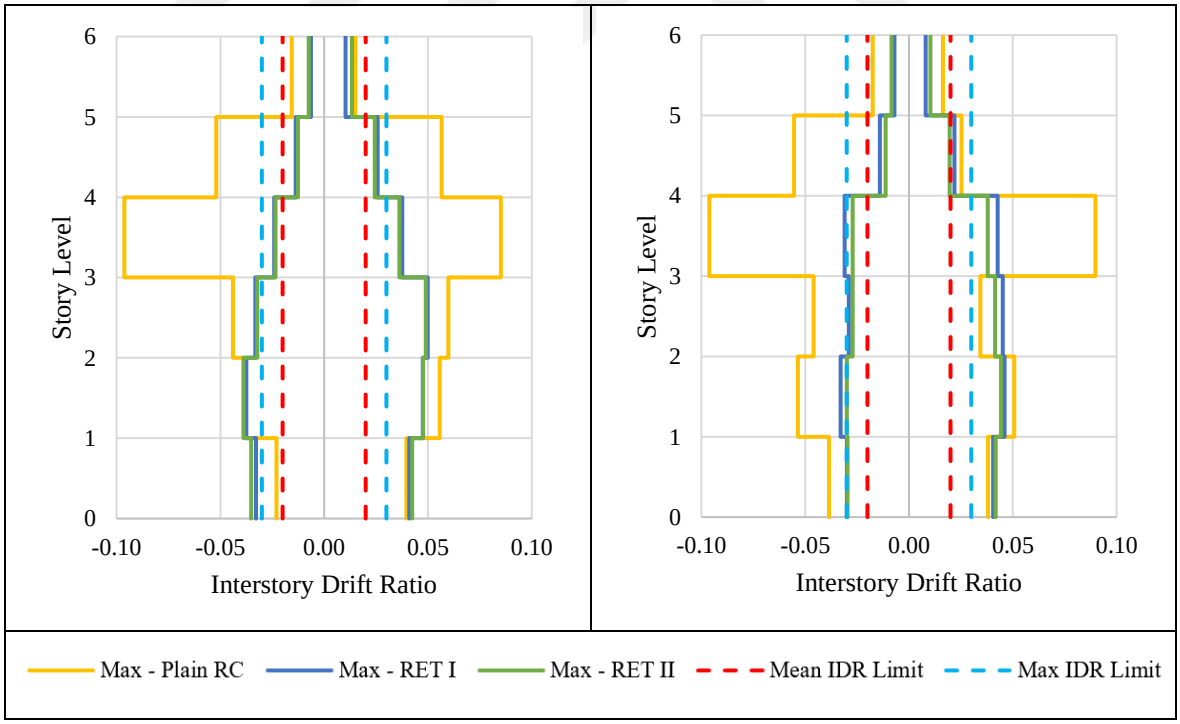

Figure 5.5. Maximum interstory drift ratios of all models at P1 along x [left] and y [right].

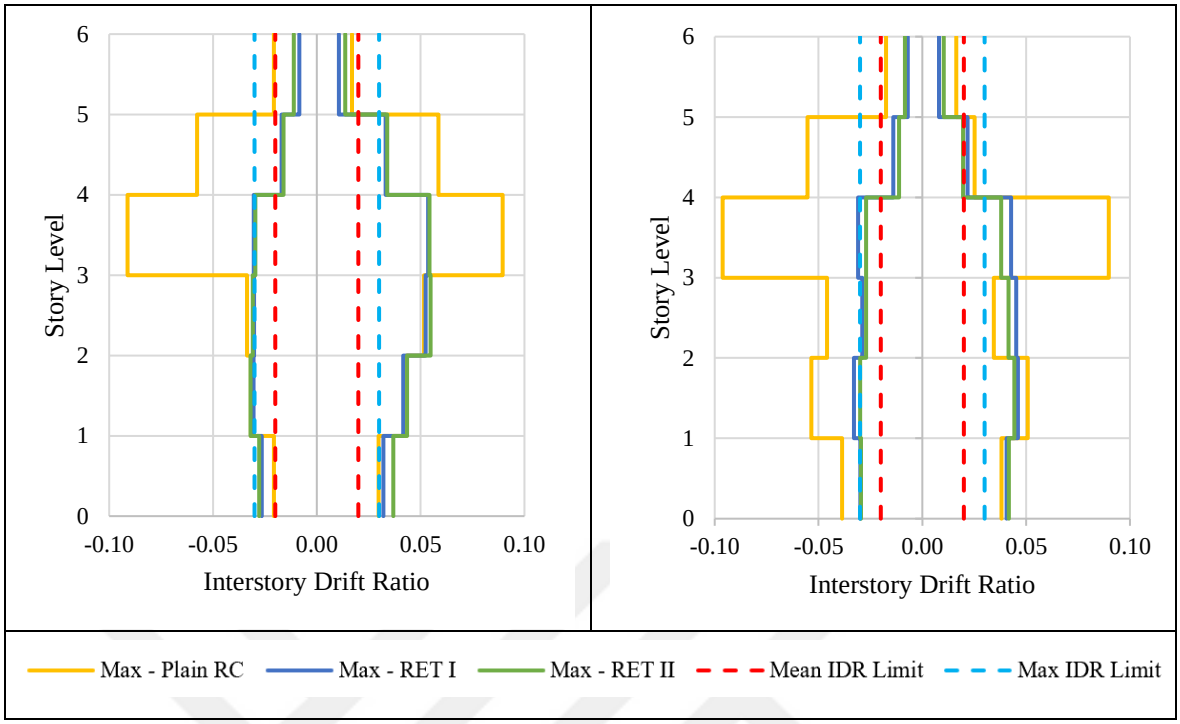

Figure 5.6. Maximum interstory drift ratios of all models at P2 along x [left] and y [right].

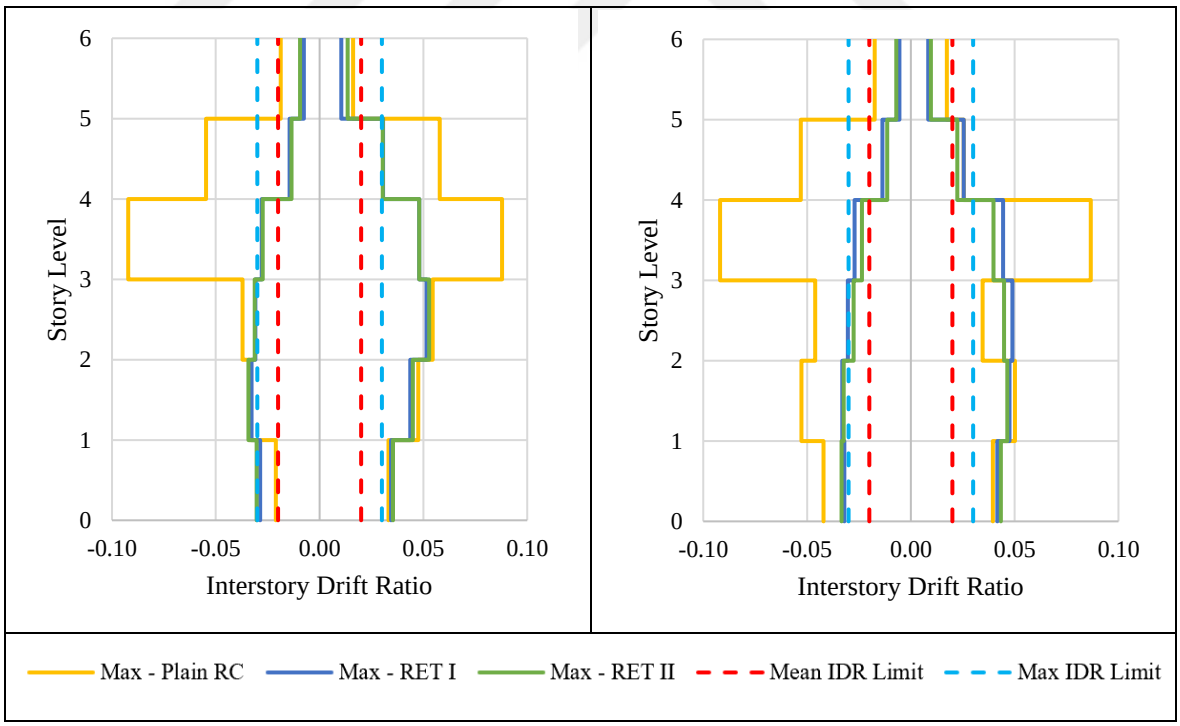

Figure 5.7. Maximum interstory drift ratios of all models at P3 along x [left] and y [right].

5.3. Column and Beam Plastic Rotations

The mean of maximum plastic rotations at both ends of all beam and column elements under eleven pairs of DD2 level ground motions are compared with their capacities for three structural models of CSB II in Figure 5.8 and Figure 5.9, respectively. The numbers of beam elements in different damage zones are provided for positive and negative bending in Table 5.2 and Table 5.3, whereas the numbers of column elements in different damage zones are presented in Table 5.4.

Table 5.2. Number of beam elements in different damage regions for positive bending.

Beam+	Limited Damage Region	Visible Damage Region	Significant Damage Region	Collapse Region
Plain RC	464	94	0	0
RET I	429	129	0	0
RET II	421	137	0	0

Table 5.3. Number of beam elements in different damage regions for negative bending.

Beam-	Limited Damage Region	Visible Damage Region	Significant Damage Region	Collapse Region
Plain RC	306	207	12	33
RET I	280	237	12	29
RET II	271	250	10	27

CSB II suffers from strong beam weak column condition and especially columns suffer from excessive plastic hinge rotations as it can be seen from Table 5.4 and Figure 5.9. Even though with the presented retrofitting methods plastic hinge rotation values of the columns are reduced significantly, neither retrofitting with NTW I nor retrofitting with NTW II manages to effectively reduce the plastic rotations of columns.

Table 5.4. Number of column elements in different damage regions.

Column	Limited Damage Region	Visible Damage Region	Significant Damage Region	Collapse Region
Plain RC	0	0	0	204
RET I	0	0	9	195
RET II	0	0	1	203

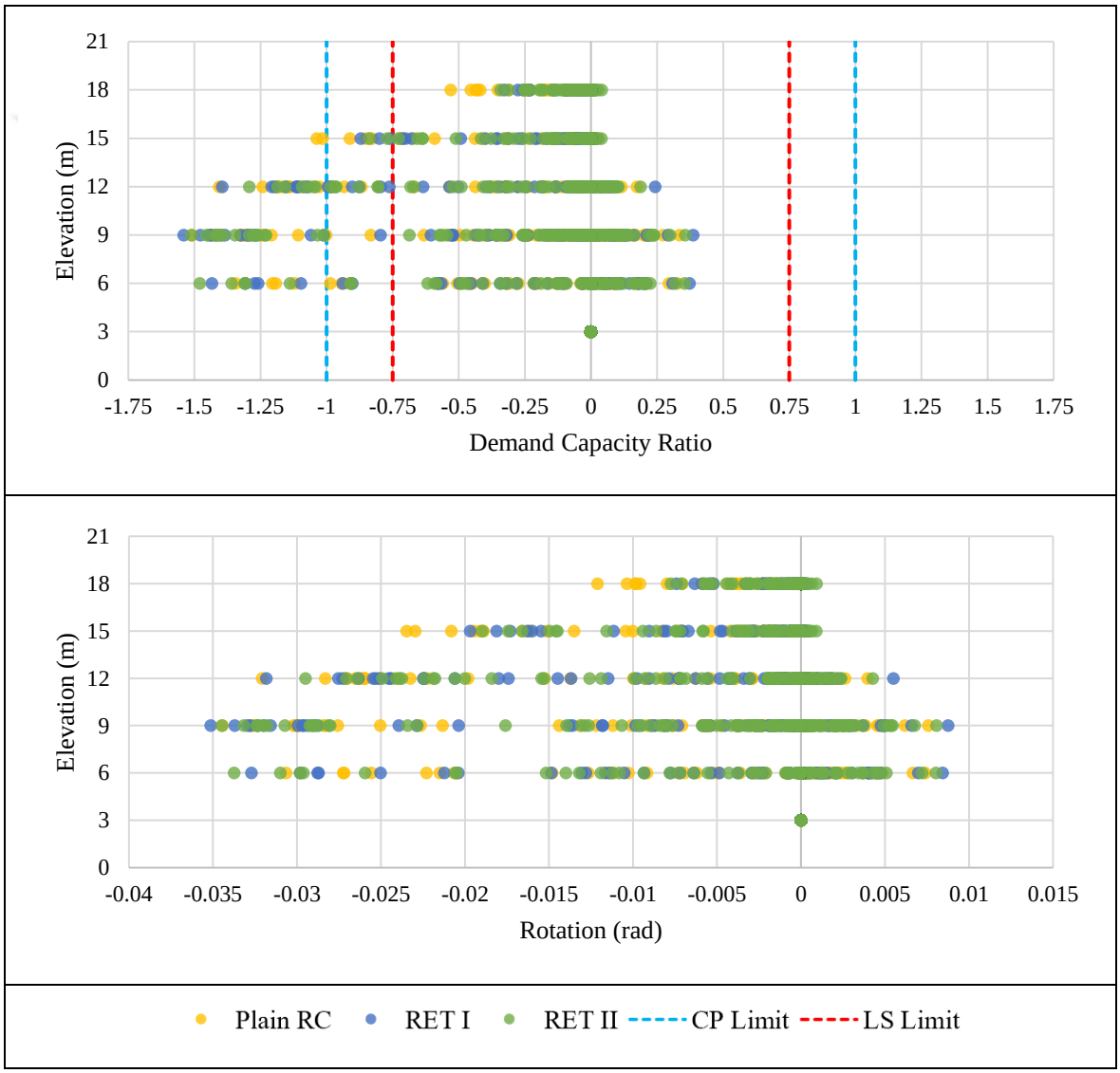

Figure 5.8. Demand - capacity ratios [top] and plastic rotations [bottom] of beams.

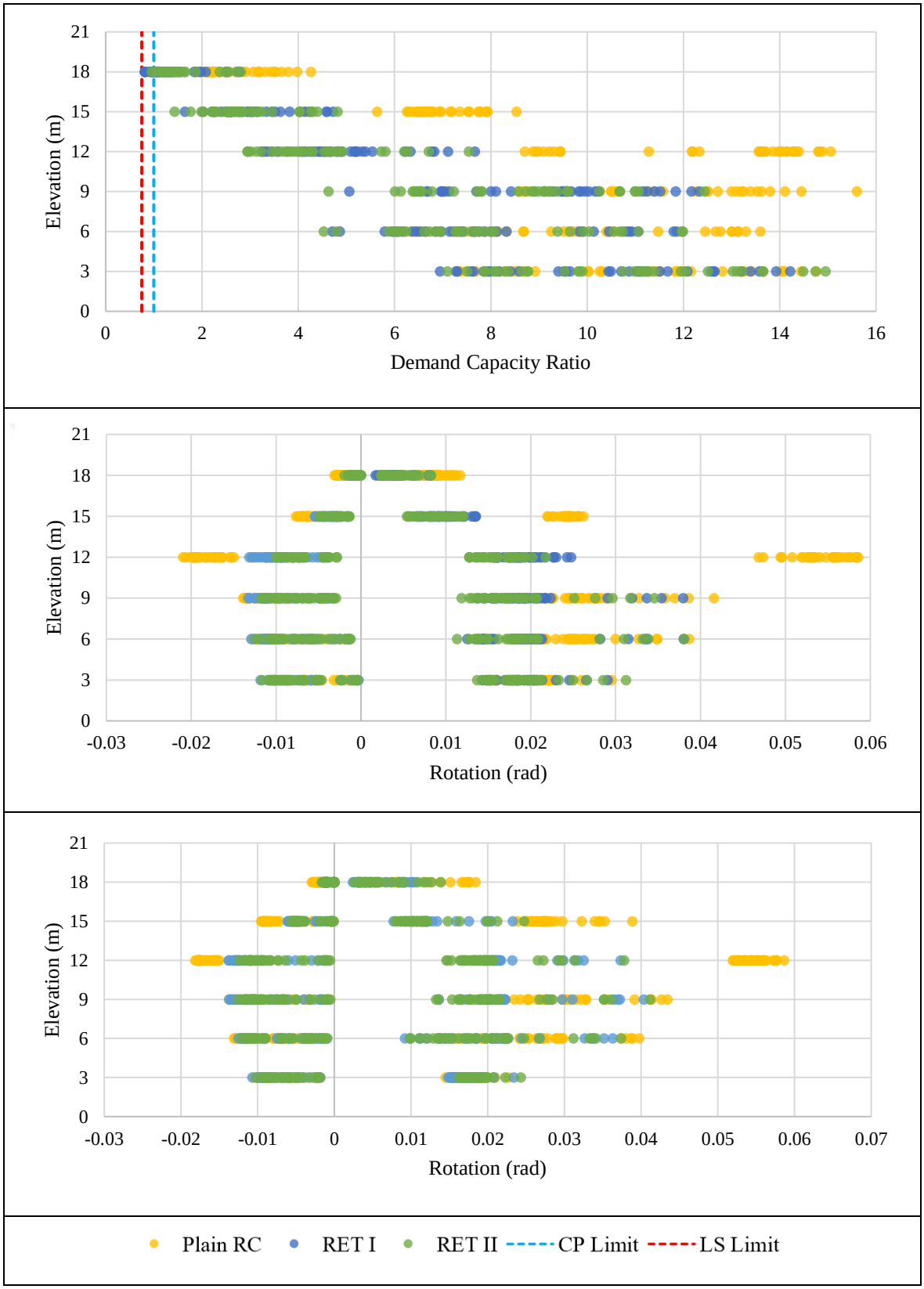

Figure 5.9. Demand - capacity ratios [top] and plastic rotations of columns in x [middle] and y [bottom] directions.

6. CONCLUSIONS AND RECOMMENDATIONS

6.1. Summary

This study is conducted with the motivation to investigate the effectiveness of a timber-based retrofitting method which could provide a cheaper alternative to some existing methods. Two case studies are investigated in detail to discuss the various effects of substandard construction material quality issues. The first CSB is intended to represent a typical well designed RC residential building with the only deficiency of being constructed with substandard construction materials and the second CSB is intended to represent a typical RC residential building which is constructed before the recent earthquake design codes and expected to suffer from most of the problems that many of the old existing buildings in Turkey suffer from such as irregular structural system, strong beam weak column condition, etc. Two different types of NTWs are assumed to be installed in both case study buildings. Within the scope of this research, three nonlinear models are generated for each CSB, and NLTHA method is conducted for each model to obtain seismic performance measures.

According to NLTHA results of the three structural models of the first case study building, when the mean IDRs are considered, retrofitting with any type of NTW did not result in a noticeable reduction. However, it should also be noted that, for CSB I the mean IDR values were already under the mean IDR limits that no further improvements were required. However, when maximum IDR values are considered, the second retrofitting scenario (RET II) was able to minimize the IDR values such that they are under the maximum IDR limit (3%). However, there were no significant difference between the IDR values of structural models of CSB I retrofitted with NTW I and NTW II. As a result of evaluation of IDR values of CSB I, it is concluded that retrofitting with NTWs is more effective when a building suffers from high IDR values. Plastic rotations of beam elements were reduced by both retrofitting scenarios, but the amount of reduction was not high enough to shift all the plastic rotation values between the capacity limits. Plastic rotation values for columns were already below the LS limit. Shear forces acting on core walls were above shear capacity limits. However, addition of NTWs did not have any noticeable reduction in the

shear demand of the building. In other words, shear forces acting on structural walls were almost the same for all three scenarios regardless of the direction of the wall. Lastly, strain values at the ends of structural walls are compared for all three structural models. Even for the plain reinforced concrete model, almost all strain values were between IO strain limits or slightly higher than the limits for both concrete (compression) and reinforcement (tension). By retrofitting, all strain values are shifted between IO strain limits.

Since it is deduced from the analysis results of the first case study building that retrofitting with NTWs is expected to be more effective when a building suffers from more extensive damage, a second case study building is also incorporated into the scope of this research. In accordance with NLTHA results of the three structural models of the second case study building, Plain RC model resulted in much higher mean and maximum IDR values that exceeded the mean and maximum IDR limits. Both retrofitting scenarios managed to successfully reduce the mean IDR values under the mean IDR limits. When max IDR values are compared, both retrofitting scenarios were able to effectively reduce the maximum IDR values obtained from analysis results of Plain RC model of CSB II but were not adequate to drag them under the maximum IDR limits. Similar to the conclusion made for CSB I, retrofitting with NTW II did not contribute significantly to the improvement of seismic performance provided by NTW I even though, due to twice as many nails used during production, it had much higher stiffness and strength values. As many of the typical residential buildings in Turkey, CSB II suffers from strong beam weak column condition and especially columns suffer from excessive plastic hinge rotations. Despite the fact that with the presented retrofitting methods plastic rotation values of the columns are reduced significantly, neither retrofitting with NTW I nor NTW II help much to minimize plastic rotation demands of columns under the plastic rotation capacity values.

To sum up, retrofitting of CSB I with any type of the NTWs did not provide significant improvement on seismic performance. However, retrofitting of CSB II with both NTW I and NTW II resulted in promising improvements on seismic performance. Overall, it can be concluded that retrofitting with NTWs may contribute effectively to seismic performance in the case of structures susceptible to extensive damage. However, it can also be concluded that retrofitting with NTW II did not contribute significantly to the

improvement of seismic performance provided by NTW I even though, due to twice as many nails used during production, it had much higher stiffness and strength values.

6.2. Future Recommendations

This study is only a starting point of investigation on the effectiveness of NTWs due to several reasons. First, there are too many factors affecting the seismic response of a building and throughout this research only two CSBs are investigated. In order to have a final conclusion on the effectiveness of retrofitting with NTWs, it would be better to investigate different types of buildings with different floor plans and number of stories. Additionally, buildings located on different soil types may also be investigated. Second, since the experimental test results used throughout this study is limited to a certain drift value which is less than the drift value experienced by NTWs that are assumed to be installed in CSB II, some assumptions had to be made in order to see the final seismic performance of CSB II. Since it might be expected for seismically vulnerable buildings to experience such high drift values, it would be better to expand the scope of the experimental tests. Third, computational simulations of the NTWs are generated using a single diagonal bracing which is expected to result in some minor inconsistencies during analysis stage. In order to avoid such inconsistencies, computational representation of NTWs with double diagonal bracing or another way of computational modeling might give more realistic results. Due to the reasons listed above , this study should be considered as an initial step of investigation of the effect of NTWs on the seismic performance of buildings.

REFERENCES

1. Burton, I., R. W. Kates, and G. F. White, *The Environment as Hazard*, The Guilford Press, New York, USA, 1993.

2. Department of Regional Development and Environment, *Disaster Planning and Development: Managing Natural Hazards to Reduce Loss*, Washington, D.C, USA, 1990.

3. UNISDR, *Making Development Sustainable: The Future of Disaster Risk Management. Global Assessment Report on Disaster Risk Reduction*, United Nations, Geneva, Switzerland, 2015.

4. UNDRR, *United Nations Office for Disaster Risk Reduction*, https://www.undrr.org/, accessed on January 8, 2022.

5. Bozkurt, E., "Neotectonics of Turkey – a Synthesis", *Geodinamica Acta*, Vol. 14, No. 1-3, pp. 3-30, 2001.

6. Gunes, O., "Turkey's Grand Challenge: Disaster-proof Building Inventory within 20 Years", *Case Studies in Construction Materials*, Vol. 2, pp. 18-34, 2015.

7. EM-DAT, "The International Disaster Database", https://www.emdat.be/, accessed on January 3, 2022.

8. Wald, L., "U.S. Geological Survey (USGS)", //www.usgs.gov/, accessed on January 5, 2022.

9. Parsons, T., S. Toda, R. S. Stein, A. Barka and J. H. Dieterich, "Heightened Odds of Large Earthquakes Near Istanbul: An Interaction-Based Probability Calculation", *Science*, Vol. 288, pp. 661-665, 2000.

10. Erdik, M., N. Aydinoglu, Y. Fahjan, K. Sesetyan, M. Demircioglu, B. Siyahi, E. Durukal, C. Ozbey, Y. Biro, H. Akman and O. Yuzugullu, "Earthquake Risk Assessment for Istanbul Metropolitan Area", *Earthquake Engineering and Engineering Vibration*, Vol. 2, No. 1, pp. 1-23, 2003.

11. Atmaca, B., S. Demir, M. Gunaydın, A. C. Altunisik, M. Husem, Ş. Ates, S. Adanur, and Z. Angın, "Lessons Learned from the Past Earthquakes on Building Performance in Turkey", *Journal of Structural Engineering & Applied Mechanics,* Vol. 3, No. 2, pp. 61-84, 2020.

12. Dere, Y., "Assessing a Retrofitting Method for Existing RC Buildings with Low Seismic Capacity in Turkey", *Journal of Performance of Constructed Facilities*, Vol. 31, No. 2, 2017.

13. Anil, O and S. Altin, "An Experimental Study on Reinforced Concrete Partially Infilled Frames", *Engineering Structures*, Vol. 29, No. 3, pp. 449-460, 2006.

14. Altin, S., O. Anil and M. E. Kara, "Strengthening of Reinforced Concrete Nonductile Frames with Reinforced Concrete Infills: An Experimental Study", *Cement and Concrete Composites*, Vol. 30, No. 7, pp. 612-621, 2007.

15. Farghaly, A. A. and A. M. Abdallah, "Evaluation of Seismic Retrofitting Techniques Used in Old Reinforced Concrete Buildings", *Journal of Engineering*, Vol. 4, No. 6, pp. 14-22, 2015.

16. Contiguglia, C.P., A. Pelle, Z. Lai, B. Briseghella and C. Nuti, "Chinese High Rise Reinforced Concrete Building Retrofitted with CLT Panels", *Sustainability*, Vol. 13, No. 17, 2021.

17. Turkish Building Seismic Code: Specifications for Design of Buildings Under Earthquake Action, Disaster and Emergency Management Presidency, Ankara, Turkey, 2018.

18. Mander, J. B., M. J. N. Priestley and R. Park, “Theoretical Stress-Strain Model for Confined Concrete”, *Journal of Structural Engineering,* Vol. 114, No. 8, pp. 1804-1826, 1988.

19. TS 498: Design Loads for Buildings, Turkish Standards Institute, Ankara, Turkey, 1997.

20. AFAD (Disaster and Emergency Management Presidency), “Turkish Earthquake Hazard Map”, https://tdth.afad.gov.tr/, accessed on December 7, 2021.

21. Pacific Earthquake Engineering Research Center, “Next Generation Attenuation-West2”, 2013, https://ngawest2.berkeley.edu, accessed on January15, 2022.

22. TS 500: Requirements for Design and Construction of Reinforced Concrete Structures, Turkish Standards Institute, Ankara, Turkey, 2000.